US009140896B2

(12) **United States Patent**　　　　(10) **Patent No.:**　　**US 9,140,896 B2**
Norman et al.　　　　　　　　　　　(45) **Date of Patent:**　　**Sep. 22, 2015**

(54) **ACTIVE BEAM SHAPING SYSTEM AND METHOD USING SEQUENTIAL DEFORMABLE MIRRORS**

(71) Applicant: **The Johns Hopkins University,** Baltimore, MD (US)

(72) Inventors: **Colin A. Norman,** Baltimore, MD (US); **Laurent A. Pueyo,** Baltimore, MD (US)

(73) Assignee: **The Johns Hopkins University,** Baltimore, MD (US)

(*) Notice: Subject to any disclaimer, the term of this patent is extended or adjusted under 35 U.S.C. 154(b) by 33 days.

(21) Appl. No.: **14/052,599**

(22) Filed: **Oct. 11, 2013**

(65) **Prior Publication Data**
US 2015/0104188 A1　　Apr. 16, 2015

(51) **Int. Cl.**
H04B 10/00	(2013.01)
G02B 26/08	(2006.01)
G02B 23/02	(2006.01)
G02B 19/00	(2006.01)
H04B 10/516	(2013.01)
H04B 10/60	(2013.01)
H04B 10/25	(2013.01)

(52) **U.S. Cl.**
CPC *G02B 26/0816* (2013.01); *G02B 19/0019* (2013.01); *G02B 23/02* (2013.01); *H04B 10/25* (2013.01); *H04B 10/516* (2013.01); *H04B 10/60* (2013.01)

(58) **Field of Classification Search**
CPC .. H04B 10/11; H04B 10/112; H04B 10/1121; H04B 10/1123; H04B 10/1125; H04B 10/118; H04B 10/516; H04B 10/25; H04B 10/60; G02B 26/0816; G02B 23/02; G02B 19/0019

USPC 398/118, 119, 121, 124, 128, 130
See application file for complete search history.

(56) **References Cited**

U.S. PATENT DOCUMENTS

6,934,477	B2 *	8/2005	Willebrand	....	398/139
7,197,248	B1 *	3/2007	Vorontsov et al.	....	398/119
7,397,018	B1 *	7/2008	Pham et al.	....	250/201.9
7,486,893	B1 *	2/2009	Pepper et al.	....	398/119
2003/0034432	A1 *	2/2003	Presby et al.	....	250/201.9
2003/0099264	A1 *	5/2003	Dantus et al.	....	372/25
2005/0196170	A1 *	9/2005	Winsor	....	398/118
2008/0002972	A1 *	1/2008	Dogariu et al.	....	398/25
2010/0172649	A1 *	7/2010	Graves	....	398/118
2011/0235916	A1 *	9/2011	Veeraraghavan et al.	.....	382/190

(Continued)

OTHER PUBLICATIONS

Barman et al., 2011a, ApJ, 733, 65.

(Continued)

Primary Examiner — Dalzid Singh
(74) *Attorney, Agent, or Firm* — Venable LLP; Henry J. Daley

(57) **ABSTRACT**

An active optical beam shaping system includes a first deformable mirror arranged to at least partially intercept an entrance beam of light and to provide a first reflected beam of light, a second deformable mirror arranged to at least partially intercept the first reflected beam of light from the first deformable mirror and to provide a second reflected beam of light, and a signal processing and control system configured to communicate with the first and second deformable mirrors. The first deformable mirror, the second deformable mirror and the signal processing and control system together provide a large amplitude light modulation range to provide an actively shaped optical beam.

17 Claims, 34 Drawing Sheets
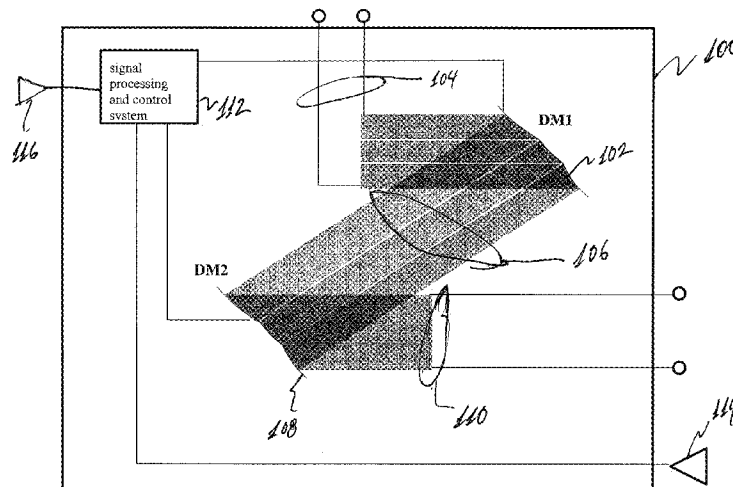
(56)   **References Cited**

U.S. PATENT DOCUMENTS

2011/0267663 A1 * 11/2011 Murayama 359/9
2012/0260906 A1 * 10/2012 Baeten 126/600

OTHER PUBLICATIONS

Barman et al., 2011b, ApJ, 735, L39.
Benamou et al., 2010, ESAIM: Mathematical Modelling and Numerical Analysis, 44, 737.
Bord'e, P. J. & Traub, W. A. 2006, ApJ, 638, 488.
Brown et al., 1990, Icarus, 87, 484.
Carlotti, A., Vanderbei, R., & Kasdin, N. J. 2011, Optics Express, 19, 26796.
Dacorogna et al., 1990, Ann. Inst Henri Poincare, 7.
Dodson-Robinson, S. E., Veras, D., Ford, E. B., & Beichman,. A. 2009, ApJ, 707, 79.
Dohlen et al., 2006, in Presented at the Society of Photo-Optical Instrumentation Engineers (SPIE) Conference, vol. 6269, Ground-based and Airborne Instrumentation for Astronomy. Edited by McLean, Ian S. et al., Proceedings of the SPIE, vol. 6269, pp. 62690Q (2006).
Fortney, J. J., Marley, M. S., Saumon, D., & Lodders, K. 2008, ApJ, 683, 1104.
Froese et al., 2012, Arxiv preprint arXiv:1204.5798.
Give'on, A., Belikov, R., Shaklan, S., & Kasdin, J. 2007, Opt. Express, 15, 12338.
Give'on et al., 2006, J. Opt. Soc. Am. A, 5, pp. 1063-1073.
Glimm et al., 2002, J. Math. Sci., 117.
Graham et al., 2007, ArXiv e-prints, 704.
Guyon et al., "Phase induced amplitude apodization (PIAA) coronagraphy: recent results and future prospects," Proc. SPIE 8442, Space Telescopes and Instrumentation 2012: Optical, Infrared, and Millimeter Wave, 84424V (Aug. 22, 2012); doi:10.1117/12.927187.
Guyon et al., 2005, ApJ, 622, 744.
Guyon et al., 2008, in Society of Photo-Optical Instrumentation Engineers (SPIE) Conference Series, vol. 7010, (SPIE) Conference Series.
Guyon et al., 2009, ApJ, 693, 75-84.
Guyon et al., 2010a, ApJS, 190, 220.
Guyon et al., 2010b, PASP, 122, 71.
Guyon, O. 2003, A&A, 404, 379.
Guyon, O.. 2005, ApJ, 629, 592.
Hinkley et al., 2011, PASP, 123, 74.
Johnson et al., 2010, PASP, 122, 905.
Kalas et al., 2008, Science, 322, 1345.
Kasdin et al., 2005, Appl. Opt., 44, 1117.
Kratter et al., 2010, ApJ, 710, 1375.
Krist et al., 2010in (SPIE), 77314N.
Krist et al., 2011, Assessing the performance limits of internal; coronagraphs through end-to-end modeling, in Society of Photo-Optical Instrumentation Engineers (SPIE) Conference Series, vol. 8151, Engineers (SPIE) Conference Series.
Kuchner et al., 2002, ApJ, 570, 900.
Lagrange et al., 2010, Science, 329, 57.
Loeper et al., 2005, Comptes Rendus Mathematique, 340, 319.
Lozi et al., 2009, PASP, 121, 1232.

Macintosh et al., 2006, in Society of Photo-Optical Instrumentation Engineers (SPIE) Conference Series, vol. 6272, Society of Photo-Optical Instrumentation Engineers (SPIE) Conference Series.
Madhusudhan et al., 2011, ApJ, 737, 34.
Marley et al., 2010, ApJ, 723, L117.
Marois et al., 2008, Science, 322, 1348.
Martinache et al., 2006, ApJ, 639, 1129.
Martinez et al., 2008, A&A, 492, 289.
Martinez et al., 2010, A&A, 520, A110.
Mawet et al., 2010in (SPIE), 773914.
Mawet et al., 2011, Optics Letters, 36, 1506.
Monge, G. 1781, Histoire de l'Acad'emie Royale des Sciences de Paris, 666.
Pluzhnik et al., 2005, ArXiv Astrophysics e-prints.
Postman et al., 2010, in Astronomical Society of the Pacific Conference Series, vol. 430, Pathways Towards Habitable Planets, ed. V. Coud'e Du Foresto, D. M. Gelino, & I. Ribas, 361.
Poyneer et al., 2005, Journal of the Optical Society of America A, 22, 1515.
Pueyo et al., "High Contrast Imaging with an Arbitrary Aperture: Active Correction of Aperture Discontinuities," ApJ, Nov. 2012, arXiv:1211.6112.
Pueyo et al., 2009, Appl. Opt., 48, 6296.
Pueyo et al., 2010in (SPIE), 77362A.
Pueyo et al., 2011, ApJS, 195, 25.
Pueyo et al., 2011, J. Opt. Soc. Am. A, 28, 189.
Pueyo, L. 2007, ApJ, 666, 609.
Rafikov, R. R. 2005, ApJ, 621, L69.
Rouan et al., 2000, PASP, 112, 1479.
Sauvage et al., 2007, Journal of the Optical Society of America A, 24, 2334.
Shaklan et al., 2006, Appl. Opt., 45, 5143.
Shaklan et al., 2006, in Presented at the Society of Photo-Optical Instrumentation Engineers (SPIE) Conference, vol. 6265, Space Telescopes and Instrumentation I: Optical, Infrared, and Millimeter. Eds. Mather, John C et al., Proceedings of the SPIE, vol. 6265, pp. 62651I.
Soummer et al., 2003, A&A, 397, 1161.
Soummer et al., 2009, ApJ, 695, 695.
Soummer et al., 2011, ApJ, 729, 144.
Spiegel et al., 2012, ApJ, 745, 174.
Thomas et al., 2011, AJ, 142, 119.
Traub et al., 2003, ApJ, 599, 695.
Trauger et al., 2007, Nature, 446, 771.
Trauger et al., 2010, in Society of Photo-Optical Instrumentation Engineers (SPIE) Conference Series, vol. 7731, (SPIE) Conference Series.
Vanderbei et al., 2003a, ApJ, 599, 686.
Vanderbei et al., 2003b, ApJ, 590, 593.
Vanderbei et al., 2005, ApJ, 626, 1079.
Vanderbei et al., 2007, ApJ, 665, 794.
V'erinaud et al., 2010, in Society of Photo-Optical Instrumentation Engineers (SPIE) Conference Series, vol. 7736, Society of Photo-Optical Instrumentation Engineers (SPIE) Conference Series.
Wallace et al., 2009, in Proceedings of the SPIE conference 7440, ed. S. B. Shaklan, vol. 7440 (SPIE).
Wallace et al., 2011, Proc SPIE 8126.
Zheligovsky et al., 2010, Journal of Computational Physics, 229, 5043.

* cited by examiner

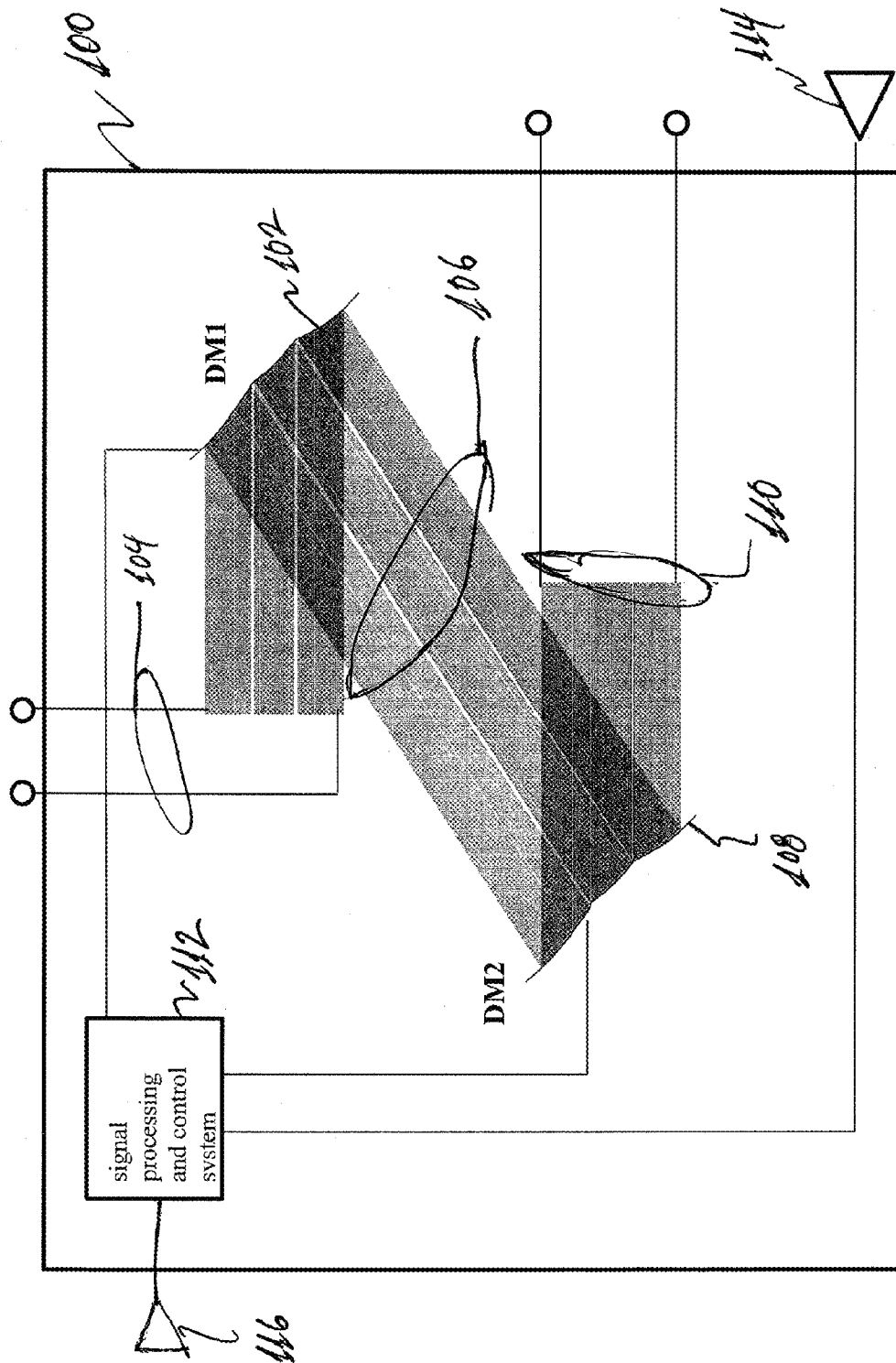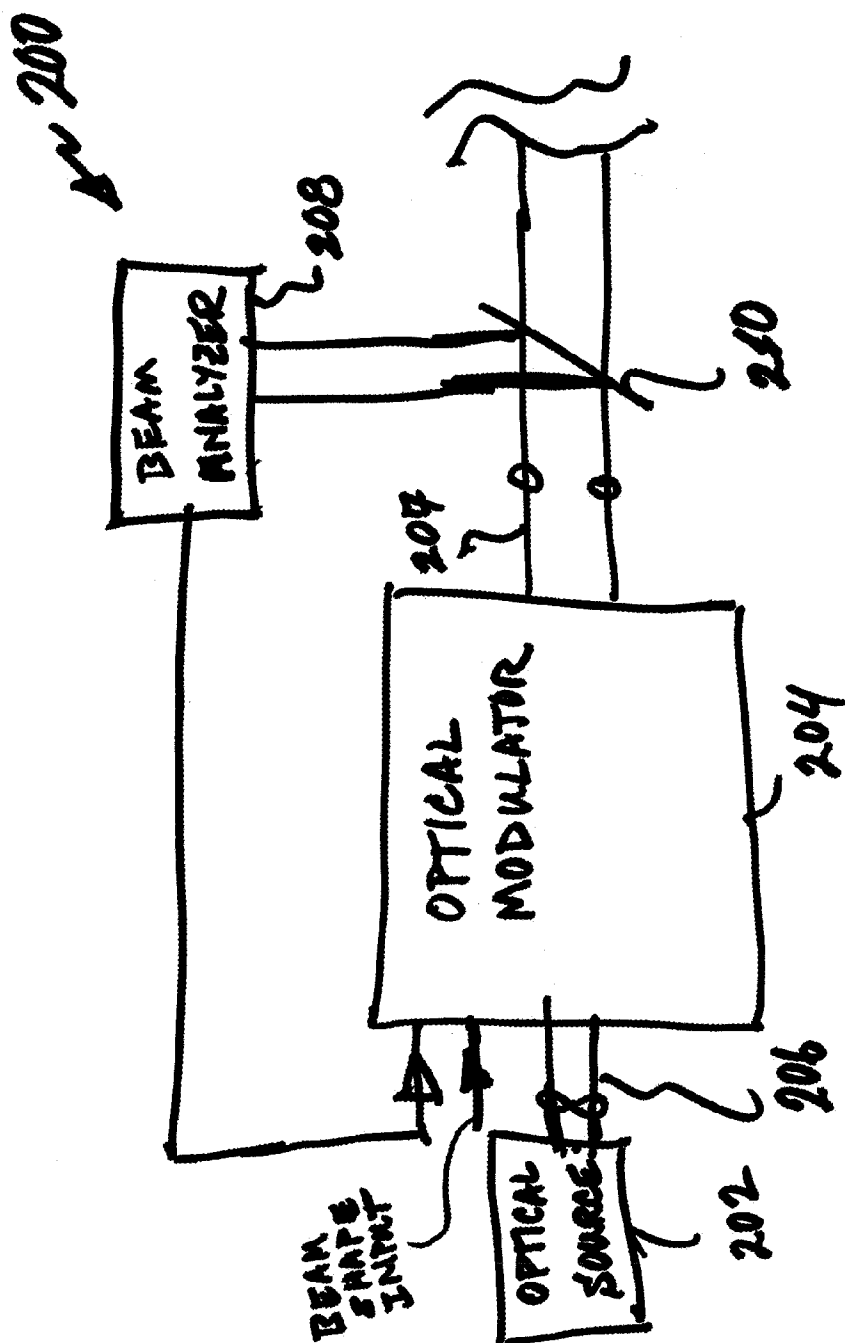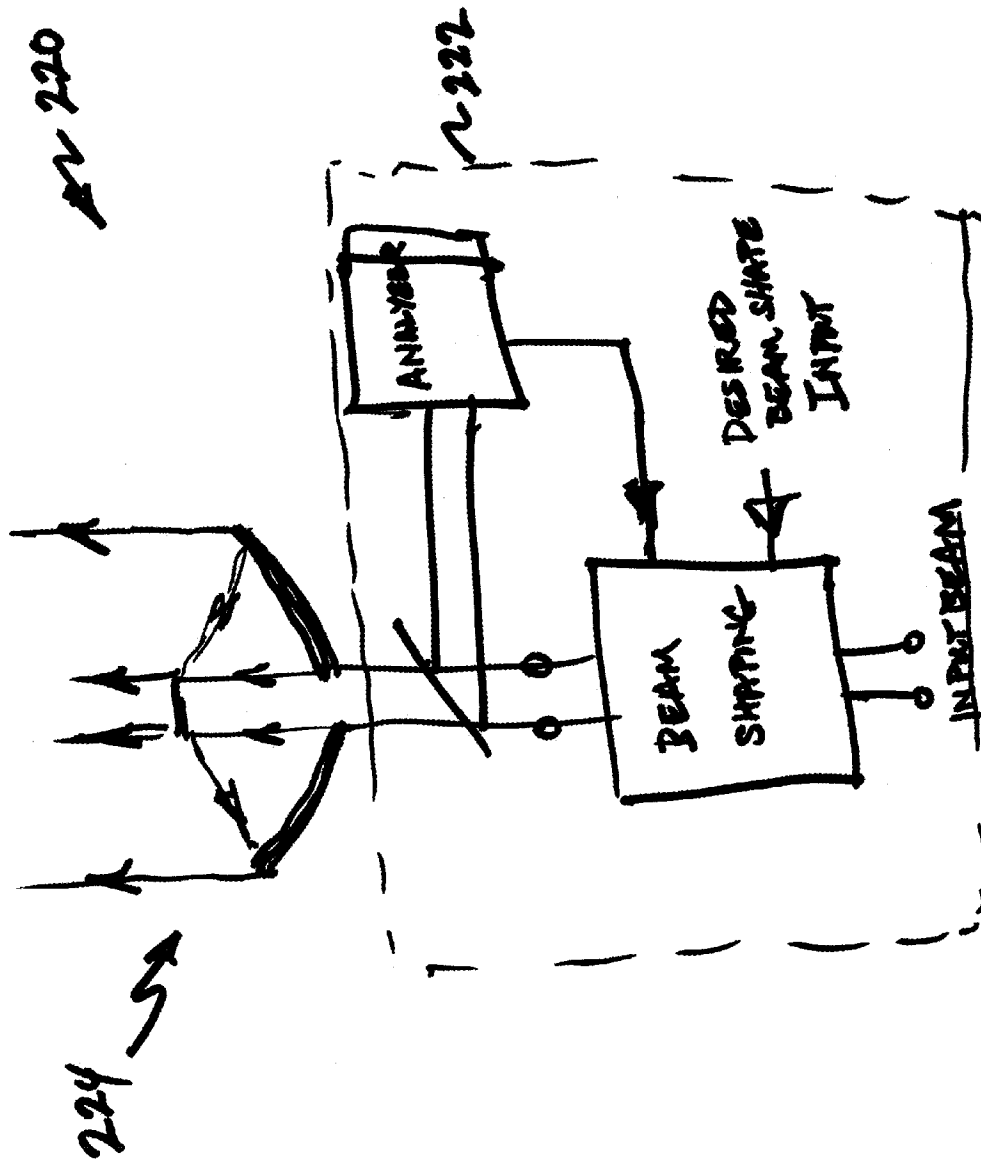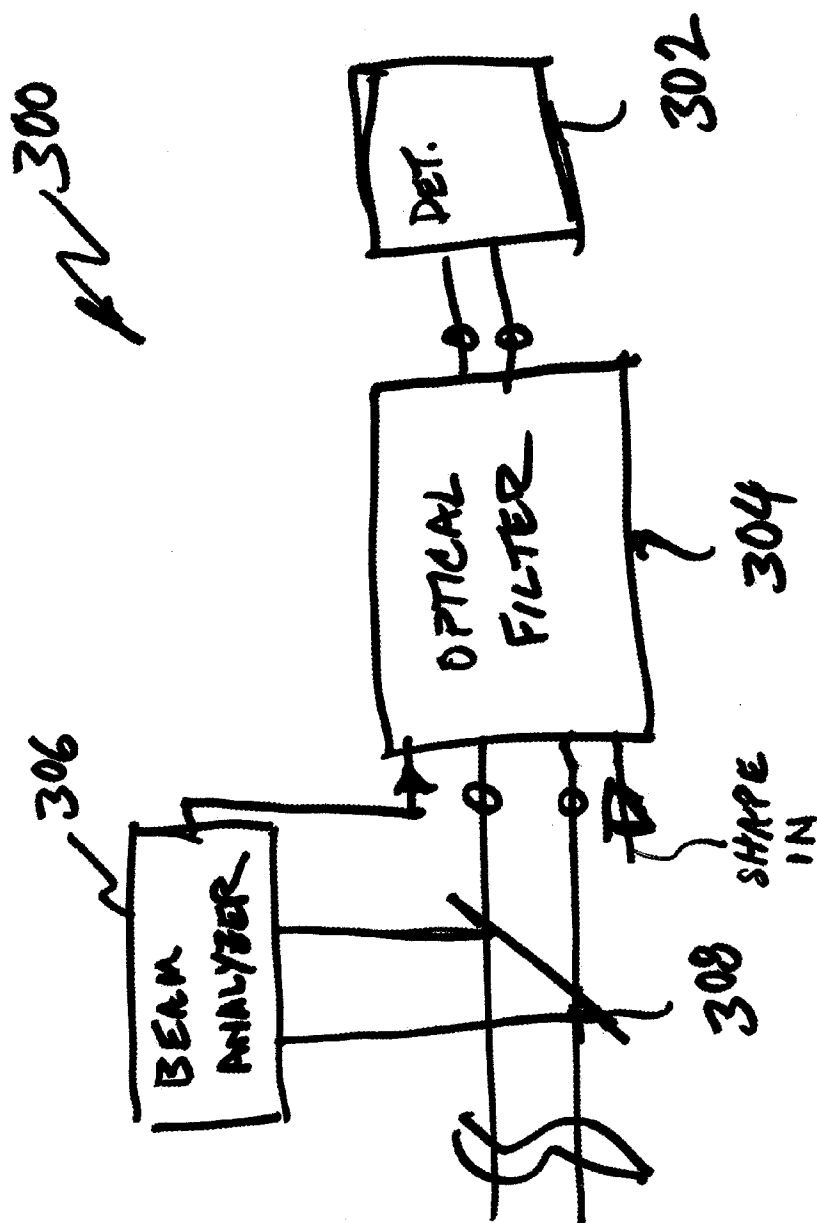**FIG. 1A**
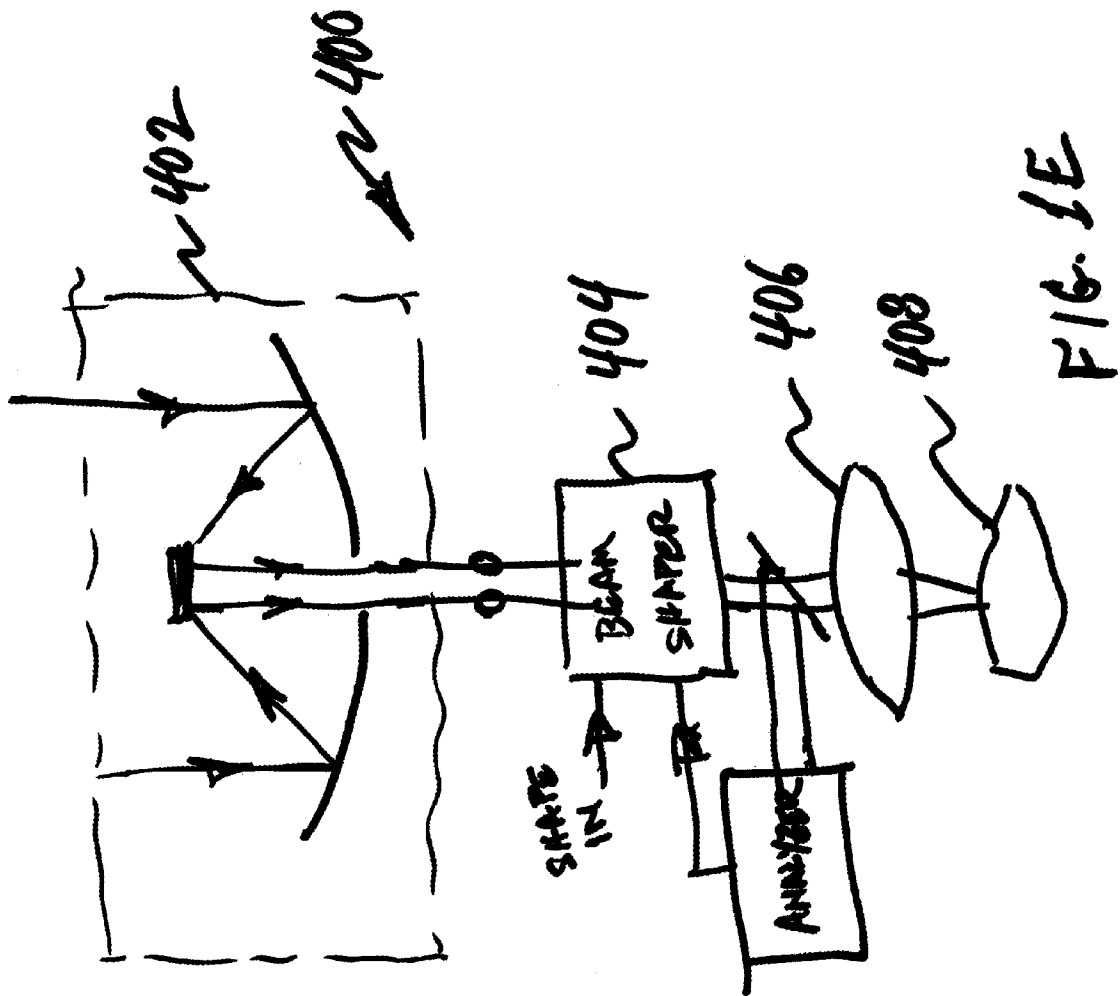
200

BEAM ANALYZER

208

250

204

OPTICAL MODULATOR

204

206

BEAM SHAPE INPUT

OPTICAL SOURCE

202

FIG. 1B

FIG. 1C

FIG. 4D

FIG. 1E
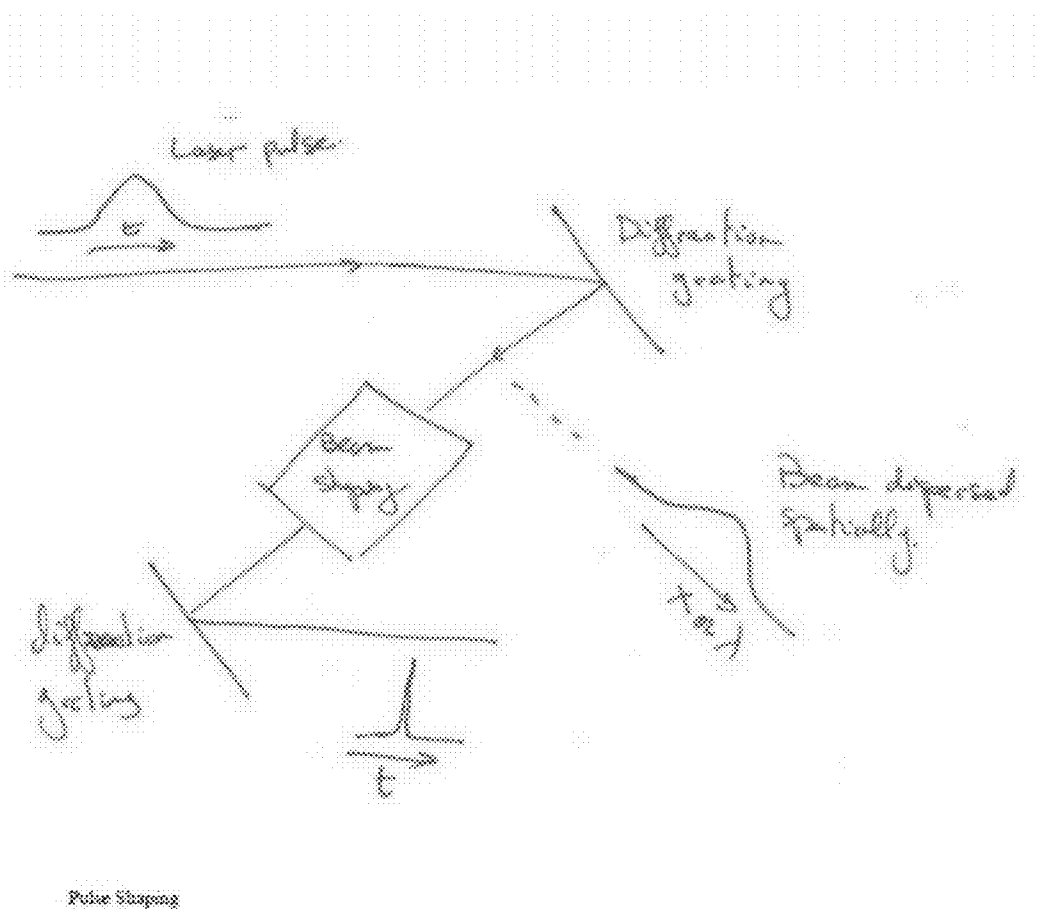
FIG. 1F
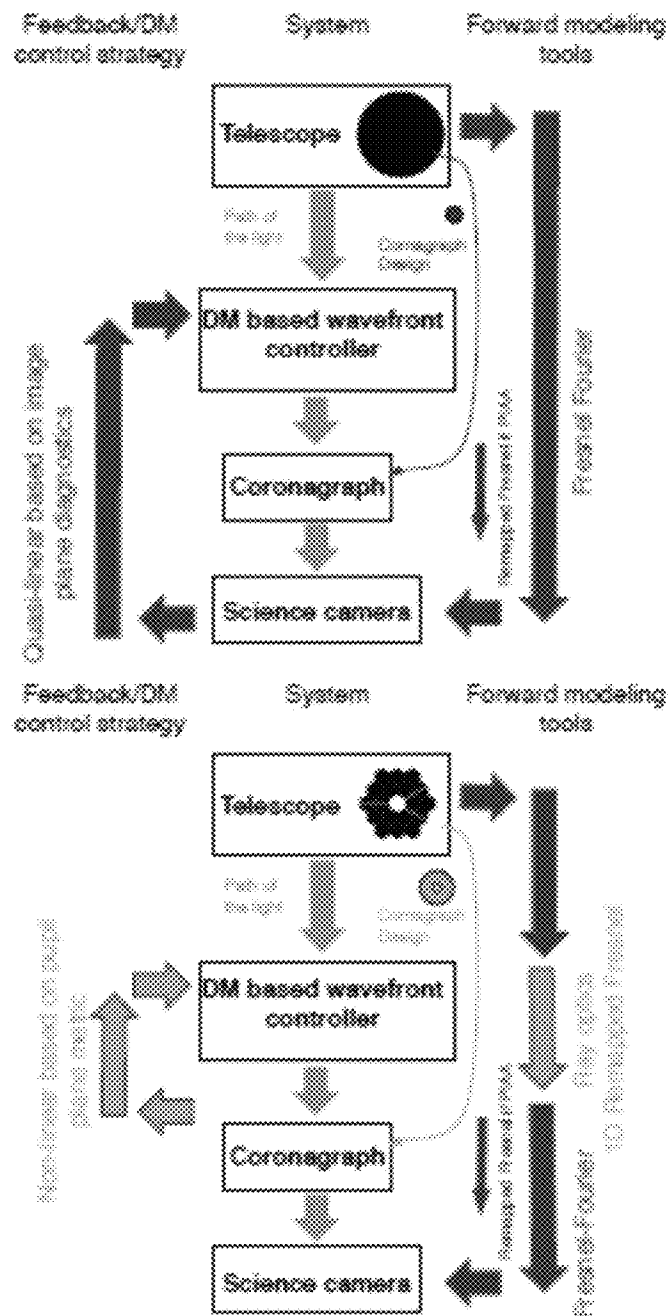
FIG. 1G
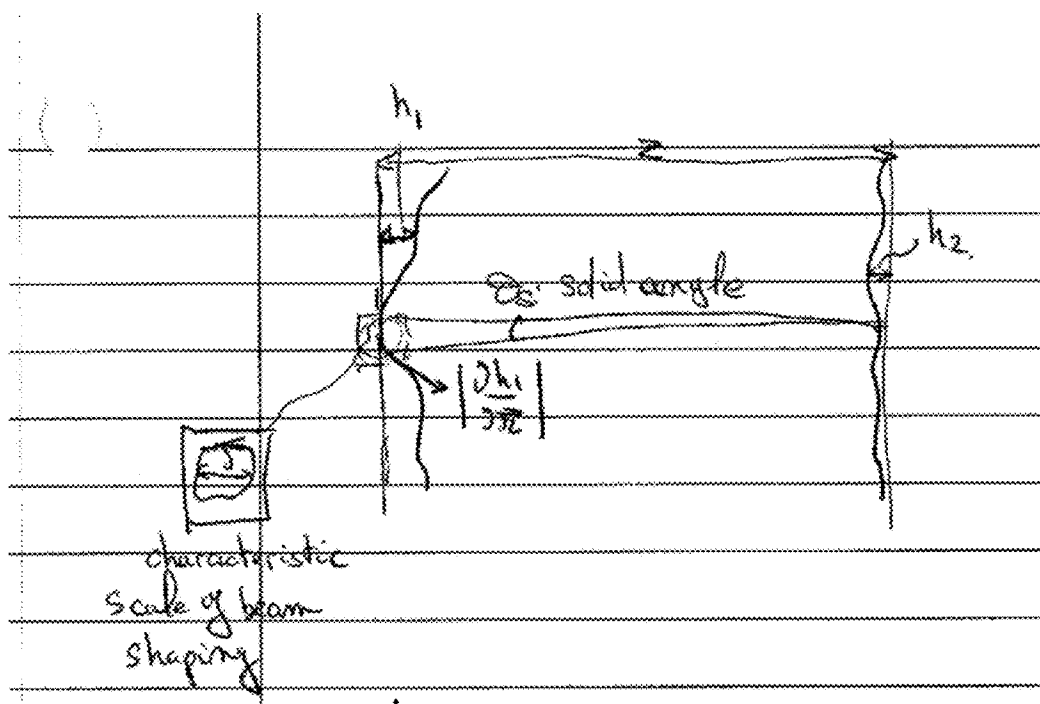
FIG. 1H
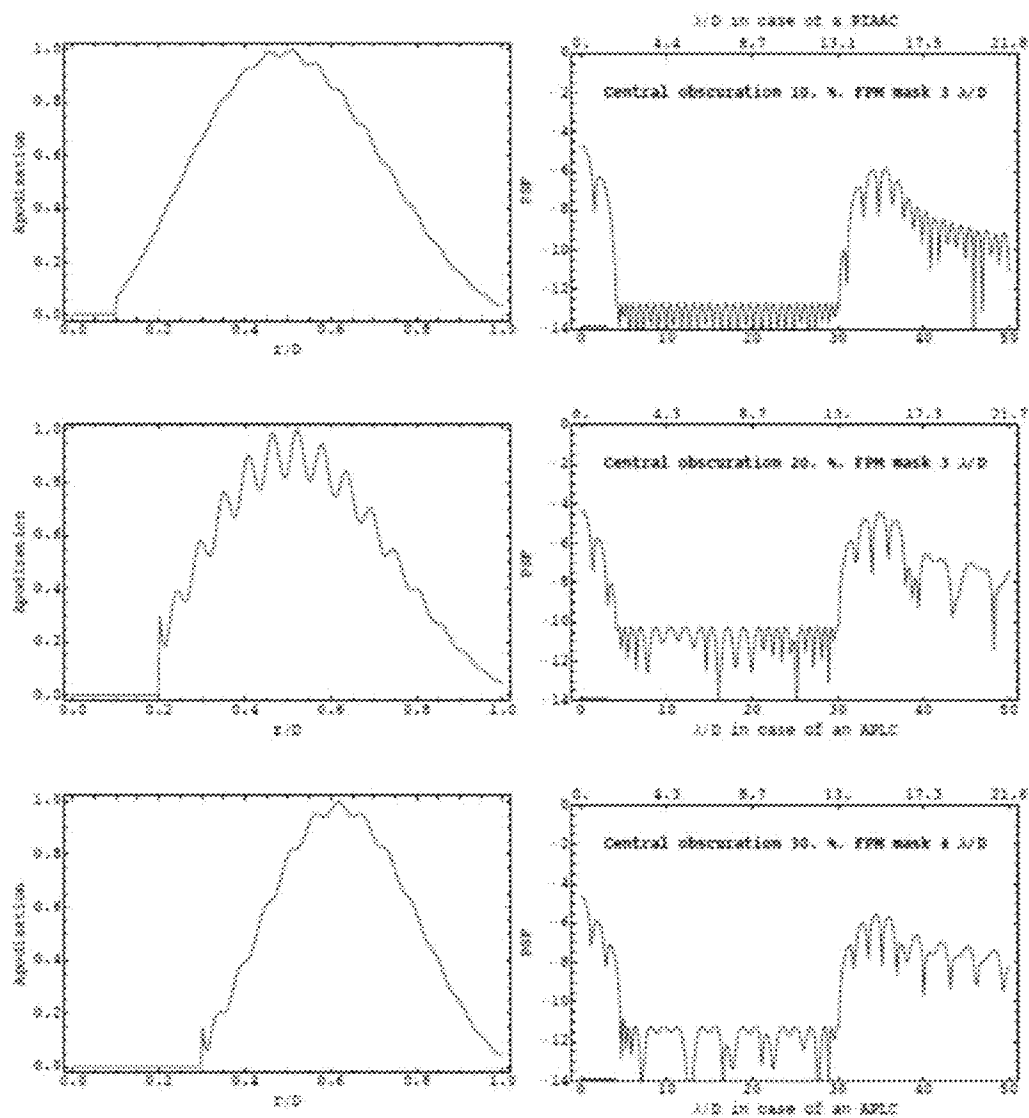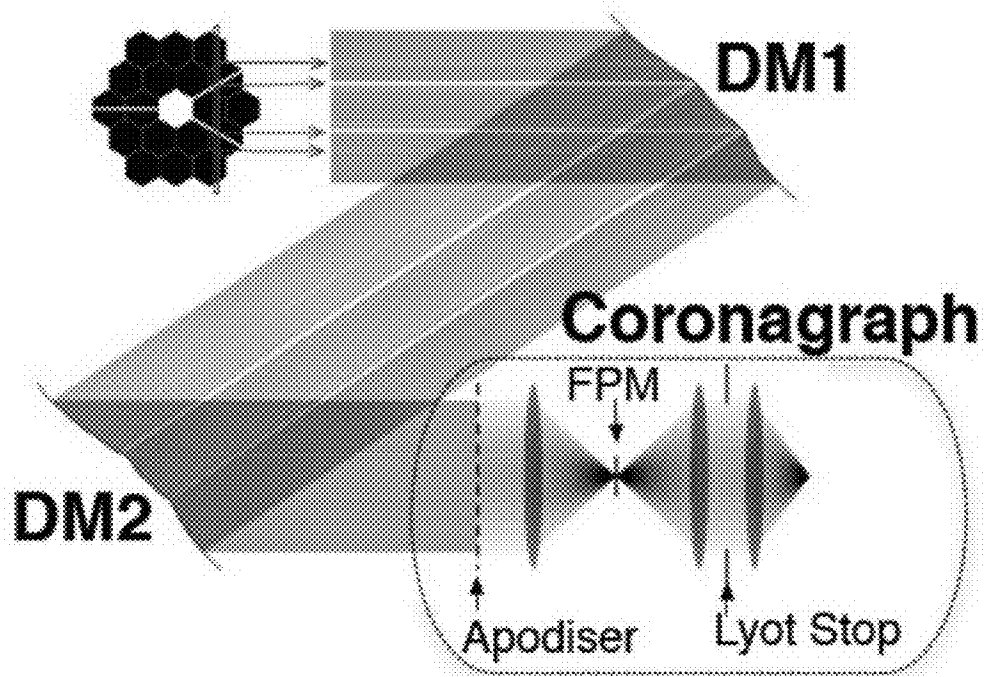
FIG. 2

FIG. 3
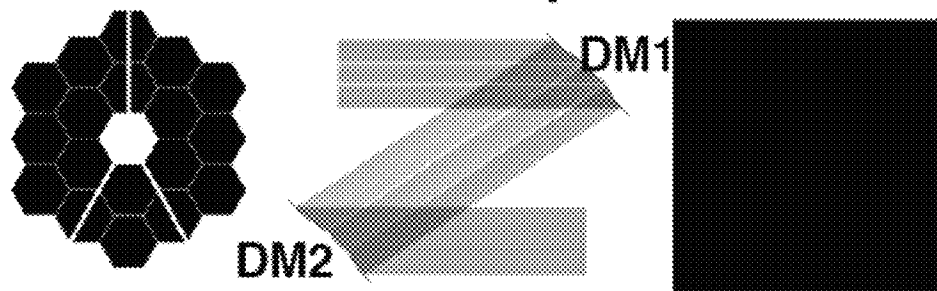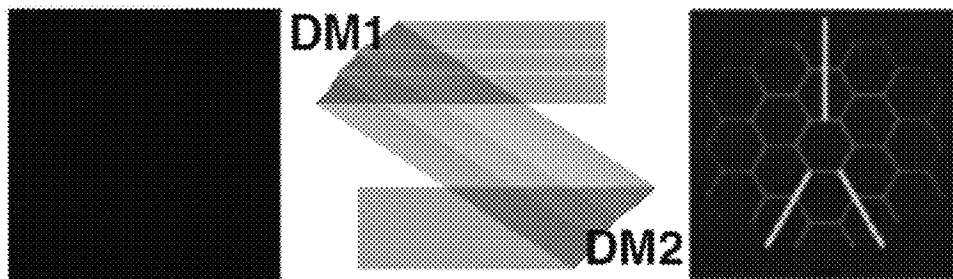
FIG. 4

Forward coordinate system
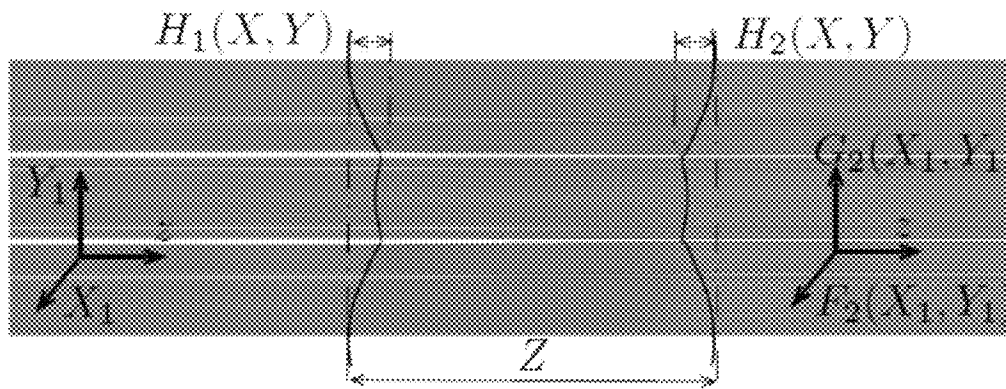
Reverse coordinate system

FIG. 5

FIG. 6

$$F_2\left(X_1, \frac{1}{2}\right)$$

$$10^{-4}\left(-\frac{1}{2} - F_2\left(\frac{1}{2}, Y_1\right)\right)$$

$$10^{-4}\left(\frac{1}{2} - F_2\left(\frac{1}{2}, Y_1\right)\right)$$

$$X_2 - F_2(X_1, Y_1)$$

$$F_2\left(X_1, -\frac{1}{2}\right)$$

FIG. 7

$$G_2\left(-\frac{1}{2}, Y_1\right) \qquad\qquad G_2\left(\frac{1}{2}, Y_1\right)$$

$$10^{-3}\left(\frac{1}{2} - G_2\left(X_1, \frac{1}{2}\right)\right)$$

$$Y_2 - G_2(X_1, Y_1)$$

$$10^{-3}\left(\frac{1}{2} - G_2\left(X_1, -\frac{1}{2}\right)\right)$$
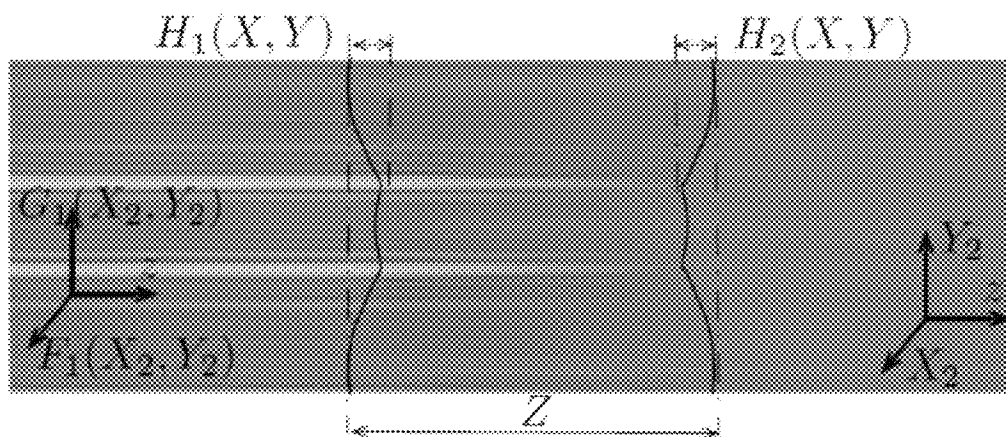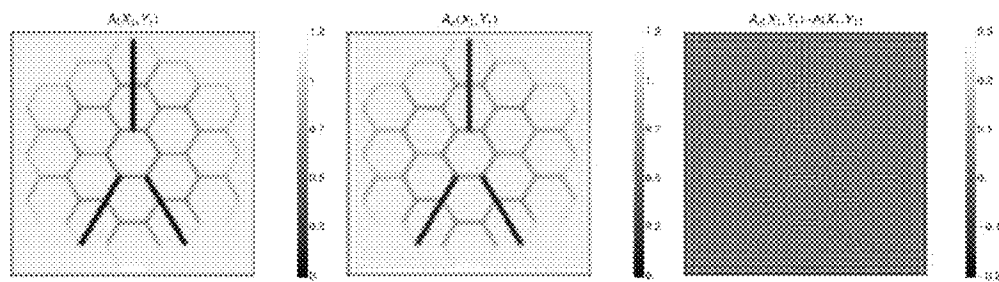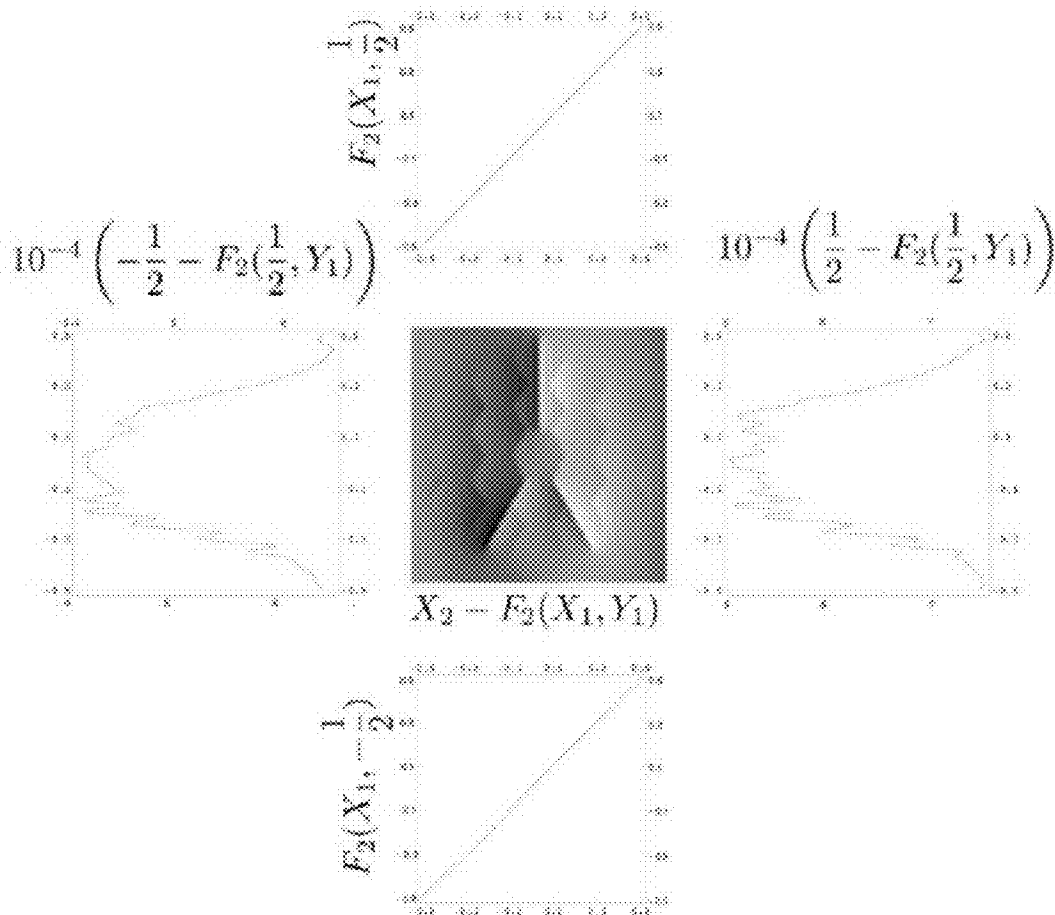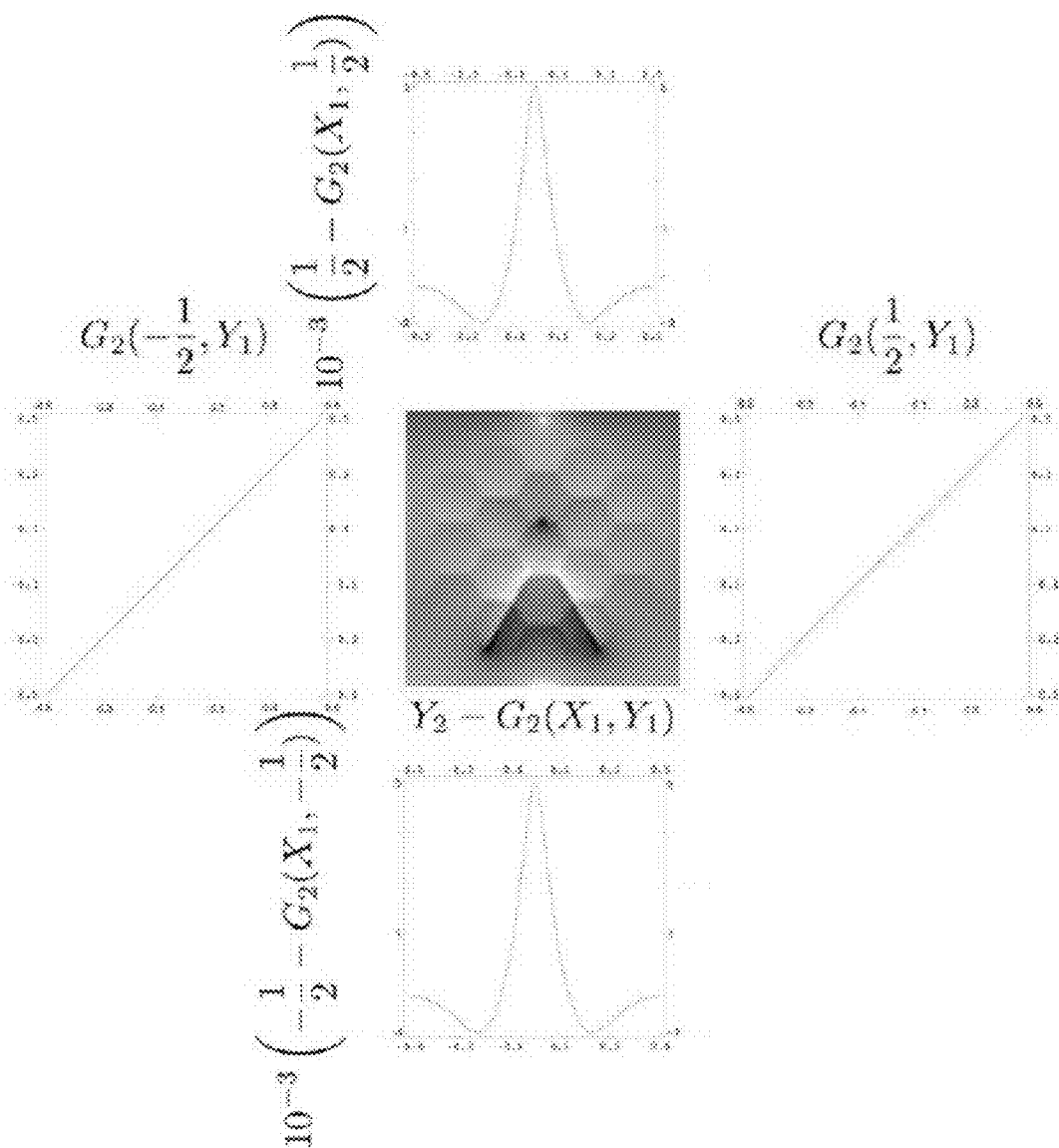
FIG. 8
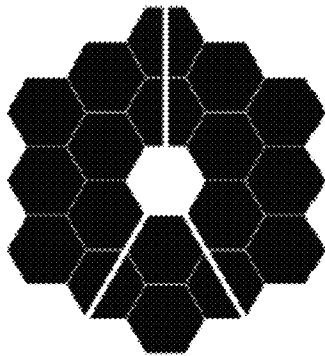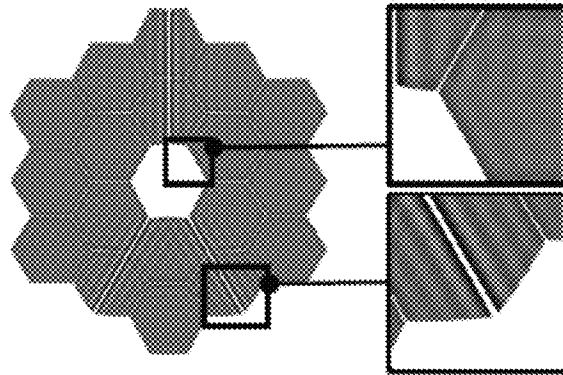
FIG. 9

FIG. 10
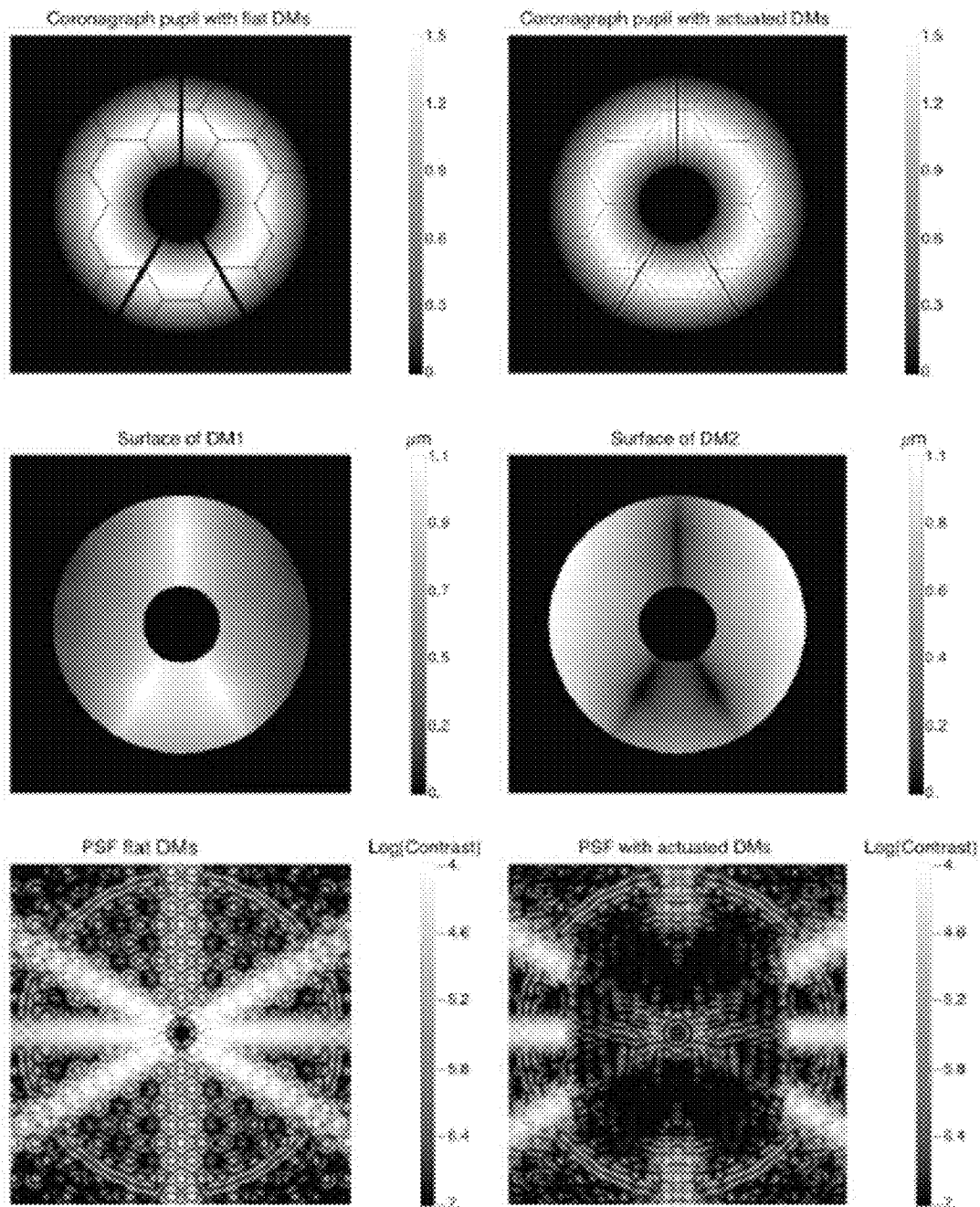
FIG. 11

FIG. 12
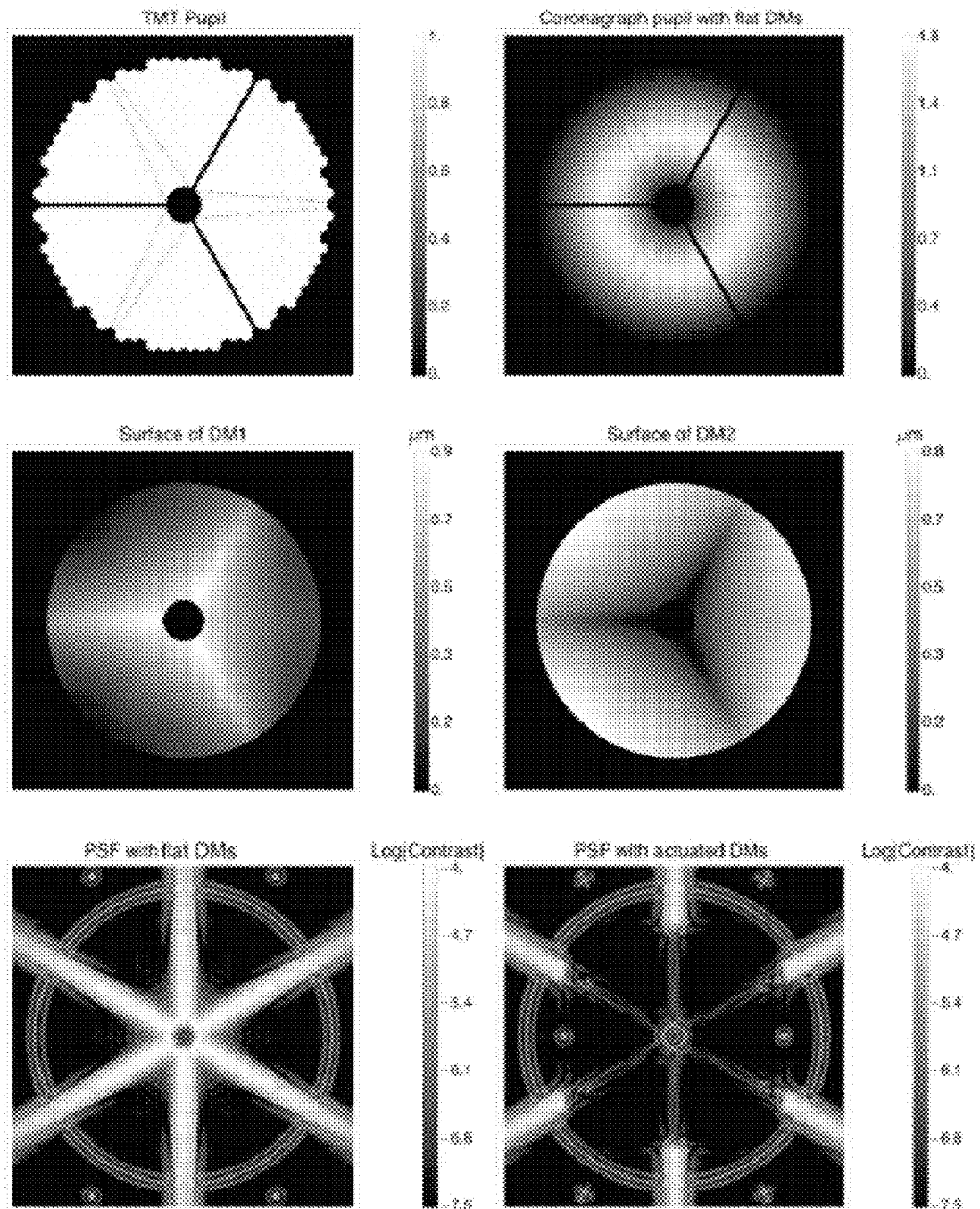
FIG. 13

FIG. 14

FIG. 15

FIG. 16

Flat DMs

Actuated DMs

FIG. 17

FIG. 18

FIG. 19

FIG. 20
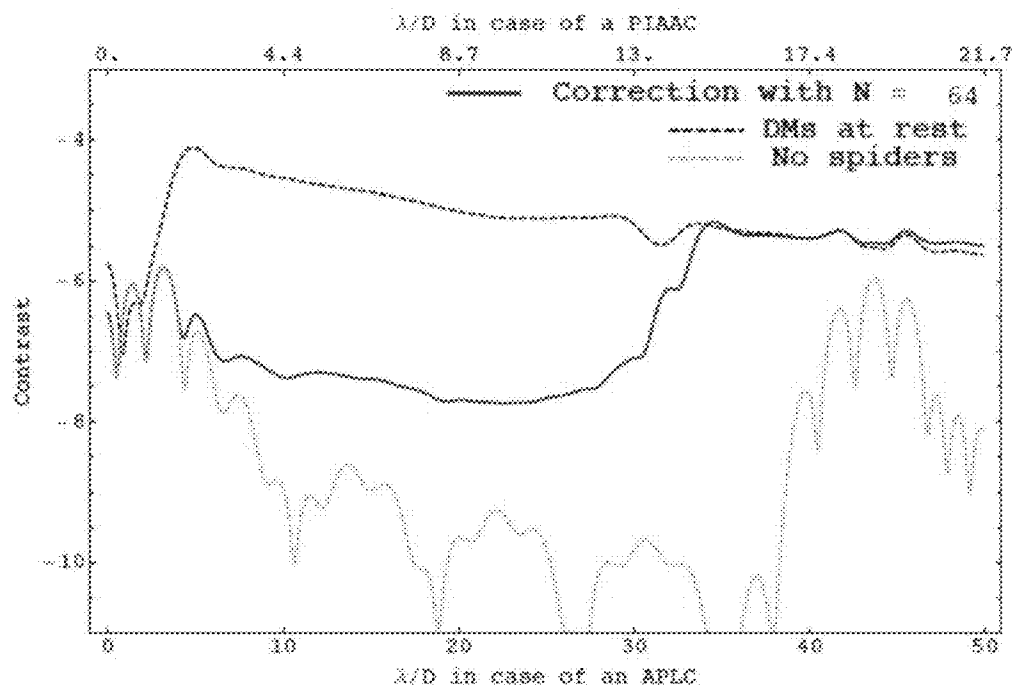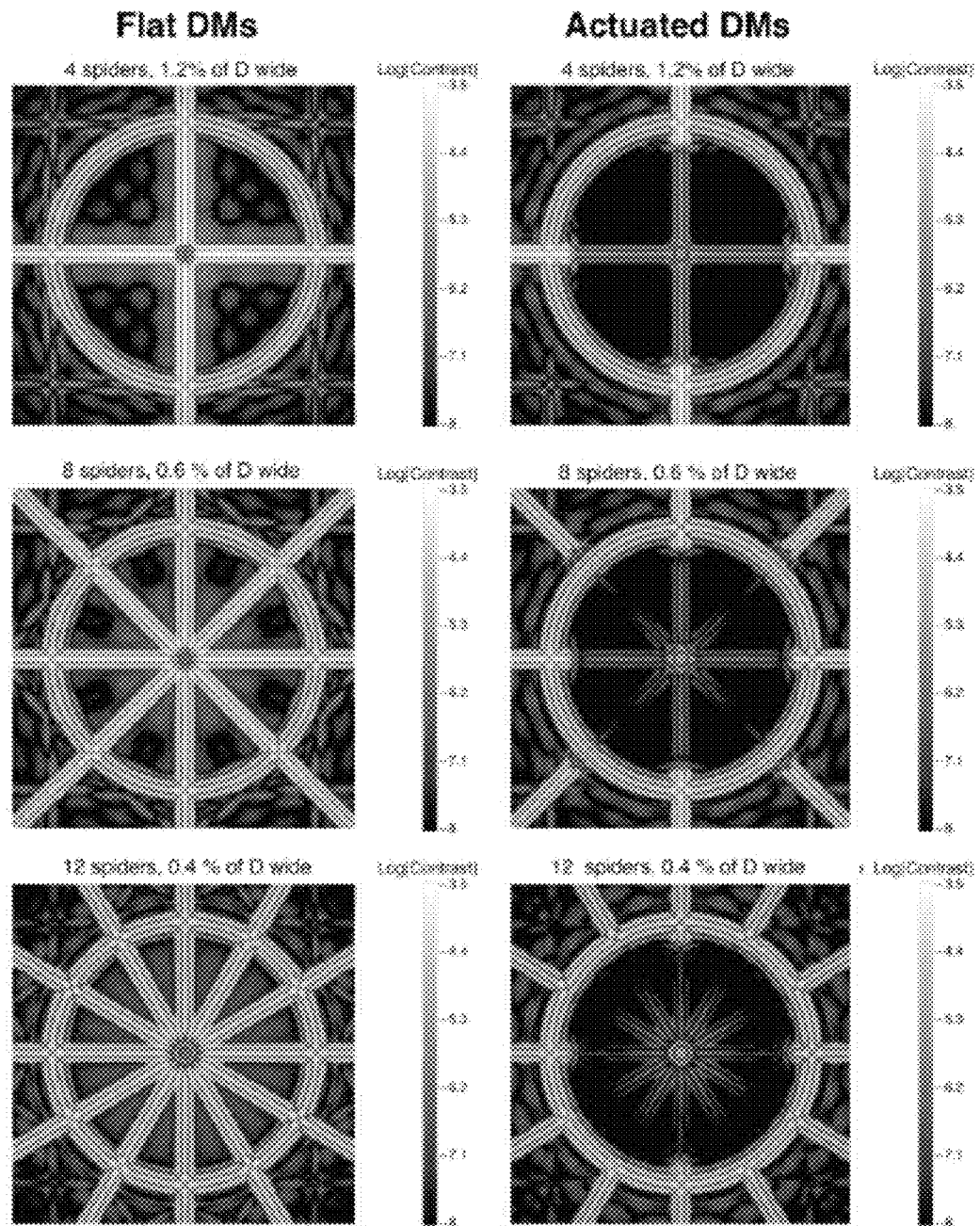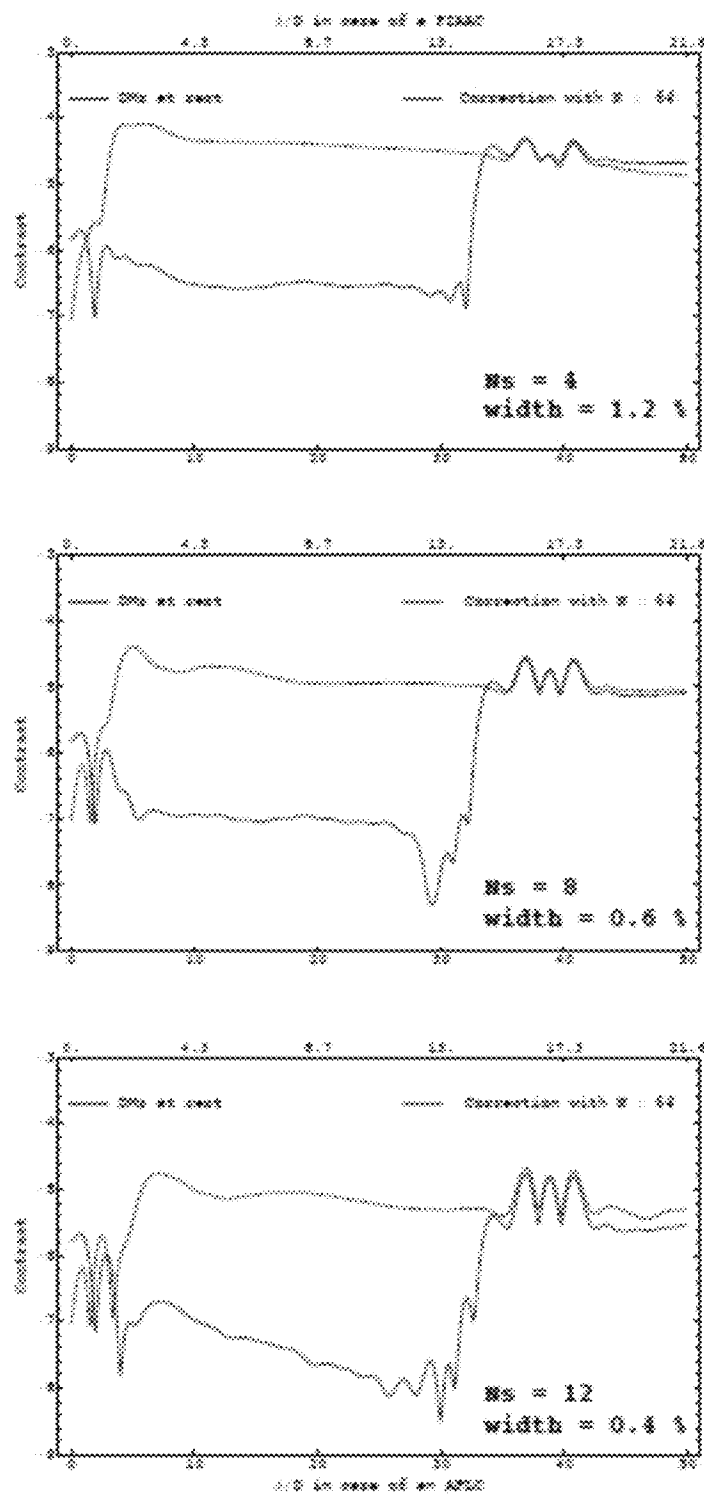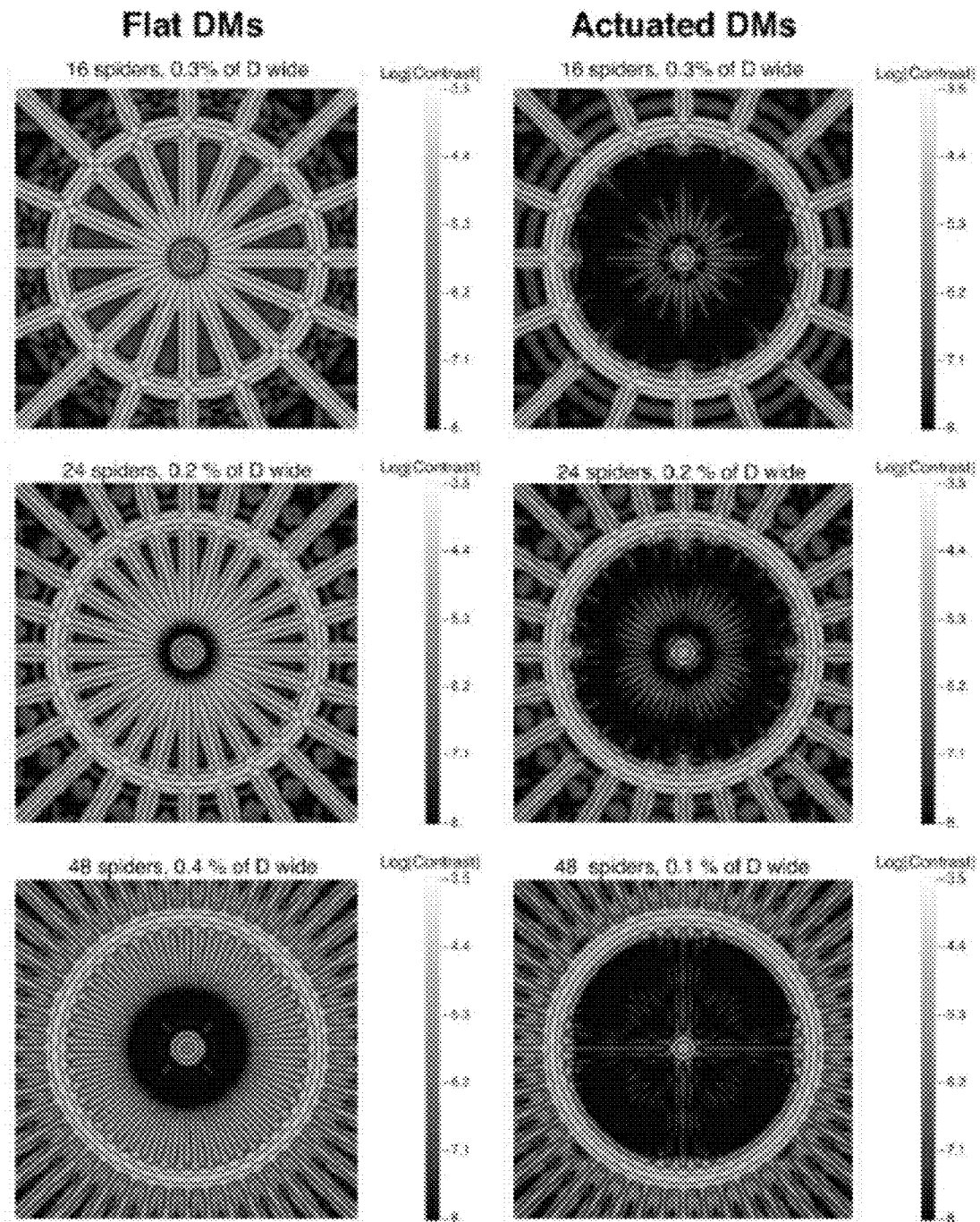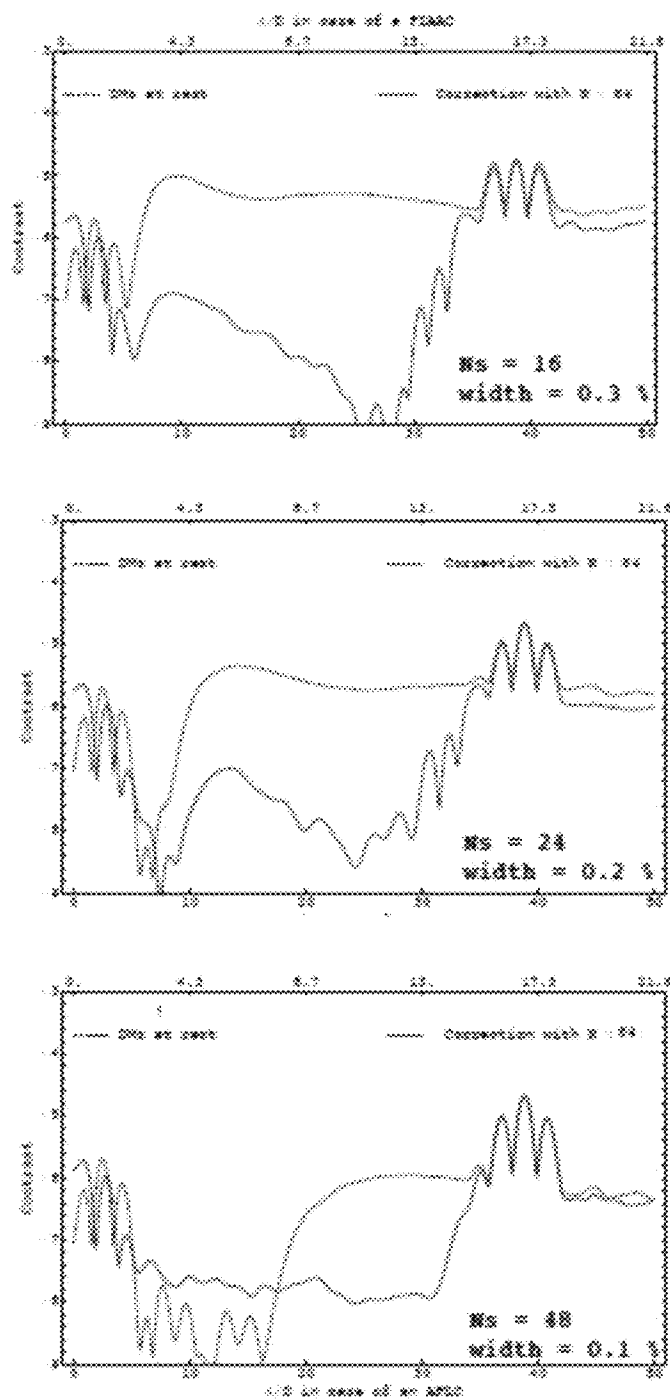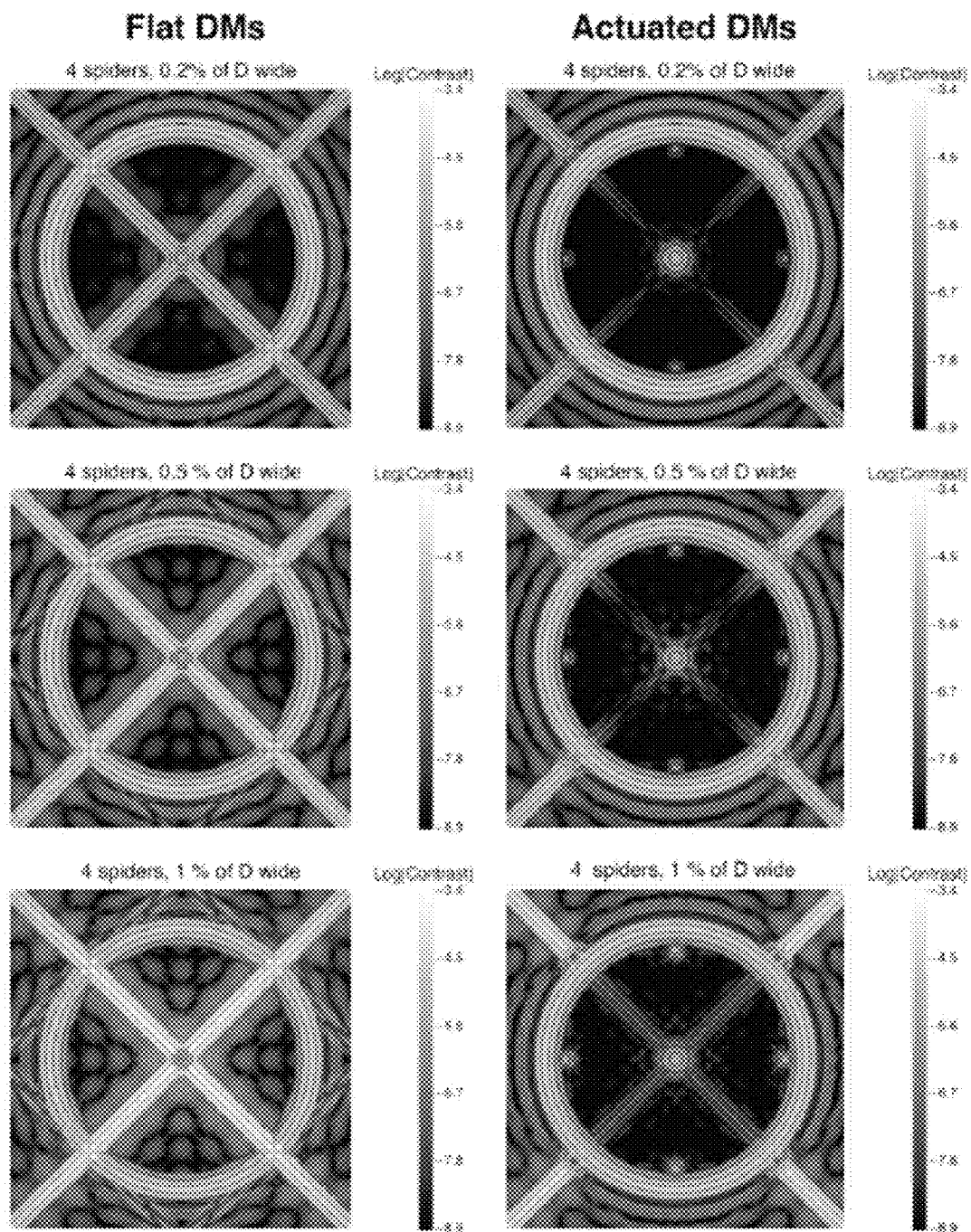
FIG. 21

FIG. 22

FIG. 23
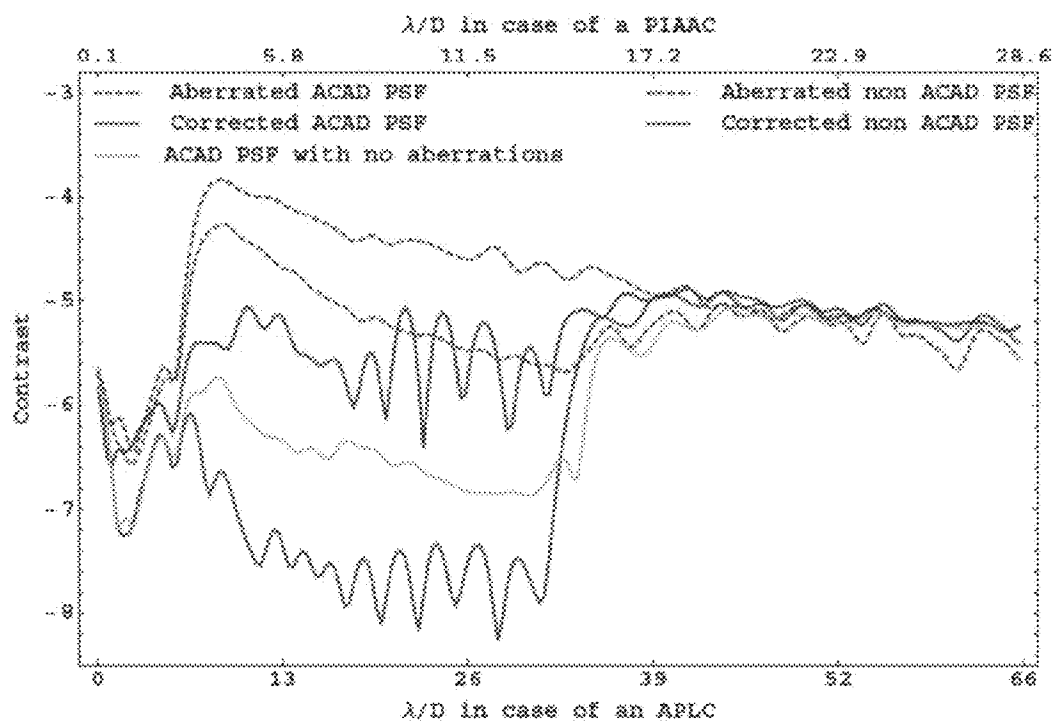
FIG. 24

FIG. 25
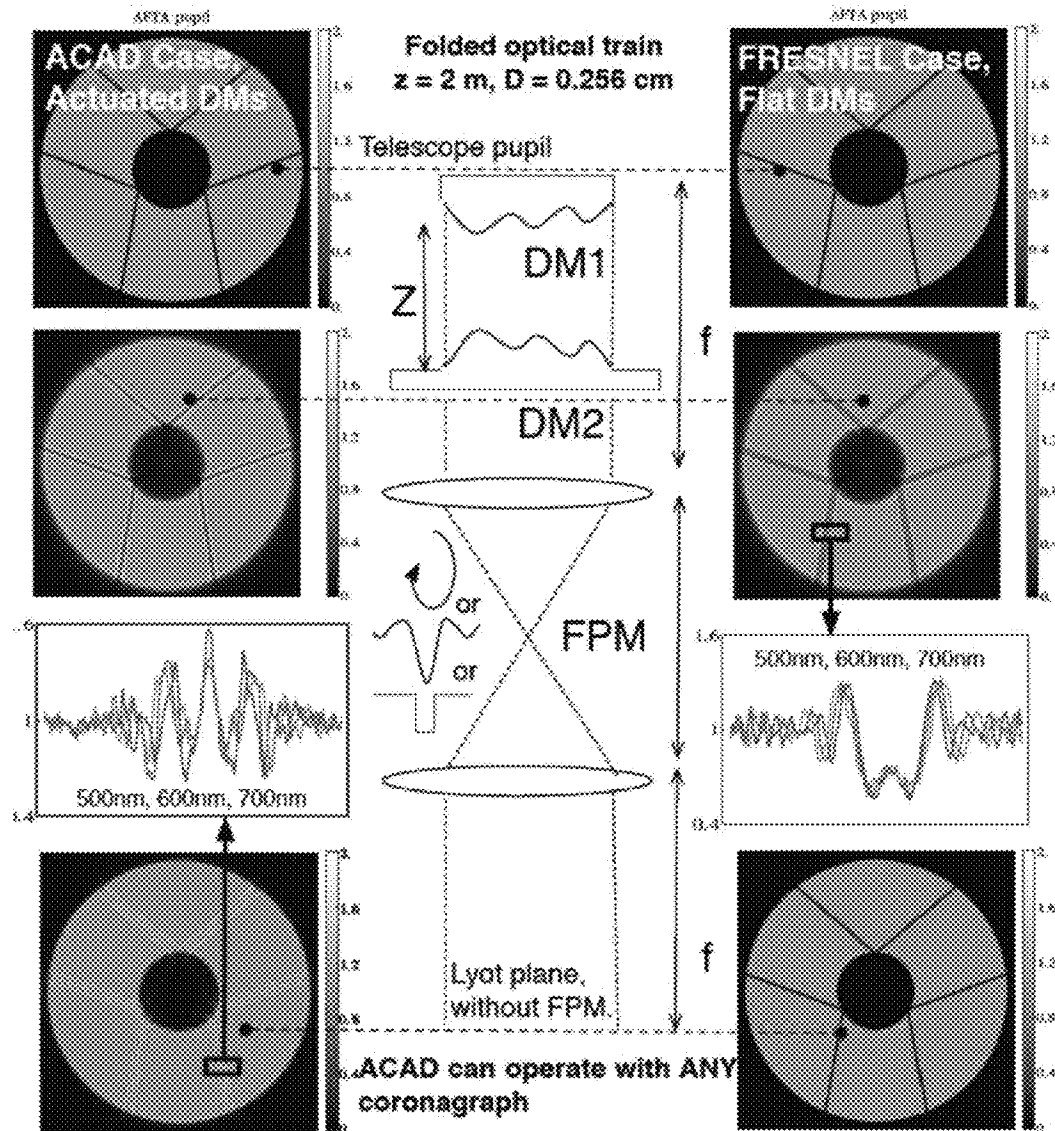
FIG. 26
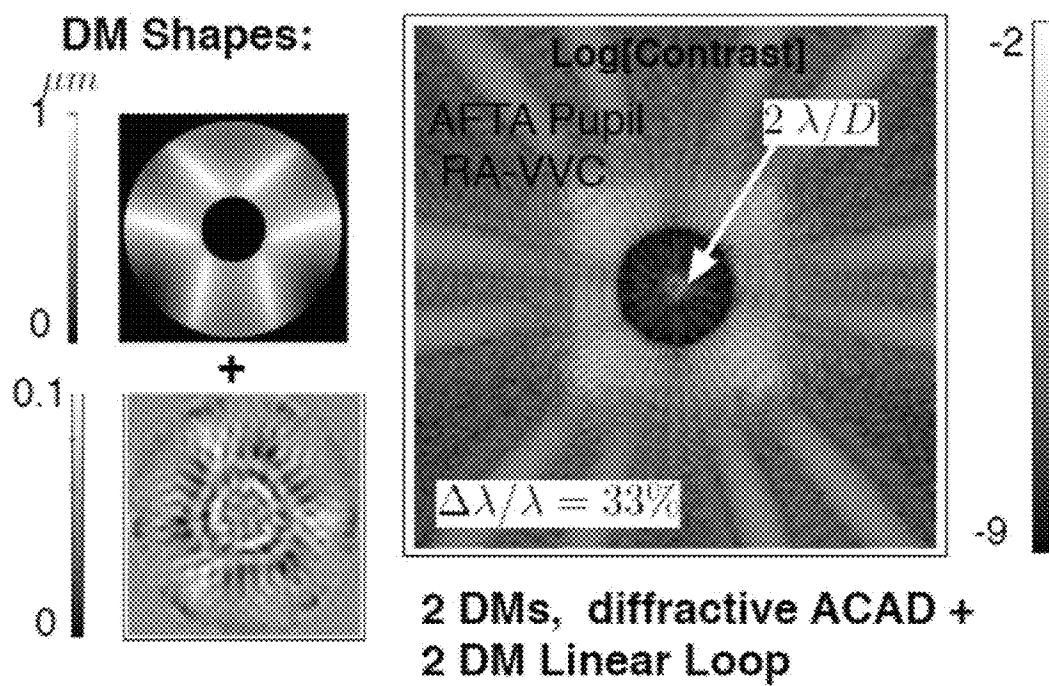
FIG. 27

ACTIVE BEAM SHAPING SYSTEM AND METHOD USING SEQUENTIAL DEFORMABLE MIRRORS

FEDERAL FUNDING BY THE U.S. GOVERNMENT

This invention was made with Government support of Grant No. NAS7-03001, awarded by the National Aeronautics and Space Administration (NASA). The U.S. Government has certain rights in this invention.

BACKGROUND

1. Field of Invention

The field of the currently claimed embodiments of this invention relates to active optical beam shaping systems and methods, and more particularly to active optical beam shaping systems and methods using sequential deformable mirrors.

2. Discussion of Related Art

Exo-planetary systems that are directly imaged using existing facilities (Marois et al. 2008; Kalas et al. 2008; Lagrange et al. 2010) give a unique laboratory to constrain planetary formation at wide separations (Rafikov 2005; Dodson-Robinson et al. 2009; Kratter et al. 2010; Johnson et al. 2010), to study the planetary luminosity distribution at critical young ages (Spiegel & Burrows 2012; Fortney et al. 2008) and the atmospheric properties of low surface gravity objects (Barman et al. 2011b,a; Marley et al. 2010; Madhusudhan et al. 2011). Upcoming surveys, conducted with instruments specifically designed for high-contrast (Dohlen et al. 2006; Graham et al. 2007; Hinkley et al. 2011), will unravel the bulk of this population of self-luminous Jovian planets and provide an unprecedented und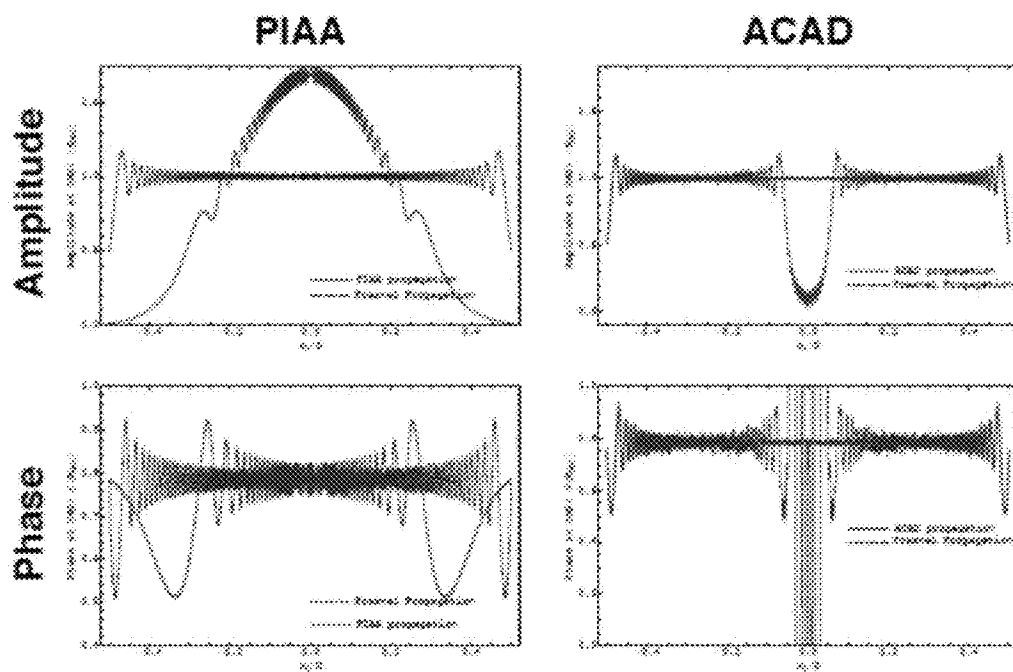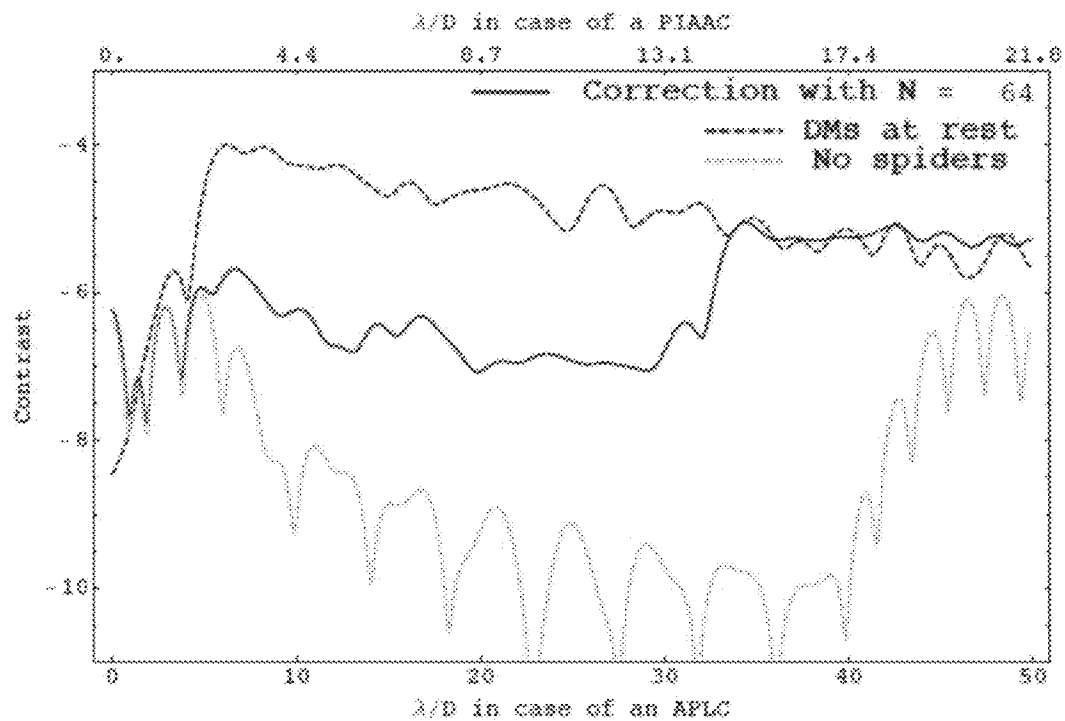erstanding of their formation history. Such instruments will reach the contrast required to achieve their scientific goals by combining Extreme Adaptive Optics systems (Ex-AO, Poyneer & V'eran (2005)), optimized coronagraphs (Soummer et al. 2011; Guyon 2003; Rouan et al. 2000) and nanometer class wavefront calibration (Sauvage et al. 2007; Wallace et al. 2009; Pueyo et al. 2010). In the future, high-contrast instruments on Extremely Large Telescopes will focus on probing planetary formation in distant star forming regions (Macintosh et al. 2006), characterizing both the spectra of cooler gas giants (V'erinaud et al. 2010) and the reflected light of planets in the habitable zone of low mass stars. The formidable contrast necessary to investigate the presence of biomarkers at the surface of earth analogs ($>10^{10}$) cannot be achieved from the ground beneath atmospheric turbulence and will require dedicated space-based instruments (Guyon 2005).

The coronagraphs that will equip upcoming Ex-AO instruments on 8 meter class telescopes have been designed for contrasts of at most $\sim10^{-7}$. Secondary support structure (or spiders: 4 struts each 1 cm wide, $\sim0.3\%$ of the total pupil diameter in the case of Gemini South) have a small impact on starlight extinction at such levels of contrasts. In this case, coronagraphs have thus been optimized on circularly symmetric apertures, which only take into account the central obscuration (Soummer et al. 2011). However, high-contrast instrumentation on future observatories will not benefit from such gentle circumstances. ELTs will have to support a substantially heavier secondary than 8 meter class observatories do, and over larger lengths: as a consequence, the relative area covered by the secondary support will increase by a factor of 10 (30 cm wide spiders, occupying $\sim3\%$ of the pupil diameter in the case of TMT). This will degrade the contrast of coro-

nagraphs only designed for circularly obscured geometries by a factor ~100, when the actual envisioned contrast for an ELT e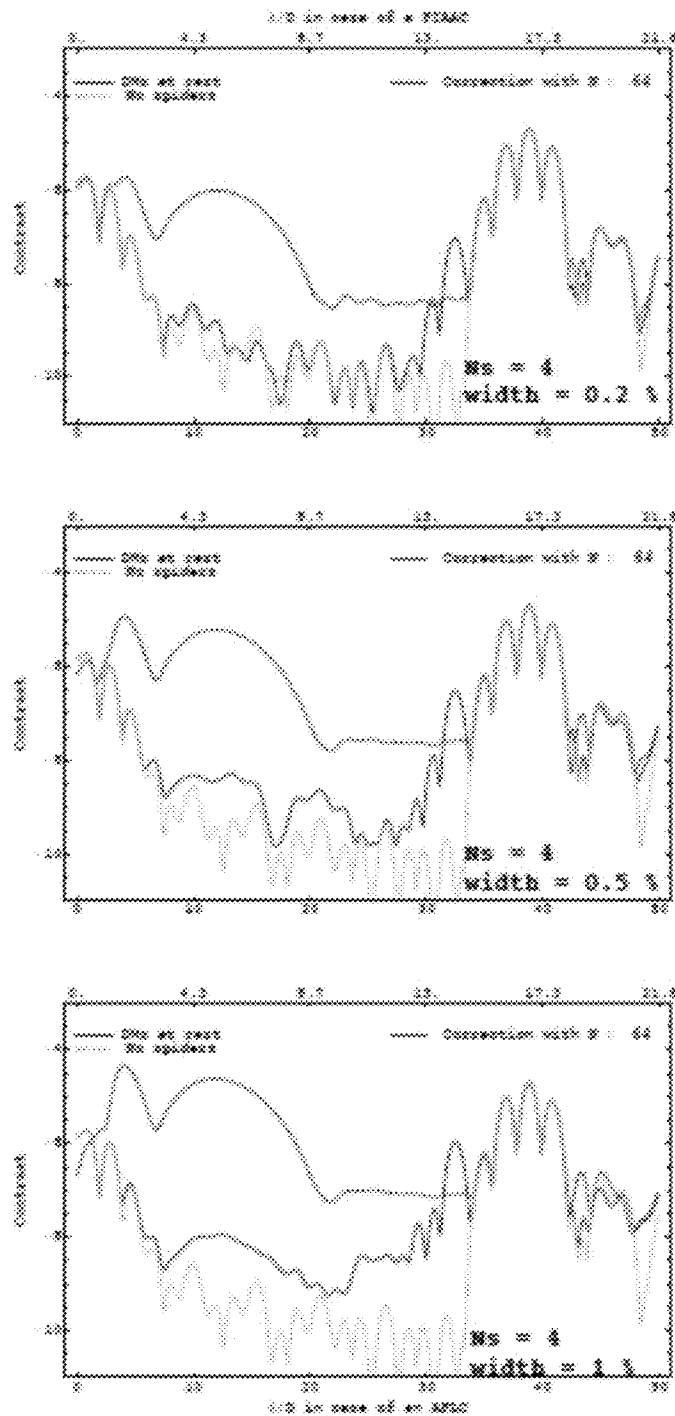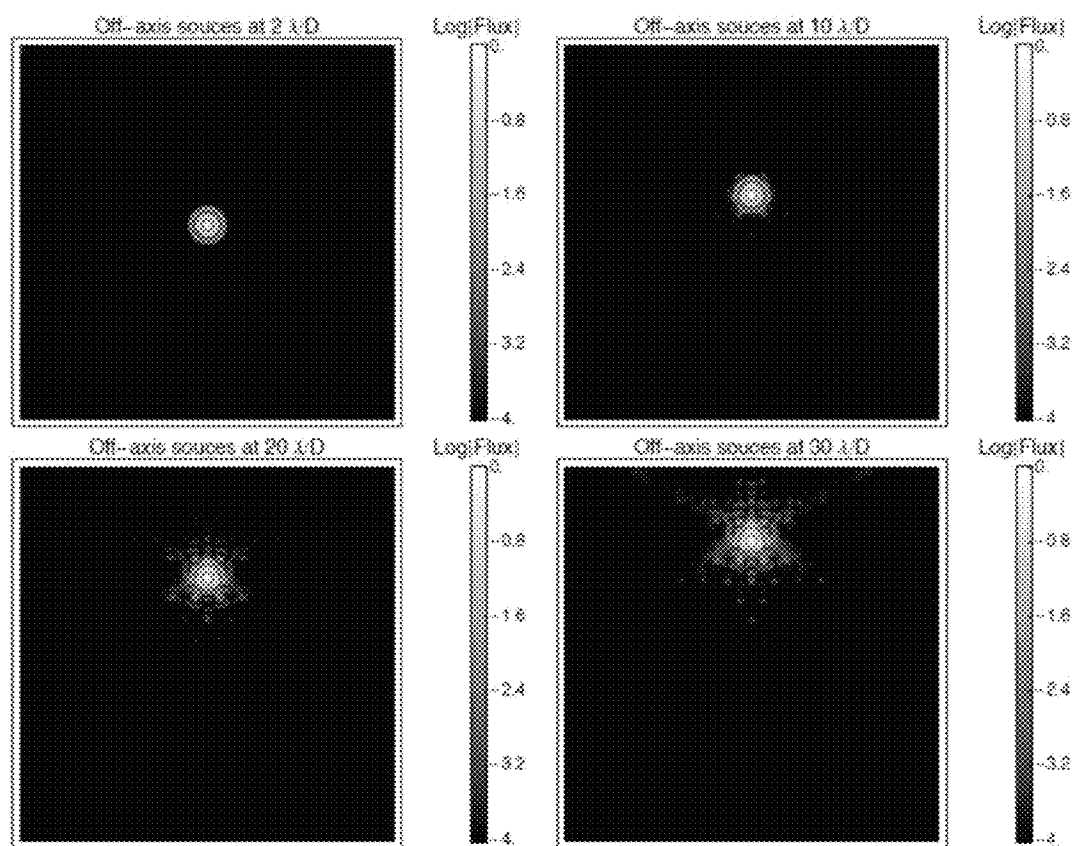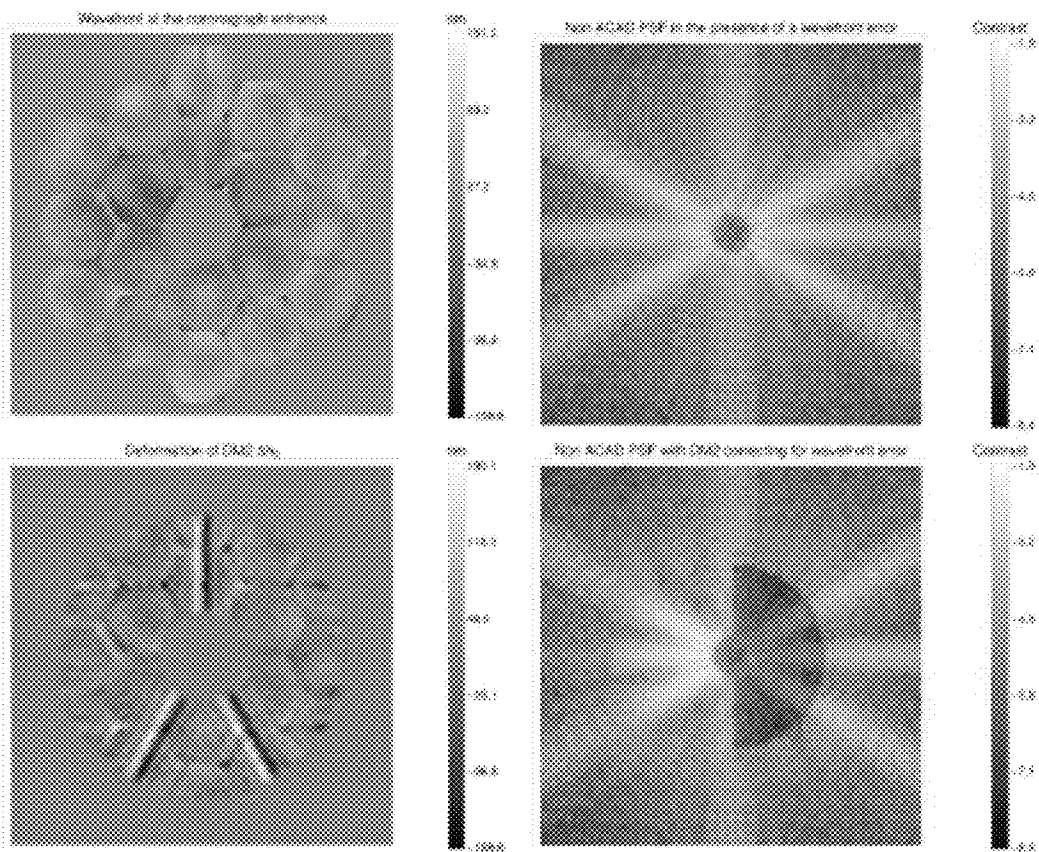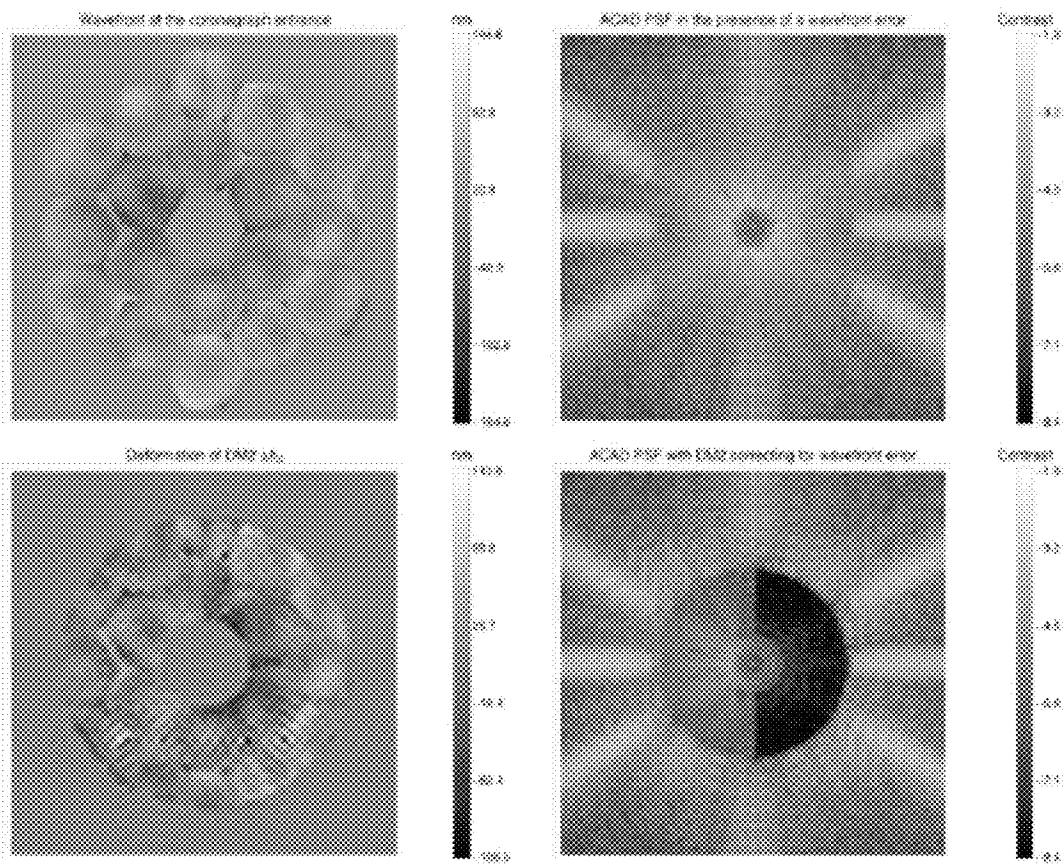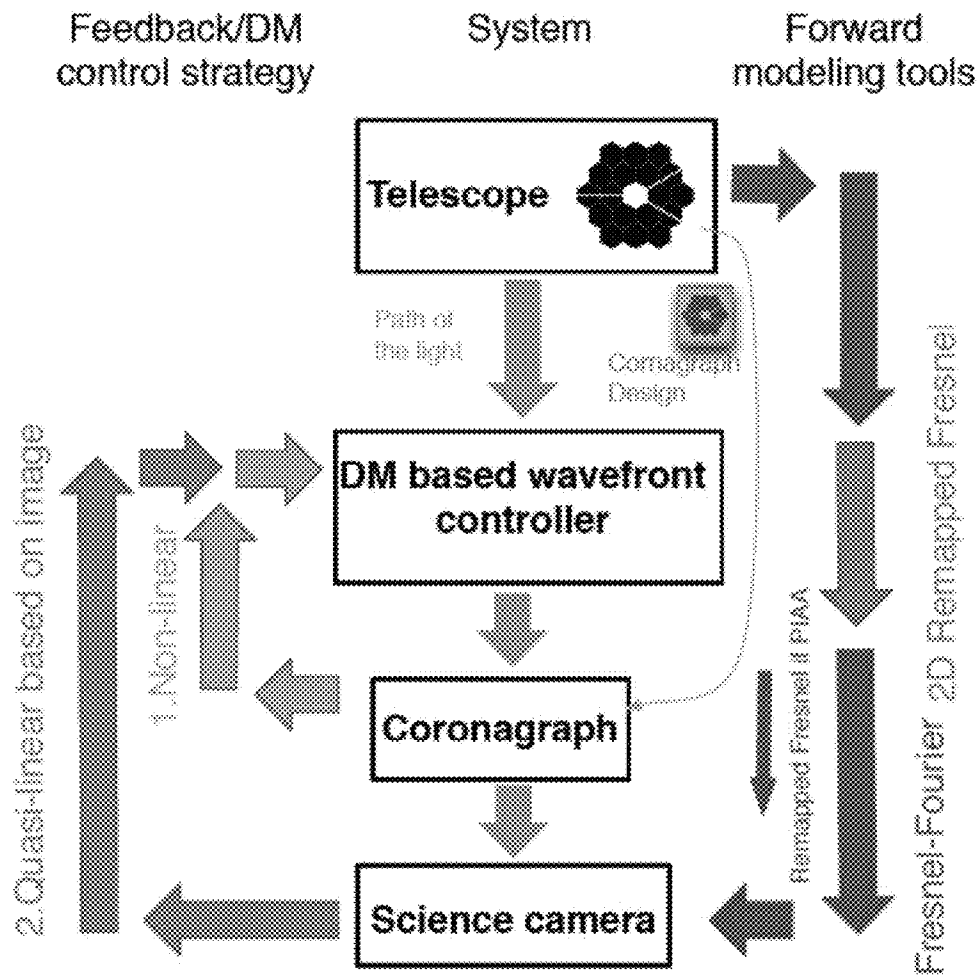xo-planet imager can be as low as $\sim10^{-8}$ (Macintosh et al. 2006). While the trade-offs associated with minimization of spider width in the space-based case have yet to be explored, secondary support structures will certainly hamper the contrast depth of coronagraphic instruments of such observatories at levels that are well above the 10^{10} contrast requirement. As a consequence, telescope architectures currently envisioned for direct characterization of exo-earths consist of monolithic, off-axis, and thus un-obscured, telescopes (Guyon et al. 2008; Trauger et al. 2010). Coronagraphs for such architectures take advantage of the pupil symmetry to reach a theoretical contrast of ten orders of magnitude (Guyon et al. 2005; Vanderbei et al. 2003a,b; Kasdin et al. 2005; Mawet et al, 2010; Kuchner & Traub 2002; Soummer et al. 2003). However, using obscured on-axis and/or segmented apertures take full advantage of the limited real estate associated with a given launch vehicle and can allow larger apertures that increase the scientific return of space-based direct imaging survey. Recent solutions can mitigate the presence of secondary support structures in on-axis apertures. However these concepts present practical limitations: APLCs on arbitrary apertures (Soummer et al. 2009) and Shaped Pupils (Carlotti et al. 2011) suffer from throughput loss for very high contrast designs, and PIAAMCM (Guyon et al. 2010a) rely on a phase mask technology whose chromatic properties have not yet been fully characterized. Moreover, segmentation will further complicate the structure of the telescope's pupil: both the amplitude discontinuities created by the segments gaps and the phase discontinuities resulting from imperfect phasing will thus further degrade coronagraphic contrast. Devising a practical solution for broadband coronagraphy on asymmetric, unfriendly apertures is an outstanding problem in high contrast instrumentation. Therefore, there remains a need for improved beam shaping systems and methods.

SUMMARY

An active optical beam shaping system according to an embodiment of the current invention includes a first deformable mirror arranged to at least partially intercept an entrance beam of light and to provide a first reflected beam of light, a second deformable mirror arranged to at least partially intercept the first reflected beam of light from the first deformable mirror and to provide a second reflected beam of light, and a signal processing and control system configured to communicate with the first and second deformable mirrors. The signal processing and control system is configured to provide control signals to the first deformable mirror so as to configure a reflecting surface of the first deformable mirror to substantially conform to a calculated surface shape so that the first reflected beam of light will have a predetermined amplitude profile. The signal processing and control system is further configured to provide control signals to the second deformable mirror to configure a reflecting surface of the second deformable mirror to substantially conform to a calculated surface shape so that a phase delay profile across the second reflected beam of light will be substantially constant when a phase delay profile across the entrance beam of light is substantially constant. The first deformable mirror, the second deformable mirror and the signal processing and control system together provide a large amplitude light modulation range to provide an actively shaped optical beam.

An optical transmitter according to an embodiment of the current invention includes an optical source, and an optical modulator arranged in an optical path of the optical source.

The optical modulator includes a first deformable mirror arranged to at least partially intercept an entrance beam of light from the optical source and to provide a first reflected beam of light, a second deformable mirror arranged to at least partially intercept the first reflected beam of light from the first deformable mirror and to provide a second reflected beam of light, and a signal processing and control system configured to communicate with the first and second deformable mirrors. The signal processing and control system is configured to provide control signals to the first deformable mirror and the second deformable mirror to provide at least a portion of the second reflected beam of light as an output beam having at least one of a selectable amplitude profile or selectable phase profile.

An optical receiver according to an embodiment of the current invention includes an optical detector, and an optical filter arranged in an optical path of the optical detector. The optical filter includes a first deformable mirror arranged to at least partially intercept an entrance beam of light being detected to provide a first reflected beam of light, a second deformable mirror arranged to at least partially intercept the first reflected beam of light from the first deformable mirror and to provide a second reflected beam of light, and a signal processing and control system configured to communicate with the first and second deformable mirrors. The signal processing and control system is configured to provide control signals to the first deformable mirror and the second deformable mirror to provide at least a portion of the second reflected beam of light as an output beam directed to the optical detector having at least one of a selectable amplitude profile or selectable phase profile.

An optical communication system according to an embodiment of the current invention includes an optical transmitter, an optical transmission path optically coupled to the optical transmitter, and an optical receiver optically coupled to the optical transmission path. At least one of the optical transmitter, the optical transmission path, or the optical receiver includes an active optical beam shaper. The active optical beam shaper includes a first deformable mirror arranged to at least partially intercept an entrance beam of light to provide a first reflected beam of light, a second deformable mirror arranged to at least partially intercept the first reflected beam of light from the first deformable mirror and to provide a second reflected beam of light, and a signal processing and control system configured to communicate with the first and second deformable mirrors. The signal processing and control system is configured to provide control signals to the first deformable mirror and the second deformable mirror to provide at least a portion of the second reflected beam of light as an output beam having at least one of a selectable amplitude profile or selectable phase profile.

An optical telescope according to an embodiment of the current invention includes a light collection and magnification system, an active optical beam shaper arranged in an optical path of light collected and magnified by the light collection and magnification system, and an optical detection system arranged to receive a beam of light from the active optical beam shaper. The active optical beam shaper includes a first deformable mirror arranged to at least partially intercept an entrance beam of light to provide a first reflected beam of light, a second deformable mirror arranged to at least partially intercept the first reflected beam of light from the first deformable mirror and to provide a second reflected beam of light, and a signal processing and control system configured to communicate with the first and second deformable mirrors. The signal processing and control system is configured to provide control signals to the first deformable

mirror and the second deformable mirror to provide at least a portion of the second reflected beam of light as an output beam having at least one of a selectable amplitude profile or selectable phase profile.

A solar furnace according to an embodiment of the current invention includes a light collection system, an active optical beam shaper arranged in an optical path of light collected by the light collection system, and an optical focusing system arranged to receive a beam of light from the active optical beam shaper to be focused on an object to be heated. The active optical beam shaper includes a first deformable mirror arranged to at least partially intercept an entrance beam of light to provide a first reflected beam of light, a second deformable mirror arranged to at least partially intercept the first reflected beam of light from the first deformable mirror and to provide a second reflected beam of light, and a signal processing and control system configured to communicate with the first and second deformable mirrors. The signal processing and control system is configured to provide control signals to the first deformable mirror and the second deformable mirror to provide at least a portion of the second reflected beam of light as an output beam having at least one of a selectable amplitude profile or selectable phase profile.

An optical pulse-shaping system according to an embodiment of the current invention includes an optical pulse source, a first diffraction grating disposed in an optical path of the optical pulse source, an active optical beam shaper disposed in an optical path of light diffracted from the first diffraction grating, and a second diffraction grating disposed in an optical path of light output from the active optical beam shaper. The active optical beam shaper includes a first deformable mirror arranged to at least partially intercept an entrance beam of light to provide a first reflected beam of light, a second deformable mirror arranged to at least partially intercept the first reflected beam of light from the first deformable mirror and to provide a second reflected beam of light, and a signal processing and control system configured to communicate with the first and second deformable mirrors. The signal processing and control system is configured to provide control signals to the first deformable mirror and the second deformable mirror to provide at least a portion of the second reflected beam of light as an output beam having at least one of a selectable amplitude profile or selectable phase profile.

BRIEF DESCRIPTION OF THE DRAWINGS

Further objectives and advantages will become apparent from a consideration of the description, drawings, and examples.

FIG. 1A is a schematic illustration of an active optical beam shaping system according to an embodiment of the current invention.

FIG. 1B is a schematic illustration of an optical transmitter according to an embodiment of the current invention.

FIG. 1C is a schematic illustration of laser beam launch system according to an embodiment of the current invention.

FIG. 1D is a schematic illustration of an optical receiver according to an embodiment of the current invention.

FIG. 1E is a schematic illustration of a solar furnace according to an embodiment of the current invention.

FIG. 1F is a schematic of a beam shaping device according to an embodiment of the current invention. Some advantages of beam shaping can include: (1) Can put more energy in a pulse. These can be ultra-short, high energy femtosecond pulses. Can include applications to laser fusion. (2) Can actively correct for beam aberrations that do not degrade the gratings.

FIG. 1G is a schematic illustration of a telescope according to an embodiment of the current invention. Top: Architecture applicable to future exo-earth imaging missions: a monolithic un-obscured telescope feeds a coronagraph designed on a circular aperture. The wavefront errors are corrected using two sequential Deformable Mirrors (DMs) that are controlled using a quasi-linear feedback loop based on image plane diagnostics. The propagation between optical surfaces, between the DMs in particular is assumed to occur in the Fresnel regime. Bottom: ACAD solution: the coronagraph is designed for a circular geometry around the central obscuration. The two sequential DMs are controlled in the non-linear regime based on a pupil plane cost function. The propagation between the DMs is modeled using ray optics, and we conduct a quantitative one-dimensional analysis of the diffraction artifacts.

FIG. 1H is a schematic illustration to help explain some concepts of some embodiments of the current invention.

FIG. 2 shows optimally designed Apodized Pupil Lyot Coronagraphs on circularly obscured apertures. With fixed obscuration ratio, size of opaque focal plane mask, IWA and OWA, our linear programming approach yields solutions with theoretical contrast below 10^{10}. All PSFs shown on this figure are monochromatic for $\lambda=\lambda_0$. When all other quantities remain equal and the central obscuration ratio increases (from 10% in the top panel to 20% in the middle panel), then the solution becomes more oscillatory (e.g less feasible) and the contrast constraint has to be relaxed. Eventually the optimizer does not find a solution and the size of the opaque focal plane mask (and thus the IWA) has to be increased (central obscuration of 30% in the bottom panel). On the right hand side, we present our results in two configurations: when the apodization is achieved using at grayscale screen (APLC), "on-sky" λ/D bottom x-axis, and when the apodization is achieved via two pupil remapping mirrors (PIAAC), "on-sky" λ/D top x-axis. We adopt this presentation to show that ACAD is "coronagraph independent" and that it can be applied to coronagraphs with high throughput and small IWA.

FIG. 3 shows a schematic of the optical system considered: the telescope aperture is followed by two sequential Deformable Mirrors (DMs) in non-conjugate planes whose purpose is to remap the pupil discontinuities. The beam then enters a coronagraph to suppress the bulk of the starlight: in this figure we show an Apodized Lyot Pupil Coronagraph (APLC). This is the coronagraphic architecture we consider for the remainder of the paper but we stress that the method presented herein is applicable to any coronagraph.

FIG. 4 Top: In the ideal case, the two DMs would fully remap all the discontinuities in the telescope's aperture to feed a fully uniform beam to the coronagraph. However this would require discontinuities in the mirror's curvatures which are not achieved in practice. Moreover solving the Monge-Ampere Equation in this direction is a difficult exercise as the right hand side of Eq. 26 presents an implicit dependence on the solution h_2.

Bottom: We circumvent this problem by solving the reverse problem, where the the input beam is now uniform and the implicit dependence drops out. Moreover we taper the edges of the discontinuities by convolving the target field $A(x_1,y_1)$ by a gaussian of full width at half maximum ω ($\omega=50$ cycles per aperture in this figure).

FIG. 5 shows forward and reverse coordinate systems, with their respective forward and reverse coordinate transforms, in the case of the folded system studied in this example. Note that this figure shows normalized units. As explained in the

body of the text the correspondence between normalized and real units scales as follow: $(x_i,y_i)=(DX_i,DY_i)$, $(f_i,g_i)=(DF_i, DG_i)$,

$$H_i = \frac{D^2}{Z} h_i,$$

where i=1, 2, D is the aperture diameter and Z the separation between DMs. We solve the Monge-Ampere Equation in normalized coordinates and then apply the scalings in order to find the true DM shapes.

FIG. 6 shows the virtual field at M1 when solving the reverse problem, $A(X_1,Y_1)$ is the desired apodization (top), $A_n(X_1,Y_1)$ is the apodization obtained after solving the Monge-Ampere Equation (center). The bottom panel shows the difference between the two quantities: the bulk of the energy in the residual is located in high spatial frequencies that cannot be controlled by the DMs.

FIG. 7 shows boundary conditions seen in the horizontal remapped space. Should the boundary conditions have strictly been enforced by our solver then

$$F_2\left(-\frac{1}{2}, Y\right) = -\frac{1}{2}, F_2\left(\frac{1}{2}, Y\right) = \frac{1}{2},$$

$$F_2\left(X, -\frac{1}{2}\right) = X, F_2\left(X, \frac{1}{2}\right) = X.$$

The remapping function obtained with our solutions is very close to these theoretical boundary conditions and the residuals can easily be mitigated by sacrificing the edge rows and columns of actuators on each DM.

FIG. 8 shows boundary conditions seen in the vertical remapped space. Should the boundary conditions have strictly been enforced by our solver then

$$G_2\left(-\frac{1}{2}, Y\right) = Y, G_2\left(\frac{1}{2}, Y\right) = Y,$$

$$G_2\left(X, -\frac{1}{2}\right) = -\frac{1}{2}, G_2\left(X, \frac{1}{2}\right) = \frac{1}{2}.$$

The remapping function obtained with our solutions is very close to these theoretical boundary conditions and the residuals can easily be mitigated by sacrificing the edge rows and columns of actuators on each DM.

FIG. 9 shows beam amplitude before and after the DMs in the case of a geometry similar to JWST. We chose to solve the reverse problem over a square using a Fourier basis set and not strictly enforcing boundary conditions. This results in small distortions of the edges of the actual aperture in the vicinity of segments gaps and secondary supports. We address this problem by slightly oversizing the secondary obscuration and undersizing the aperture edge in the coronagraph.

FIG. 10, Left: Comparison of edge diffraction between PIAA and Fresnel propagation. Because the discontinuities in the pupil occur at the location where $\Gamma_x<1$, a PIAA amplifies the chromatic ringing when compared to a more classical propagation. Right: Comparison of edge diffraction between ACAD and Fresnel propagation. Because the discontinuities in the pupil occur at the location where $\Gamma_x>1$, a ACAD damps the chromatic ringing when compared to a more classical propagation. These simulations were carried out for a one dimensional aperture. In this case the Monge-Ampere Equa-

tion can be solved using finite elements and the calculation of the diffractive effects reduces to the evaluation of various Fresnel special functions at varying wavelength. The full two-dimensional problem is not separable and requires the development of novel numerical tools.

FIG. **11** Results obtained when applying our approach to a geometry similar to JWST. We used two 3 cm DMs of 64 actuators separated by 1 m. Their maximal surface deformation is 1.1 μm, well within the stroke limit of current DM technologies. The residual light in the corrected PSF follows the secondary support structures and can potentially be further cancelled by controlling the DMs using an image plane based cost function, see FIG. **23**.

FIG. **12** Case of JWST: Radial average obtained when applying ACAD. We used two 3 cm DMs of 64 actuators separated by 1 m. Their maximal surface deformation is 1.1 μm, well within the stroke limit of current DM technologies. ACAD yields a gain in contrast of two orders of magnitude, and provides contrasts levels similar to upcoming Ex-AO instruments, which are designed on much friendlier apertures geometries. Since ACAD removes the bulk of the light diffracted by the asymmetric aperture discontinuities, the final contrast can be improved by controlling the DMs using and image plane based cost function, see FIG. **23**.

FIG. **13** shows results obtained when applying our approach to a TMT geometry. We used two 3 cm DMs of 64 actuators separated by 1 m. Their maximal surface deformation is 0.9μ 0.9 μm, well within the stroke limit of current DM technologies. The final contrast is below 10^7 10^7, in a regime favorable for direct imaging of exo-planets with ELTs.

FIG. **14** Case of TMT: radial average obtained when applying ACAD. We used two 3 cm DMs of 64 actuators separated by 1 m. Their maximal surface deformation is 0.9 μ 0.9 μm, well within the stroke limit of current DM technologies. The final contrast is below 1.0^7 10^7, in a regime favorable for direct imaging of exo-planets with ELTs. Since ACAD removes the bulk of the light diffracted by the asymmetric aperture discontinuities, the final contrast can be enhanced by controlling the DMs using and image plane based metric.

FIG. **15** shows PSFs resulting from ACAD when varying the number and thickness of secondary support structures while maintaining their covered surface constant. The surface area covered in this example is 50% greater than in the TMT example shown on FIG. **13**. As the spiders get thinner their impact on raw contrast becomes smaller and the starlight suppression after DM correction becomes bigger. For a relatively small number of spiders (<12) the contrast improvement on each single structure is the dominant phenomenon, regardless of the number of spiders. ELTs designed with a moderate to large number of thin secondary support structure (6 to 12) present aperture discontinuities which are easy to correct with ACAD.

FIG. **16** shows radial PSF profiles resulting from ACAD when varying the number and thickness of secondary support structures while maintaining their covered surface constant. The surface area covered in this example is 50% greater than in the TMT example shown on FIG. **13**. As the spiders get thinner their impact on raw contrast becomes lesser and the starlight suppression after DM correction becomes greater. In the 12 spiders example, at large separations, the average contrast is an order of magnitude higher than reported on FIG. **14**.

FIG. **17** shows PSFs resulting from ACAD when varying the number and thickness of secondary support structures while maintaining their covered surface constant. The surface area covered in this example is 50% greater than in the TMT example shown on FIG. **13**. When the number of spiders

increases, they produce a sharp circular diffraction feature at $N_{Spiders}/\pi$ λ/D. If this number is greater than the size of the focal plane mask this structure appears in the high contrast zone and is very difficult to correct with ACAD. The brightness of this structure is mitigated by the fact that the spiders are very thin.

FIG. **18** shows radial PSF profiles resulting from ACAD when varying the number and thickness of secondary support structures while maintaining their covered surface constant. The surface area covered in this example is 50% greater than in the TMT example shown on FIG. **13**. With a large number of spiders the bright ring in the PSF structure located at $N_{Spiders}/\pi$ λ/D is difficult to correct with ACAD. However, since the spiders become thinner their net effect on contrast after ACAD remains small.

FIG. **19** shows PSFs resulting from ACAD when varying the number and thickness of secondary support structures. As the spiders get thinner their impact on raw contrast becomes lesser and the starlight suppression after DM correction becomes greater. In this case ω was optimized on a very fine grid and the aperture we clocked in a favorable direction with respect to the Fourier basis.

FIG. **20** shows PFSs resulting from ACAD when varying the number and thickness of secondary support structures. As the spiders get thinner their impact on raw contrast becomes lesser and the starlight suppression after DM correction becomes greater. In this case ω was optimized on a very fine grid and the aperture we clocked in a favorable direction with respect to the Fourier basis. Even for spiders as thick as 0.5% of the telescope aperture the designed contrast of the coronagraph is retrieved.

FIG. **21** shows off-axis PSF after ACAD in the case of a geometry similar to JWST. The aspheric surface of the DMs introduces a slight field-dependent distortion. However the core of the PSF is still concentrated within the central airy disk and the DMs only have an effect on the PSF tail. Field distortion does not thus hamper the detectability of faint off-axis sources.

FIG. **22** shows broadband wavefront correction (20% bandwidth around 700 nm) with a single DM in segmented telescope with discontinuous surface errors. Top Left: wavefront before the coronagraph. Top Right: broadband aberrated PSF with DM at rest. Bottom Left: DM surface resulting from the wavefront control algorithm. Bottom Right: broadband corrected PSF. Note that the wavefront control algorithm seeks to compensate for the diffractive artifacts associated with the secondary support structures: it attenuates them on the right side of the PSF while it strengthens them on the left side of the PSF. As a result the DM surface becomes too large at the pupil spider's location and the quasi-linear wavefront control algorithm eventually diverges.

FIG. **23** shows broadband wavefront correction (20% bandwidth around 700 nm) in a segmented telescope whose pupil has been re-arranged using ACAD. The surface of the first DM is set according to the ACAD equations. The surface of the second DM is the sum of the ACAD solution and a small perturbation calculated using a quasi-linear wavefront control algorithm. Top Left: wavefront before the coronagraph. Note that the ACAD remapping has compressed the wavefront errors near the struts and the segment gaps. Top Right: broadband aberrated PSF with DMs set to the ACAD solution. Bottom Left: perturbation of DM2's surface resulting from the wavefront control algorithm. Bottom Right: broadband corrected PSF. The wavefront control algorithm now yields a DM surface that does not feature prominent deformations at the location of the spiders. Most of the DM stroke is located at the edge of the segments, at location of the

wavefront discontinuities. There, the DM surface eventually becomes too large and the quasi-linear wavefront control algorithm diverges. However this results in higher contrasts than in the absence of ACAD.

FIG. 24 shows radial average in the half dark plane of the PSFs on FIG. 22 and FIG. 23. In the presence of wavefront discontinuities corrected using a continuous membrane DM, ACAD still yields, over a 20% bandwidth around 700 nm, PSF with a contrast 100 larger than in a classical segmented telescope. Moreover this figure illustrates that since it is based on a true image plane metric, the wavefront control algorithm can be used (within the limits of its linear regime) to improve upon the ACAD DM shapes derived solving the Monge-Ampere Equation.

FIG. 25 shows further embodiments for higher contrasts with ACAD. The blue and orange colors respectively represent the current state of the art in wavefront control and the work described in the present manuscript, as in FIG. 1G. In brown are listed avenues to further the contrasts presented herein: 1) combining ACAD with coronagraphs designed on segmented and/or on-axis apertures, 2) using diffractive models to close a quasi-linear focal plane based loop using a metric whose starting point corresponds to the DM shapes calculated in the non-linear regime.

FIG. 26 shows simulation of ACAD in the SR-Fresnel approximation. We simulated the propagation between DM1 and DM2 according to Eq. (59), and simulated the rest of the coronagraphic train using the Fresnel approximation. Fresnel propagation simply replicates the input pupil's (top panels) deep and sharp discontinuities in the final reimaged pupil (right bottom panel). ACAD SR-Fresnel instead transforms them into shallow and smooth mid-spatial frequency ripples (left bottom panel). The chromatic nature of these oscillations sets the ultimate bandwidth of ACAD, but unlike in PIAA coronagraphs the beam reshaping here does not amplify these oscillations any beyond normal edge ringing for out of pupil optics in the Fresnel regime (discussed in Pueyo and Kasdin, 2007). The plotted slices across the secondary support structures (middle panels) show that ripples in the SR-Fresnel approximation are neither bigger nor more chromatic than hard-edge induced ripples in the Fresnel approximation. This enables a broad spectral bandwidth. Note that in order to better illustrate the oscillations' chromatic nature this figure has been generated with a large separation between the DMs, $Z=2$ m. For more realistic separations ACAD exhibits a weaker chromatic behavior, as illustrated by FIG. 2. Here we intentionally omit the coronagraphic mask and Lyot stop to highlight that ACAD can operate with any coronagraph.

FIG. 27 shows ACAD in the SR-Fresnel diffractive optics regime +RA-VVC}: We demonstrate a simulated 30% bandwidth contrast of ~3×10^9 and an inner working angle of 2λ/D on the AFTA pupil using ACAD with two 1 inch DMs separated by 0.5 m. It demonstrates the weak chromaticity of ACAD and its ability to operate with a high throughput, small IWA coronagraph on an obscured aperture.

DETAILED DESCRIPTION

Some embodiments of the current invention are discussed in detail below. In describing embodiments, specific terminology is employed for the sake of clarity. However, the invention is not intended to be limited to the specific terminology so selected. A person skilled in the relevant art will recognize that other equivalent components can be employed and other methods developed without departing from the broad concepts of the current invention. All references cited anywhere in this specification, including the Background and

Detailed Description sections, are incorporated by reference as if each had been individually incorporated.

The terms "light" and "optical" are intended to have broad meanings to include both visible and non-visible regions of the electromagnetic spectrum. Visible, infrared, ultraviolet and x-ray regions of the electromagnetic spectrum are all intended to be included within the definition of the term "light".

FIG. 1A is a schematic illustration of an active optical beam shaping system 100 according to an embodiment of the current invention. The optical beam shaping system 100 includes a first deformable mirror 102 arranged to at least partially intercept an entrance beam of light 104 and to provide a first reflected beam of light 106, a second deformable mirror 108 arranged to at least partially intercept the first reflected beam of light 106 from the first deformable mirror 102 and to provide a second reflected beam of light 110, and a signal processing and control system 112 configured to communicate with the first and second deformable mirrors (102, 108). The signal processing and control system 112 is configured to provide control signals to the first deformable mirror 102 so as to configure a reflecting surface of the first deformable mirror 102 to substantially conform to a calculated surface shape so that the first reflected beam of light 106 will have a predetermined amplitude profile. The signal processing and control system 112 is further configured to provide control signals to the second deformable mirror 108 to configure a reflecting surface of the second deformable mirror 108 to substantially conform to a calculated surface shape so that a phase delay profile across the second reflected beam of light 110 will be substantially constant when a phase delay profile across the entrance beam of light 104 is substantially constant. When the phase delay of entrance beam of light 104 is not constant the signal processing and control system 112 can control the second deformable mirror 108 to make the phase delay of the second reflected beam of light 110 constant. The first deformable mirror 102, the second deformable mirror 108 and the signal processing and control system 112 together provide a large amplitude light modulation range to provide an actively shaped optical beam.

The term "deformable mirror" refers to an assembly that includes a reflecting surface as well as structural components that effect reconfiguration of the surface to substantially match calculated surface shapes. For example, the reflecting surface can be reconfigured into a plurality of complex non-spherical, non-parabolic and non-ellipsoidal surface shapes that can include a plurality of local convex and/or concave localized regions. The structural components of the deformable mirrors can include, but are not limited to, actuators.

The signal processing and control system 112 can be an application-specific and/or a general programmable system. For example, it can be implemented on a computer system and/or implemented on dedicated hardware such as an ASIC and/or FPGA. The signal processing system and control 112 can also include memory and/or data storage in addition to data processing components, such as, but not limited to a CPU and/or GPU. The signal processing and control functions can be incorporated together or performed on separate components, for example. The communication paths with the deformable mirrors can be hard wired, such as electrically wired or fiber optic, and/or wireless such as radio frequency (RF) and/or optical communications links, for example.

In an embodiment of the current invention, the large amplitude modulation range can be at least 1% of a fully illuminated portion of the entrance beam 104 of light. In an embodiment of the current invention, the large amplitude modulation range can be substantially an entire range to permit selectable

amplitude modulation of portions of the entrance beam **104** of light anywhere from substantially fully attenuated to substantially fully illuminated relative to fully illuminated portions of the entrance beam of light **104**. If the spatial scale amplitude or phase structures of interest of the incoming beam is $(\delta x, \delta y)$ $\sim O(\delta)$ (where δ is that distance between actuators, OR size of discontinuities between telescope pupil, OR solid angle of a fiber when coupling to a fiber, or scale of beam/over what info is encoded for laser can, or scale of beam perturbations), then the large amplitude modulation regime over this characteristic scale can be defined as follows:

Define

$$\left|\frac{\partial h}{\partial \vec{r}}\right|$$

the focal gradient of both mirror's surface at any arbitrary point on either the input or the output beam (FIG. 1H).

Define θ_s as the solid angle subtended by the disk or radius δ and the distance z between the DMs.

The radius δ is a characteristic scale of the beam that is sought to be reshaped, Z is a distance between the deformable mirrors, defined by a) the two points for which the optical surfaces of the DMs are the farthest one to another in the horizontal direction, and b) the length between the two tangent planes to the DM surfaces at those points. h_1 and h_2 are the surface deflections of each DM measured as the relative distance from each respective DM surface at the tangent planes at maximum horizontal length defined above.

Then the long amplitude modulation regime is defined when significant beam remapping occurs.

$$\left|\frac{\partial h}{\partial \vec{r}}\right| \geq 0(\theta_s) \qquad \text{Eqn (1)}$$

This rigorous expression can be translated in terms of the largest amplitude modulation ("a") in a simple case.

Assume we are seeking a 1D amplitude modulation:

$$1 + a\cos\left(\frac{2\pi}{D}nx\right)$$

Then under the assumption a<<1 one can seek:

$$h_1(x) = -h_2(x) = \epsilon \cos\left(\frac{2\pi}{D}nx\right)$$

with

$$\epsilon = \frac{n^2}{4\pi^2}\frac{D^2}{2}a$$

When in the "large amplitude modulation" regime the "a<<1" breaks down and, this simple solution is not valid, we have to solve the Monge-Ampere equation as per the present description.

Assuming that the characteristic scale of the input beam is

$$\frac{D}{N_{act}}$$

(actuator pitch) and that n is "as large as possible" in order not to lose generality, eg,

$$n = \frac{N_{act}}{2}.$$

Then folding this into Eqn (1) yields:

$$a_{crit} = \sigma\left(\frac{4\pi}{N_{act}}\right)$$

Namely, when N=32 we find a_{crit}=1.2% as previously stated in this specification, the boundary between "small" and "large" amplitude modulation is around 1%, but the above also provides a rigorous derivation. This is the rigorous definition that defines the boundary between small and large amplitude modulation regime for ALL applications.

In an embodiment of the current invention, the active optical beam shaping system **100** can further include a beam analyzer **114** arranged to receive at least a portion of the exit beam **110** of light reflected from the second deformable mirror **108**. In alternative embodiments, the beam analyzer **114** can receive external information regarding the medium or environment in which the second beam of light **110** will propagate. The beam analyzer **114** can be configured to communicate with the signal processing and control system **112** to provide feedback control of at least one of the first and second deformable mirrors (**102, 108**). The beam analyzer **114** can be hard wired by electrical and/or fiber optic connections to the signal processing and control system **112**, and/or in wireless communication such as by RF and/or optical wireless communications links. In some embodiments, the beam analyzer **114** can be further configured to estimate: (1) the amplitude profile of the beam and/or (2) the phase of the beam.

In an embodiment of the current invention, input **116** for a desired output beam shape can be provided to the signal processing and control system **112**. The input **116** information for the desired output beam shape can be used in conjunction with feedback signals from said beam analyzer **114** in some embodiments of the current invention. However, embodiments in which no feedback information is used are intended to be included within the general concepts of the current invention.

In an embodiment of the current invention, the signal processing and control system **112** can be further configured to calculate the surface shape of at least one of the first and second deformable mirrors (**102, 108**) based on reverse ray tracing calculations.

In an embodiment of the current invention, the signal processing and control system **112** can be further configured to calculate the surface shape of at least one of the first and second deformable mirrors based on a solution to Monge-Ampere equations corresponding to the active optical beam shaping system.

Further embodiments of the current invention are directed to numerous devices and systems that incorporate at least one

active optical beam shaping system according to an embodiment of the current invention. The following will describe some such devices and systems; however, one should recognize that further devices and systems, and modifications thereof, can be constructed with one or more active optical beam shaping systems according to an embodiment of the current invention and are considered to be included within the general scope of the current invention.

FIG. 1B is a schematic illustration of an optical transmitter 200 according to an embodiment of the current invention. The optical transmitter 200 includes an optical source 202 and an optical modulator 204 arranged in an optical path 206 of the optical source 202. The optical modulator 204 can be similar to or the same as the active optical beam shaping system 100, for example. The optical modulator 204 includes, similar to FIG. 1A and not shown in FIG. 1B, a first deformable mirror arranged to at least partially intercept an entrance beam of light from the optical source 202 and to provide a first reflected beam of light, a second deformable mirror arranged to at least partially intercept the first reflected beam of light from said first deformable mirror and to provide a second reflected beam of light, and a signal processing and control system configured to communicate with the first and second deformable mirrors. The signal processing and control system is configured to provide control signals to the first deformable mirror and the second deformable mirror to provide at least a portion of the second reflected beam of light as an output beam 207 having at least one of a selectable amplitude profile or selectable phase profile.

The optical transmitter 200 can further include a beam analyzer 208 configured to sample a portion of the output beam 207. For example, the optical transmitter 200 can include a beam splitter 210, such as a partially silvered mirror or a dichroic mirror arranged in the output beam 207 to redirect a portion of the output beam 207 to beam analyzer 208. However, the general concepts of the current invention are not limited to this particular example. The beam analyzer can be, but is not limited to, a camera and/or a wavefront sensor, for example.

The optical transmitter 200 can be used in, but is not limited to, optical communications systems for example. Such optical communications systems can be free space systems, or can be waveguide systems, for example. Waveguide systems can include, but are not limited to, fiber optic systems. The term "free space" is intended to have a general meaning to include vacuum propagation, such as between satellites and/or spacecraft, or through a medium such as the atmosphere, and/or water.

In some embodiments, the signal processing and control system of the optical transmitter 200 can be configured to provide control signals to the first deformable mirror and the second deformable mirror such that the output beam has both a selectable amplitude profile and selectable phase profile. In some embodiments, the signal processing and control system of the optical transmitter 200 can be configured to provide control signals to the first deformable mirror and the second deformable mirror such that the output beam of light 207 is soliton pulses. The soliton boundary conditions can be input to the signal processing and control system, for example. For a given fiber we do not calculate the soliton shape here. However, we can couple to the fiber any prescribed solitons and keep accurately their profile in the presence of disturbances.

The solitons can be coupled into an optical fiber, for example, for long distance fiber optic communication without

the need for repeaters for signal regeneration, for example. This can be useful for transoceanic fiber optic systems, for example.

FIG. 1C is a schematic illustration of laser beam launch system 220 according to an embodiment of the current invention. It includes an optical transmitter 222 and reflecting telescope 224. The optical transmitter 222 can be the same or similar to optical transmitter 200, for example. Some applications of laser beam launch system 220 can include, but are not limited to, tactical and strategic shooting down of satellites.

FIG. 1D is a schematic illustration of an optical receiver 300, according to an embodiment of the current invention. The optical receiver 300 includes an optical detector 302 and an optical filter 304 arranged in an optical path of the optical detector 320. The optical filter can be similar to or the same as the active optical beam shaping system 100, for example. The optical filter 304 includes a first deformable mirror arranged to at least partially intercept an entrance beam of light being detected to provide a first reflected beam of light, a second deformable mirror arranged to at least partially intercept the first reflected beam of light from the first deformable mirror and to provide a second reflected beam of light, and a signal processing and control system configured to communicate with the first and second deformable mirrors, (Also, see, e.g., FIG. 1A.) The signal processing and control system is configured to provide control signals to the first deformable mirror and the second deformable mirror to provide at least a portion of the second reflected beam of light as an output beam directed to the optical detector to have at least one of a selectable amplitude profile or selectable phase profile.

The optical receiver 300 can further include a beam analyzer 306 configured to communicate with the optical filter 304. The beam analyzer 306 can be, but is not limited to, a camera and/or wavefront detector, for example. The optical receiver 300 can further include a beam splitter 308, such as, but not limited to, a partially silvered mirror or a dichroic mirror to direct a portion of the received beam of light to the beam analyzer. The optical receiver 300 can be used in, but is not limited to, an optical communication system. The optical communication system can be a waveguide system and/or a free space system.

In free space communication systems according to some embodiments of the current invention, information can be encoded in the shape of the beam without loss of light, such as would occur with temporal modulation. The broad bandwidth can be advantageous for communications.

FIG. 1E is a schematic illustration of a solar furnace 400 according to an embodiment of the current invention. The solar furnace 400 includes a light collection system 402, an active optical beam shaper 404 arranged in an optical path of light collected by the light collection system 402, and an optical focusing system 406 arranged to receive a beam of light from the active optical beam shaper 404 to be focused on an object 408 to be heated. The active optical beam shaper 404 can be the same as, or similar to, active optical beam shaping system 100. The efficiency is boosted by shaping the solar beam precisely to the heat element with losing energy that can scatter and also cause damage.

The following examples describe some embodiments and some applications in more detail. However, the broad concepts of the current invention are not limited to the particular examples.

EXAMPLES

The examples here describe a family of practical applications according to some embodiments of the current inven-

tion. As their ultimate performances depend strongly on the pupil structure, we limit the scope here to a few characteristic examples. Full optimization for specific telescope geometries, as well as other applications, can be conducted as needed.

1 Introduction

Some embodiments of the current invention can take advantage of state-of-the-art Deformable Mirrors (DM) in modern high-contrast instruments to address the problem of pupil amplitude discontinuities for on-axis and/or segmented telescopes. Indeed, coronagraphs are not sufficient to reach the high contrast required to image faint exo-planets: wavefront control is needed to remove the light scattered by small imperfections on the optical surfaces (Brown & Burrows 1990). Over the past several years, significant progress has been made in this area, both in the development of new algorithms (Bordé & Traub 2006; Give'on et al. 2007) and in the experimental demonstration of high-contrast imaging with a variety of coronagraphs (Give'on et al. 2007; Trauger & Traub 2007; Guyon et al. 2010b; Belikov et al, 2011). These experiments rely on a system with a single Deformable Mirror which is controlled based on diagnostics downstream of the coronagraph, either at the science camera or as close as possible to the end detector (Wallace et al. 2009; Pueyo et al. 2010). Such configurations are well suited to correct phase wavefront errors arising from surface roughness but have limitations in the presence of pure amplitude errors (reflectivity), or phase-induced amplitude errors, which result from the propagation of surface errors in optics that are not conjugate to the telescope pupil (Shaklan & Green 2006; Pueyo & Kasdin 2007). Indeed a single DM can only mimic half of the spatial frequency content of amplitude errors and compensate for them only on one half of the image plane (thus limiting the scientific field of view) over a moderate bandwidth. In theory, architectures with two sequential Deformable Mirrors, can circumvent this problem and create a symmetric broadband high contrast PSF (Shaklan & Green 2006; Pueyo & Kasdin 2007). The first demonstration of symmetric dark hole was reported in Pueyo et al. (2009) and has since been generalized to broadband by Groff et al. (2011). In such experiments the coronagraph has been designed over a full circular aperture, the DM control strategy is based on a linearization of the relationship between surface deformations and electrical field at the science camera, and the modeling tools underlying the control loop consist of classic Fourier and Fresnel propagators. This is illustrated on the left panel of FIG. 1. As a consequence, a wavefront control system composed of two sequential Deformable Mirrors is currently the baseline architecture of currently envisioned coronagraphic space-based instruments (Shaklan et al. 2006; Krist et al. 2011) and ELT planet imagers (Macintosh et al. 2006). One can thus naturally be motivated to investigate if such wavefront control systems can be used to cancel the light diffracted by secondary supports and segments in large telescopes, since such structures are amplitude errors, albeit large amplitude errors.

The purpose of the current example is to demonstrate that indeed a two Deformable Mirror wavefront control system can mitigate the impact of the pupil asymmetries, such as spiders and segments, on contrast and thus enable high contrast on unfriendly apertures. We first present a new approach to coronagraph design according to an embodiment of the current invention in the presence of a central obscuration, but in the absence of spiders or segments. We show that for coronagraphs with a pupil apodization and an opaque focal plane stop, contrasts of 10^{-10} can be reached for any central obscuration diameter, provided that the Inner Working Angle is large enough. Naturally the secondary support structures,

and in the segmented cases, segment gaps, will degrade this contrast. As our goal is to use two DMs as an amplitude modulation device, we first briefly review the physics of such a modulation. We then introduce a solution to this problem. In particular, we show how to compute DM surfaces that mitigate spiders and segment gaps. Current algorithms used for amplitude control operate under the assumption that amplitude errors are small, and thus they cannot be readily applied to the problem of compensating aperture discontinuities, which have inherently large reflectivity non-uniformities. FIG. 1G illustrates how the current example embodiment introduces a control strategy for the DMs that is radically different from previously published amplitude modulators in the high-contrast imaging literature. Our technique, which we name Active Compensation of Aperture Discontinuities (hereafter ACAD), finds the adequate DM shapes in the true non-linear large amplitude error regime. In this case the DMs' surfaces are calculated as the solution of a non-linear partial differential equation, called the Monge-Ampere Equation. Below, we further describe our methodology according to an embodiment of the current invention to solve this equation and illustrate each step using an obscured and segmented geometry similar to JWST. As ACAD DM surfaces are prescribed in the ray-optics approximation, this is a fundamentally broadband technique provided that chromatic diffractive artifacts, edge ringing in particular, do not significantly impact the contrast. We find that when remapping small discontinuities with Deformable Mirrors, the spectral bandwidth is only limited by wavelength-dependent edge-diffraction ringing in the Fresnel approximation (as discussed in Pueyo & Kasdin (2007) for instance). Below, we also present the application of some embodiments of the current invention to various observatory architectures. Some embodiments of the current invention can render high contrast coronagraphy possible on any observatory geometry without adding any new hardware.

2 Coronagraphy with a Central Obscuration

2.1 Optimizing Pupil Apodization in the Presence of a Central Obscuration

Because the pupil obscuration in an on-axis telescope is large it will be very difficult to mitigate its impact with DMs with a limited stroke. Indeed, the main hindrance to high-contrast coronagraphy in on-axis telescope is the presence of the central obscuration: it often shadows much more than 10% of the aperture width while secondary supports and segments gaps cover ~1%. We thus first focus of azimuthally symmetric coronagraphic designs in the presence of a central obscuration. This problem (without the support structures) has been addressed in previous publications either using circularly symmetric pupil apodization (Soummer et al. 2011) or a series of phase masks (Mawet et al. 2011). Both solutions however are subject to limitations. The singularity at the center of the Optical Vector Vortex Coronagraph might be difficult to manufacture and a circular opaque spot thus lies in the central portion of the phase mask ($<\lambda/D$) which results in a degradation of the ideal contrast of such a coronagraph (Krist et al. 2011). The solutions in Soummer et al. (2011) result from an optimization seeking to maximize the off-axis throughput for a given focal plane stop diameter: the final contrast is absent from the optimization metric and is only a byproduct of the chosen geometry. Higher contrasts are then obtained by increasing the size of the focal plane mask, and thus result in a loss in IWA.

2.2 The Optimization Problem

Here we revisit the solution proposed by Soummer et~al. (2011) in a slightly different framework. We recognize that, in the presence of wavefront errors, high contrast can only be

achieved in an area of the field of view that is bounded by the spatial frequency corresponding to the DM's actuator spacing. We thus consider the design of an Apodized Pupil Lyot Coronagraph which only aims at generating high contrast between the Inner Working Angle (IWA) and Outer Working Angle (OWA). In order to do so, we rewrite coronagraphs described by Soummer et~al. (2003) as an operator $\mathcal{C}$ which relates the entrance pupil P(r) to the electrical field in the final image plane. We first call $\hat{P}(\xi)$ the Hankel transform of the entrance pupil:

$$\hat{P}(\xi)=\int_{D_S/2}^{D/2}P(r)J_0(r\xi)r\,dr \tag{1}$$

where D is the pupil diameter, D_S the diameter of the secondary and ξ the coordinate at the science detector expressed in units of angular resolution (λ_0/D). λ_0 is the design wavelength of the coronagraph chosen to translate the actual physical size of the focal plane mask in units of angular resolution (often at the center of the bandwidth of interest). λ is then the wavelength at which the coronagraph is operating (e.g. the physical size of the focal plane mask remains constant as the width of the diffraction pattern changes with wavelength). For the purpose of the monochromatic designs presented herein $\lambda=\lambda_0$. Then the operator is given by:

$$C[P(r)](\xi) = \hat{P}(\xi) - \frac{\lambda^2}{\lambda_0^2}\int_{D_S/2}^{D/2}\hat{P}(\eta)K(\xi,\eta)\eta\,d\eta \tag{2}$$

where $K(\xi,\eta)$ is the convolution kernel that captures the effect of the focal plane stop of diameter M_{stop}:

$$K(\xi,\eta)=\int_0^{M_{stop}/2}J_0(u\eta)J_0(u\xi)u\,du \tag{3}$$

An analytical closed form for this kernel can be calculated using Lommel functions. Note that this Eq. 2 assumes that the Lyot stop is not undersized. Since we are interested in high contrast regions that only span radially all the way up to a finite OWA, we seek pupil apodization of the form:

$$P(r) = \sum_{k=0}^{N_{modes}} p_k J_Q\left(\frac{r}{\alpha_k^Q}\right) \tag{4}$$

where $I_Q(r)$ denotes the Bessel function of the first kind of order Q and α_k^Q the kth zero of this Bessel function. In order to devise optimal apodizations over obscured pupils, Q, can be chosen to be large enough so that $I_Q(r)\ll1$ for $r<D_S/2$ (in practice we choose Q=10), The α_k^Q corresponds to the spatial scale of oscillations in the coronagraph entrance pupil, and such a basis set yields high contrast regions all the way to OWA$\simeq N_{modes}\lambda_0/D$. Since the operator in Eq. 2 is linear, finding the optimal P_k can be written as the following linear programming problem:

$$\max_{(p_k)}\left[\min_r(P(r))\right] \text{ Under the constraints} \tag{5}$$

$$|C[(P(r))](\xi)| < 10^{-\sqrt{C}} \text{ for } IWA < \xi < OWA \tag{6}$$

$$\max_r(P(r)) = 1 \tag{7}$$

$$\left|\frac{d}{dr}[P(r)]\right| < b. \tag{8}$$

Our choice of cost function and constraints has been directed by the following rationale:

We maximize the smallest value on the apodization function in an attempt to maximize throughput. The actual throughput is a quadratic function of the p_k. Maximizing it requires the solution of a non-linear optimization problem (as described in Vanderbei et~al. (2003).

The contrast constraint is enforced between the IWA and the OWA ($<N_{modes}$).

The maximum of the apodization function is set to one (otherwise the p_k will be chosen to be sufficiently small so that the contrast constraint is met).

The absolute value of the derivative across the pupil cannot be larger than a limit, denoted as b here. As the natural solutions of such problems are very oscillatory (or "bang bang", [Vanderbei et~al, (2003)], a smoothness constraint has to be enforced (see [Vanderbei et~al. (2007)] for a similar case).

Note that the linear transfer function in Eq. 2 can also be derived for other coronagraphs, with grayscale and phase image-plane masks, or for the case of under-sized Lyot stops. As general coronagraphic design in obscured circular geometries is not our main purpose, we limit the scope of the paper to coronagraphs represented by Eq. 2.

Optimal design Apodized Pupil Lyot Coronagraphs on circularly obscured apertures. With fixed obscuration ratio, size of opaque focal plane mask, IWA and OWA, our linear programming approach yields solutions with theoretical contrast below 10^{10}. All PSFs shown on this figure are monochromatic for $\lambda=\lambda_0$. When all other quantities remain equal and the central obscuration ratio increases (from 10% in the top panel to 20% in the middle panel), then the solution becomes more oscillatory (e.g less feasible) and the contrast constraint has to be relaxed. Eventually the optimizer does not find a solution and the size of the opaque focal plane mask (and thus the IWA) has to be increased (central obscuration of 30% in the bottom panel). On the right hand side, we present our results in two configurations: when the apodization is achieved using at grayscale screen (APLC), "on-sky" λ/D bottom x-axis, and when the apodization is achieved via two pupil remapping mirrors (PIAAC), "on-sky" λ/D top x-axis. We adopt this presentation to show that ACAD is "coronagraph independent" and that it can be applied to coronagraphs with high throughput and small IWA.

2.3 Results of the Optimization

Typical results of the monochromatic optimization in Eqs. 8, with $\lambda=\lambda_0$, are shown in FIG. 2.2 for central obscurations of 10, 20 and 30%. In the first two cases the size of the focal plane stop is equal to $3\lambda/D$, the IWA is $4\lambda/D$ and the OWA is $30\lambda/D$. As the size of the central obscuration increases the resulting optimal apodization becomes more oscillatory and the contrast constraint has to be loosened in order for the linear programming optimizer to converge to a smoother solution. Alternatively increasing the size of the focal plane stop yields smooth apodizers with high contrast, at a cost in angular resolution (bottom panel with a central obscuration of 30%, a focal plane mask of radius $4\lambda/D$, an IWA of $5\lambda/D$ and an OWA of $30\lambda/D$). These trade-offs were described in Soummer et~al. (2011), however our linear programming approach to the design of pupil apodizations now imposes the final contrast instead of having it be a by product of fixed central obscuration and focal plane stop. These apodizations can either be generated using grayscale screen (at a cost in throughput and angular resolution) or a series of two aspherical PIAA mirrors (for better throughput and angular resolution). In order not to lose generality, we present our results on FIG. 2.2 considering the two types of practical implementa-

tions (classical apodization and PIAA apodization). In the case of a grayscale amplitude screen the angular resolution units are as defined in Eq. 2 and the throughput is smaller than unity. In the case of PIAA apodisation the throughput is unity and the angular resolution units have been magnified by the field independent centroid based angular magnification defined in Pueyo et~al. (2011). We adopt this presentation for the remainder of the paper where one dimensional PSFs will be presented with "APLC angular resolution units" in the bottom horizontal axis and"PIAAC angular resolution units" in the top horizontal axis.

Note that this linear programming approach only optimizes the contrast for a given wavelength. However, since the solutions presented in FIG. **2.2** feature contrasts below 10^{10}, we choose not to focus on coronagraph chromatic optimizations. Instead, in order to account for the chromatic behavior of the coronagraph, the monochromatic simulations in §. 6 are carried out under the conservative assumption that the physical size of the focal plane stop is somewhat smaller than optimal (or that the operating wavelength of the coronagraph is slightly off, $\lambda = 1.2\lambda_0$). As a consequence the raw contrast of the coronagraphs presented in §. 6 is ~10^{-9}. Note that this choice is not representative of all possible Apodized Pupil Coronagraph chromatic configurations. It is merely a shortcut we use to cover the variety of cases presented in §. 6. In §. 7.2 we present a set of broadband simulations that include wavefront errors and the true coronagraphic chromaticity for a specific configuration and show that bandwidth is more likely to be limited by the spectral bandwidth of the wavefront control system than by the coronagraph. However, future studies aimed at defining the true contrast limits of a given telescope geometry will have to rely on solutions of the linear problem in Eqs. 8 which has been augmented to accommodate for broadband observations. In theory, the method presented here can also be applied to asymmetric pupils. However, the optimization quickly becomes computationally intensive as the dimensionality of the linear programming increases (in particular when the smoothness constraint and the bounds on the apodization have to be enforced at all points of a two dimensional array). This problem can be somewhat mitigated when seeking for binary apodizations, as shown in Carlotti et~al. (2011), at a cost in throughput and angular resolution.

3 Physics of Amplitude Modulation

3.1 General Equations

We have shown in §. 2 that by considering the design of pupil apodized coronagraphs in the presence of a circular central obscuration as a linear optimization problem, high contrast can be reached provided that the focal plane mask is large enough. In practice, the secondary support structures and the other asymmetric discontinuities in the telescope aperture (such as segment gaps) will prevent such levels of starlight suppression. We demonstrate that well controlled DMs can circumvent the obstacle of spiders and segment gaps. In this section, we first set-up our notations and review the physics of phase to amplitude modulation. We consider the system represented on FIG. **3** where two sequential DMs are located between the telescope aperture and the entrance pupil of the coronagraph. In this configuration, the telescope aperture and the pupil apodizer are not in conjugate planes. This will have an impact on the chromaticity of the system and is discussed in §. 5. Without loss of generality we work under the "folded" assumption illustrated on FIG. **3** where the DMs are not tilted with respect to the optical axis and can be considered as lenses of index of refraction −1 (as discussed in [Vanderbei Traub(2005)]. In the scalar approximation the relationship between the incoming field, $E_{DM1}(x,y)$, and the outgoing field, $E_{DM2}(x_2,y_2)$, is given by the diffractive Huygens Integral:

$$E_{DM2}(x_2, y_2) = \frac{1}{i\lambda Z} \int_{\mathcal{A}} E_{DM1}(x, y) e^{i\frac{2\pi}{\lambda}Q(x,y,x_2,y_2)} dx dy \qquad (9)$$

where $\mathcal{A}$ corresponds to the telescope aperture and $Q(x,y,x_2,y_2)$ stands for the optical path length between any two points at DM1 and DM2:

$$Q(x,y,x_2,y_2)=h_1(x,y)+S(x,y,x_2,y_2)-h_2(x_2,y_2) \qquad (10)$$

$S(x,y,x_2,y_2)$ is the free space propagation between the DMs:

$$\sqrt{(x - x_2)^2 + (y - y_2)^2 + (Z + h_1(x, y) - h_2(x_2, y_2))^2} \qquad (11)$$

where Z is the distance between the two DMs, h_1 and h_2 are the shapes of DM1 and DM2 respectively (as shown on FIG. 3) and λ is the wavelength. We recognize that two sequential DMs act as a pupil remapping unit similar to PIAA coronagraph [Guyon(2003)] whose ray optics equations were first derived by [Traub & Vanderbei (2003)]. We briefly state the notation used to describe such an optical system as introduced in Pueyo et~al. (2011):

For a given location at DM2, (x_2,y_2), the location at DM1 of the incident ray according to ray optics is given by:

$$x_1(x_2,y_2)=f_1(x_2,y_2) \qquad (12)$$

$$y_1(x_2,y_2)=g_1(x_2,y_2). \qquad (13)$$

Conversely, for a given location at DM1, (x_1,y_1), the location at DM2 of the outgoing ray according to geometric optics is given by:

$$x_2(x_1,y_1)=f_2(x_1,y_1) \qquad (14)$$

$$y_2(x_1,y_1)=g_2(x_1,y_1). \qquad (15)$$

Fermat's principle dictates the following relationships between the remapping functions and the shape of DM1:

$$\frac{\partial h_1}{\partial x}\Big|_{(x_1,y_1)} = \frac{x_1 - f_2(x_1, y_1)}{Z} \qquad (16)$$

$$\frac{\partial h_1}{\partial y}\Big|_{(x_1,y_1)} = \frac{y_1 - g_2(x_1, y_1)}{Z}. \qquad (17)$$

Conversely, if we choose the surface of DM2 to ensure that the outgoing on-axis wavefront is flat, we then find:

$$\frac{\partial h_2}{\partial x}\Big|_{(x_2,y_2)} = \frac{x_2 - f_1(x_2, y_2)}{Z} \qquad (18)$$

$$\frac{\partial h_2}{\partial y}\Big|_{(x_2,y_2)} = \frac{y_2 - g_1(x_2, y_2)}{Z}. \qquad (19)$$

Schematic of the optical system considered: the telescope apertures is followed by two sequential Defromable Mirrors (DMs) in non-conjugate planes whose purpose is to remap the pupil discontinuities. The beam then enters a coronagraph to suppress the bulk of the starlight: in this figure we show an Apodized Lyot Pupil Coronagraph (APLC). This is the coro-

nagraphic architecture we consider for the remainder of the paper but we stress that the method presented herein is applicable to any coronagraph.

3.2 Fresnel Approximation and Talbot Imaging

In Pueyo et~al. (2011) we showed that one could approximate the propagation integral in Eq. 9 by taking in a second order Taylor expansion of $Q(x,y,x_2,y_2)$ around the rays that trace $(f_1(x_2,y_2), g_1(x_2,y_2))$ to (x_2,y_2). In this case the relationship between the fields at DM1 and DM2 is:

$$E_{DM2}(x_2, y_2) = \tag{20}$$
$$\frac{e^{\frac{zi\pi}{\lambda}Z}}{i\lambda Z}\left\{\int_{\mathcal{A}} E_{DM1}(x, y)e^{\frac{i\pi}{\lambda Z}\left[\frac{\partial f_2}{\partial x}(x-x_1)^2 + 2\frac{\partial g_2}{\partial x}(x-x_1)(y-y_1) + \frac{\partial g_2}{\partial y}(y-y_1)^2\right]}\right.$$
$$\left. dx dy\right\}\Bigg|_{(x_1,y_1)}$$

When the mirror's deformations are very small compared to both the wavelength and D^2/Z, the net effect of the wavefront disturbance created by DM1 can be captured in E_{DM1} (x,y) and the surface of DM2 can be factored out of Eq. 9. In this case

$$x_1 = x_2, \; y_1 = y_2, \; \frac{\partial f_2}{\partial x}\bigg|_{x_1,y_1} = 1, \; \frac{\partial f_2}{\partial y}\bigg|_{x_1,y_1} = 0, \; \frac{\partial g_2}{\partial y}\bigg|_{x_1,y_1} = 1.$$

Then, Eq. 20 reduces to:

$$E_{DM2}(x_2, y_2) = \tag{21}$$
$$\frac{e^{\frac{zi\pi}{\lambda}(Z-h_2(x_2,y_2))}}{i\lambda Z}\int_{Aperture} e^{\frac{zi\pi}{\lambda}(h_1(x,y))}e^{\frac{i\pi}{\lambda Z}((x-x_2)^2+(y-y_2)^2)}dx dy$$

which is the Fresnel approximation. If moreover

$$h_1(x, y) = \lambda\varepsilon\cos\left(\frac{2\pi}{D}(mx + ny)\right),$$

$h_2(x,y)=-h_1(x,y)$, with $\epsilon \ll 1$, then the outgoing field is to first order:

$$E_{DM2}(x_2, y_2) \propto \frac{\pi\lambda Z(m^2 + n^2)}{D^2}\lambda\varepsilon\cos\left(\frac{2\pi}{D}(mx_2 + ny_2)\right). \tag{22}$$

$$E_{DM2}(x_2, y_2) = \frac{n\lambda Z(m^2 + n^2)}{p^2}\lambda\varepsilon\cos\left(\frac{2\pi}{p}(mx_2 + ny_2)\right)$$

This phase-to-amplitude coupling is a well known optical phenomenon called Talbot imaging and was introduced to the context of high contrast imaging by [Shaklan & Green (2006)]. In the small deformation regime, the phase on DM1 becomes an amplitude at DM2 according to the coupling in Eq. 22. When two sequential DMs are controlled to cancel small amplitude errors, as in Pueyo et~al. (2009), they operate in this regime. Note, however, that the coupling factor scales with wavelength (the resulting amplitude modulation is wavelength independent, but the coupling scales as λ): this formalism is thus not applicable to our case, for which we are seeking to correct large amplitude errors (secondary support

structures and segments) with the DMs. In practice, when using Eq. 22 in the wavefront control scheme outlined in Pueyo et~al. (2009) to correct aperture discontinuities, this weak coupling results in large mirror shapes that lie beyond the range of the linear assumption made by the DM control algorithm. For this reason, methods outlined on the left panel of FIG. 1G to correct for aperture discontinuities do not converge to high contrast. Because phase to amplitude conversion is fundamentally a very non-linear phenomena, these descending gradient methods [Bordà & Traub (2006), Give'on et~al. (2007) Pueyo et~al. (2009)] are not suitable to find DM shapes that mitigate apertures discontinuities. We circumvent these numerical limitations by calculating DMs shapes that are based on the full non-linear problem, right panel of FIG. 1G.

3.3 The SR-Fresnel Approximation

In the general case, starting from Eq. 20 and following the derivation described in §. 5, the field at DM2 can be written as follows:

$$E_{DM2}(x_2, y_2) = \left\{\sqrt{|\det[J]|}\right. \tag{23}$$
$$\left.\int_{\mathcal{FP}} \bar{E}_{DM1}(\xi, \eta)e^{i2\pi(\xi f_1 + \eta g_1)}e^{-i\frac{\pi\lambda Z}{\det[J]}\left(\frac{\partial g_1}{\partial y}\xi^2 + \frac{\partial f_1}{\partial x}\eta^2\right)}d\xi d\eta\right\}\Bigg|_{(x_2,y_2)}$$

where $\bar{E}_{DM1}(\xi,\eta)$ is the Fourier transform of the telescope aperture, $\mathcal{F}\,\mathcal{P}$ and stands for the Fourier plane. We call this integral the Stretched-Remapped Fresnel approximation (SR-Fresnel). Moreover $\det[J(x_2,y_2)]$ is the determinant of the Jacobian of the change of variables that maps (x_2,y_2) to (x_1,y_1):

$$\det[J(x_2, y_2)] = \left\{\frac{\partial f_1}{\partial x}\frac{\partial g_1}{\partial y} - \left(\frac{\partial g_1}{\partial x}\right)^2\right\}\Bigg|_{(x_2,y_2)}. \tag{24}$$

In the ray optics approximation, $\lambda\sim 0$, the non-linear transfer function between the two DMs becomes:

$$E_{DM2}(x_2,y_2)=\{\sqrt{|\det[J]|}E_{DM1}(f_1,g_1)\}|_{(x_2,y_2)} \tag{25}$$

$$[E_{DM2}(x_2,y_2)]^2=\{\det[J][E_{DM1}(f_1,g_1)]^2\}|_{(x_2,y_2)} \tag{26}$$

The square form (e.g Eq. 26) of this transfer function can also be derived based on conservation of energy principles and is a generalization to arbitrary geometries of the equation driving the design of PIAA coronagraphs [Vanderbei & Traub (2005)]. A full diffractive optimization of the DM surfaces requires use of the complete transfer function shown in Eq. 23. However, there do not exist yet tractable numerical method to evaluate Eq. 23 efficiently enough in order for this model to be included in an optimization algorithm. Moreover even solving the ray optics problem is extremely complicated: it requires to find the mapping function (f_1,g_1) which solves the non-linear partial differential equation in Eq. 26. Substituting for (f_1,g_1) and using Eqs. 19 yields a second order non-linear partial differential equation in h_2. This is the problem that we set ourselves to tackle in the next section, and is the cornerstone of our Adaptive Compensation of Aperture Discontinuities. As a check, one can verify that in the small deformation regime

$$\left(\text{e.g. if } h_1(x, y) = \lambda \varepsilon \cos\left(\frac{2\pi}{D}(mx + ny)\right) \text{ and } h_2(x, y) = -h_1(x, y)\right)$$

Eq. 26 yields the same phase-to-amplitude coupling as in Talbot imaging [Pueyo (2008)], Eq. 26 is a well know optimal transport problem [Monge (1781)], which has already been identified as underlying optical illumination optimizations [Glimm & Oliker (2002)]. While the existence and uniqueness of solutions in arbitrary dimensions have been extensively discussed in the mathematical literature (see [Dacorogna & Moser (1990)] for a review), there was no practical numerical solution published up until recently. In particular, to our knowledge, not even a dimensional solution for which the DM surfaces can be described using a realistic basis-set has been published yet. We now introduce a method that calculates solutions to Eq. 26 which can be represented by feasible DM shapes.

4 Calculation of the Deformable Mirror Shapes

4.1 Statement of the Problem

Ideally, we seek DM shapes that fully cancel all the discontinuities at the surface of the primary mirror and yield a uniform amplitude distribution, as shown in the top panel of FIG. 2. A solutions for a particular geometry with four secondary support has been derived by Lozi et~al. (2009). It relies on reducing the dimensionality of the problem to the direction orthogonal to the spiders. It is implemented using a transmissive correcting plate that is a four-faced prism arranged such that the vertices coincides with the location of the spiders. The curvature discontinuities at the location of the spiders are responsible for the local remapping that removes the spiders in the coronagraph pupil. However such a solution cannot be readily generalized to the case of more complex apertures, where the secondary support structures might vary in width, or in the presence of segment gaps. Moreover it is transmissive and thus highly chromatic. Here we focus on a different class of solutions and seek to answer a different question. How well can we mitigate the effect of pupil discontinuities using DMs with smooth surfaces, a limited number of actuators (e.g a limited maximal curvature), and a limited stroke? Under these constraints directly solving Eq. 26 (e.g. solving the forward problem illustrated in the top panel of FIG. 2) is not tractable as both factors on the left hand side of Eq. 26 depend on h_2. More specifically, the implicit dependence of E_{DM1} $(f_1(x_2,y_2), g_1(x_2,y_2))$ on h_2 can only be addressed using finite elements solvers, whose solutions might not be realistically representable using a DM. However this can be circumvented using the reversibility of light and solving the reverse problem, where the two mirrors have been swapped. Indeed, since

$$x_2 = f_2(f_1(x_2,y_2), g_1(x_2,y_2)) \tag{27}$$

$$y_2 = g_2(f_1(x_2,y_2), g_1(x_2,y_2)) \tag{28}$$

then we have the following relationship between the determinants of the forward and reverse remappings:

$$1 = \left\{\frac{\partial f_2}{\partial x}\frac{\partial g_2}{\partial y} - \left(\frac{\partial g_2}{\partial x}\right)^2\right\}\Big|_{(x_1,y_1)} \left\{\frac{\partial f_1}{\partial x}\frac{\partial g_1}{\partial y}\left(\frac{\partial g_1}{\partial x}\right)^2\right\}\Big|_{(x_2,y_2)} \tag{29}$$

We thus focus on the inverse problem, bottom panel of FIG. 2, that consists of first finding the surface of h_1 as the solution of:

$$\left\{[E_{DM2}(f_2, g_2)]^2\left[\frac{\partial f_2}{\partial x}\frac{\partial g_2}{\partial y} - \left(\frac{\partial g_2}{\partial x}\right)^2\right]\right\}\Big|_{(x_1,y_1)} = [E_{DM1}(x_1, y_1)]^2 \tag{30}$$

Since our goal is to obtain a pupil as uniform a possible we seek a field at DM2 as uniform as possible:

$$E_{DM2}(f_2(x_1,y_1), g_2(x_1,y_1)) = \frac{1}{\sqrt{\int_{a4}E_{DM1}(x,y)^2 dx dy}} = \text{Constant.} \tag{31}$$

Moreover we are only interested in compensating asymmetric structures located between the secondary and the edge of the primary. We thus only seek to find (f_2, g_2) such that:

$$E_{DM1}(x_1, y_1) = \tag{32}$$

$$A(x_1, y_1) = \left([P(x, y) - (1 - P_o(x, y))] * e^{-\frac{x^2+y^2}{\omega^2}}\right)\Big|_{(x_1,y_1)}$$

where $P_0(x_1,y_1)$ is the obscured pupil, without segments or secondary supports. Finally, we focus on solutions with a high contrast only up to a finite OWA. We artificially taper the discontinuities by convolving the control term in the Monge-Ampere Equation, $[P(x,y)-(1-P_0(x,y))]$, with a gaussian of width ω, Note that this tapering is only applied when calculating the DM shapes via solving the reverse problem. When the resulting solutions are propagated through Eq. 26 we use the true telescope pupil for $E_{DM1}(x_1,y_1)$. The parameter ω has a significant impact on the final post-coronagraphic contrast. Indeed we are here working with a merit function that is based on a pupil-plane residual, while ideally our cost function should be based on image-plane intensity. By convolving the control term in the reverse Monge-Ampere Equation, we low pass filter the discontinuities. This is equivalent to giving a stronger weight to low-to-mid spatial frequencies of interest in the context of exo-planets imaging. For each case presented in §. 6 we calculate our DM shapes over a grid of values of ω which correspond to low pass filters with cutoff frequencies ranging from ~OWA to ~2 OWA and we keep the shapes which yield the best contrast. This somewhat ad-hoc approach can certainly be optimized for higher contrasts. However such an optimization is beyond the scope of the present manuscript.

The problem we are seeking to solve is illustrated in the second panel of FIG. 2. In this configuration the full second order Monge-Ampere Equation can be written as:

$$\left(1 + Z\frac{\partial^2 h_1}{\partial x^2}\right)\left(1 + Z\frac{\partial^2 h_1}{\partial y^2}\right) - \left(Z\frac{\partial^2 h_1}{\partial x \partial y}\right)^2 = A(x, y)^2 \tag{33}$$

where we have dropped the (x_1,y_1) dependence for clarity. Since we are interested in surface deformations which can realistically be created using a DM, we seek for a Fourier representation of the DMs surface:

$$h_1(x, y) = \frac{D^2}{Z}H_1(X, Y) \tag{34}$$

$$= \frac{D^2}{Z}\sum_{n=-N/2}^{N/2}\sum_{m=-N/2}^{N/2} a_{m,n}e^{i\frac{2\pi}{D}(mX+nX)}$$

with

$$a_{-m,-n} = a^*_{-m,-n}, \ a_{-m,-n} = a^{\frac{1}{2}}_{-m,-n},$$

where N is the limited number of actuators across the DM. Note that we have normalized the dimensions in the pupil plane X=x/D, Y=y/D. The normalized second order Monge-Ampere Equation is then:

$$\left(1 + \frac{\partial^2 H_1}{\partial X^2}\right)\left(1 + \frac{\partial^2 H_1}{\partial Y^2}\right) - \left(\frac{\partial^2 H_1}{\partial X \partial Y}\right)^2 = A(X, Y)^2 \quad (35)$$

For each configuration in this paper we first solve Eq. 35 and then transform the normalized solution in physical units, which depends on the DMs diameter D and their separation Z.

4.2 Solving the Monge-Ampere Equation to Find H_1

Over the past few years a number of numerical algorithms aimed at solving Eq. 35 have emerged in the literature [Loeper & Rapetti (2005), Benamou et~al. (2010)]. Here we summarize our implementation of two of them: an explicit Newton method [Loeper &Rapetti (2005)], and a semi-implicit method [Froese & Oberman (2012)]. We do not delve into the proof of convergence of each method, they can be found in Loeper & Rapetti (2005), Benamou et~al. (2010) Froese & Oberman (2012)]. Note that Zheligovsky et~al. (2010) discussed both approaches in a cosmological context and devised Fourier based solutions. Here we are interested in a two dimensional problem and we outline below the essence of each algorithm.

4.2.1 Explicit Newton Algorithm

This method was first introduced by [Loeper & Rapetti (2005)] and relies on the fact that Eq. 35 can be re-written as

$$\det\left[\left(\begin{matrix} 1 + \frac{\partial^2 H_1}{\partial X^2} & \frac{\partial^2 H_1}{\partial X \partial Y} \\ \frac{\partial^2 H_1}{\partial X \partial Y} & 1 + \frac{\partial^2 H_1}{\partial Y^2} \end{matrix}\right)\right] = \det[Id + \mathcal{H}(H_1(X, Y))] \quad (36)$$

where $\mathcal{H}(.)$ is the two dimensional Hessian of a scalar field and Id the identity matrix. If one writes H_1=u+v with $\|v\|<<\|u\|$ then:

$$det[Id + \mathcal{H}(u+\delta v)] = det[Id + H(u)] + \delta Tr[(Id + H(u))^{\dagger T} H(v)] + o(\delta^2) \quad (37)$$

where $(.)^{\dagger T}$ denotes the transpose of the comatrix. Eq. 35 can thus be linearized as:

$$\left(1 + \frac{\partial^2 u}{\partial Y^2}\right)\frac{\partial^2 v}{\partial X^2} + \left(1 + \frac{\partial^2 u}{\partial X^2}\right)\frac{\partial^2 v}{\partial Y^2} - 2\frac{\partial^2 u}{\partial X \partial Y}\frac{\partial^2 v}{\partial X \partial Y} = \quad (38)$$
$$\left(A(X, Y)^2 - \det\left[\mathcal{H}\left(\frac{X^2 + Y^2}{2} + u\right)\right]\right)$$

The explicit Newton algorithm relies on Eq. 38 and can then be summarized as carrying out the following iterations:

Choose a first guess H_1^0.

At each iteration k we seek for a solution of the form $H_1^{k+1} = H_1^k + V^k$, where V^k is the DM shape update.

In order to find V^k we write:

$$L_E(H_1^k, V^k) = \quad (39)$$
$$\left(1 + \frac{\partial^2 H_1^k}{\partial Y^2}\right)\frac{\partial^2 V^k}{\partial X^2} + \left(1 + \frac{\partial^2 H_1^k}{\partial X^2}\right)\frac{\partial^2 V^k}{\partial Y^2} - 2\frac{\partial^2 H_1^k}{\partial X \partial Y}\frac{\partial^2 V^k}{\partial X \partial Y}$$

$$R_E(H_1^k) = \frac{1}{r}(A^2 - \det[Id + \mathcal{H}(H_1^k)]) \quad (40)$$

and solve

$$L_E(H_1^k, V^k) = R_E(H_1^k). \quad (41)$$

Eq. 41 is a linear partial differential equation in V^k. Since we are interested in a solution which can be expanded in a Fourier series we write V^k as:

$$V_1^k(X, Y) = \sum_{n=-N/2}^{N/2} \sum_{m=-N/2}^{N/2} v_{m,n}^k e^{i\frac{2\pi}{D}(mX + nX)}. \quad (42)$$

Both the right hand side and the left hand side of Eq. 45 can be written as a Fourier series, with a spatial frequency content between –N and N cycles per aperture. Equating each Fourier coefficient in these two series yields the following linear system of $(2N+1)^2$ equations with $(N+1)^2$ unknowns.

For all $m_0, n_0 \in [-N, N]$: $\int_{DM} e^{i2\pi(m_0 X + n_0 Y)}[L_E(H_1^k, V^k) - R_E(H_1^k)]dX\,dY = 0 \quad (43)$

When searching for V^k as a Fourier series over the square geometry chosen here, this inverse problem is always well posed.

Update the solution $H_1^{k+1} = H_1^k + V_1^{k+1}$

The convergence of this algorithm relies on the introduction of a damping constant $\tau > 1$. [Loeper & Rapetti (2005)] showed that as long as

$$\frac{X^2 + Y^2}{2} + H_1^k$$

remains convex, which is always true for ACAD with reasonably small aperture discontinuities, there exists a τ large enough so that this algorithm converge towards a solution of Eq. 35. However since this algorithm is gradient based, it is not guaranteed that it converges to the global minimum of the underlying non-linear problem. In order to avoid having this solver stall in a local minimum we follow the methodology outlined by [Froese & Oberman (2012)] and first carry out a series of implicit iterations to get within a reasonable neighborhood of the global minimum.

Virtual field at M1 when solving the reverse problem. A (X_1, Y_1) is the desired apodization (top), $A''(X_1, Y_1)$ is the apodization obtained after solving the Monge-Ampere Equation (center). The bottom panel shows the difference between the two quantities: the bulk of the energy in the residual is located in high spatial frequencies that cannot be controlled by the DMs.

4.2.2 Implicit Algorithm

This algorithm, along with its convergence proof, is thoroughly explained in [Froese Oberman (2012)]. It relies on rewriting Eq. 35 as:

$$\frac{\partial^2 H_1}{\partial X^2} + \frac{\partial^2 H_1}{\partial Y^2} = \sqrt{\det[Id + \mathcal{H}(H_1(X, Y))]^2 + 2A(X, Y)^2} \qquad (44)$$

The implicit method consists of carrying out the following iterations:

Choose a first guess H_1^0

In order to find H^{k+1} we write:

$$L_I(H_1^k, V^k) = \frac{\partial^2 H_1^{k+1}}{\partial X^2} + \frac{\partial^2 H_1^{k+1}}{\partial Y^2}$$

$$R_E(H_1^k) = \sqrt{\det[Id + \mathcal{H}(H_1(X, Y))]^2 + 2A(X, Y)^2}$$

and solve

$$L_1(H_1^{k+1}) = R_1(H_1^k). \qquad (45)$$

This problem is a linear system of $(N+1)^2$ equations with $(N+1)^2$ unknowns and can be solved using projections on a Fourier Basis:

For all $m_0, n_0 \in [-N,N]$: $\int_{DM} e^{i2\pi(m_0X+n_0Y)} [L_1(H_1^k, V^k) - R_1 (H_1^k)] dX\, dY = 0$ \qquad (46)

Note that the term under the square root in $R_1(H_1^k)$ is guaranteed to be positive at each iteration.

Iterate over k

The inverse problem in Eq. 46 is always well posed, for any basis set or pupil geometry, while the explicit Newton method runs into convergence issues when not using a Fourier basis over a square. When seeking to use a basis set that is more adapted to the geometry of the spiders and segments or when using a trial influence function basis for the DM, the implicit method is the most promising method. In this paper we have limited our scope to solving the reverse problem in the bottom panel of FIG. **4**, and used a Fourier representation for the DM, we are able to use both methods. In order to make sure that the algorithm converges towards the true solution of Eq. 35 we first run a few tens of iterations of the implicit method and, once it has converged, we seek for a more accurate solutions using the Newton algorithm. Typical results are shown in FIG. **6** where most of the residual error resides in the high spatial frequency content (e.g. above N cycles per aperture). Our solutions are limited by the non-optimality of the Fourier basis to describe the mostly radial and azimuthal structures present in telescopes' apertures. Moreover the DM shape is the result of the minimization of a least squares residual in the virtual end-plane of the reverse problem, with little regard to the spatial frequency content of the solution in the final image plane of the coronagraph. While this method yields significant contrast improvements, as reported in §. 6, we discuss in §. 7 how it can be refined for higher contrast.

4.3 Deformation of the Second Mirror

Once the surface of DM1 has been calculated as a solution of Eq. 26, we compute the surface of DM2 based on Eqs. 19, which stem from enforcing flatness of the outgoing on-axis wavefront. We seek a Fourier representation for the surface of DM2:

$$h_2(x, y) = \frac{D^2}{Z} H_2(X, Y) = \frac{D^2}{Z} \sum_{n=-N/2}^{N/2} \sum_{m=-N/2}^{N/2} b_{m,n} e^{i\frac{2\pi}{D}(mX+nX)} \qquad (47)$$

Plugging the solution found in the previous step for h_1 into Eqs. 17 yields a closed form for the normalized remapping functions, (F_2, G_2):

$$F_2(X_1, Y_1) = X_1 - \sum_{n=-N/2}^{N/2} \sum_{m=-N/2}^{N/2} i2\pi m\, a_{m,n} e^{i2\pi(mX_1+nY_1)}$$

$$G_2(X_1, Y_1) = Y_1 - \sum_{n=-N/2}^{N/2} \sum_{m=-N/2}^{N/2} i2\pi n\, a_{m,n} e^{i2\pi(mX_1+nY_1)}$$

Then the normalized version of Eqs. 19 can be rewritten as:

$$L_x(X_1, Y_1) = \sum_{m=-N/2}^{N/2} i2\pi m\, b_{m,n} e^{i2\pi(mF_2(X_1,Y_1)+nF_2(X_1,Y_1))}$$

$$R_x(X_1, Y_1) = X_1 - F_2(X_1, Y_1)$$

$$L_x = R_x \qquad (48)$$

$$L_y(X_1, Y_1) = \sum_{m=-N/2}^{N/2} i2\pi n\, b_{m,n} e^{i2\pi(mF_2(X_1,Y_1)+nF_2(X_1,Y_1))}$$

$$R_y(X_1, Y_1) = Y_1 - G_2(X_1, Y_1)$$

$$L_y = R_y \qquad (49)$$

We then multiply each side of Eq. 48 and Eq. 49 by:

$$e^{i2\pi(m_0F_2(X_1,Y_1)+n_0F_2(X_1,Y_1))} \det[Id + \mathcal{H}(H_1^k(X_1,Y_1))]$$

where (m_0, n_0) corresponds to a given DM spatial frequency. Integrating over the square area of the DM and using the orthogonality of the Fourier basis yields the following system of $2*(N+1)^2$ equations with $(N+1)^2$ real unknowns:

For all (m_0, n_0):

$$2\pi i\, m_0 b_{m_0, n_0} =$$
$$\int_{DM} R_x(X, Y) \det[Id + \mathcal{H}(H_1^k(X, Y))] e^{i2\pi(m_0F_2(X,Y)+n_0F_2(X,Y))} dX\, dY$$

For all (m_0, n_0):

$$i2\pi i\, n_0 b_{m_0, n_0} =$$
$$\int_{DM} R_x(X, Y) \det[Id + \mathcal{H}(H_1^k(X, Y))] e^{i2\pi(m_0F_2(X,Y)+n_0F_2(X,Y))} dX\, dY$$

$$2\pi i n_0 b_{m_0, n_0} =$$
$$\int_{DM} R_y(X, Y) \det[Id + \mathcal{H}(H_1^k(X, Y))] e^{i2\pi(m_0F_2(X,Y)+n_0F_2(X,Y))} dX\, dY$$

We then find H_2, the normalized surface of DM2, by solving this system in the least squares sense. Once the Monge-Ampere Equation has been solved, the calculation of the surface of the second mirror is a much easier problem. Indeed, by virtue of the conservation of the on-axis optical path length, finding the surface of DM2 only consists of solving a linear system (see [Traub & Vanderbei (2003)]).

4.4 Boundary Conditions

The method described above does not enforce any boundary conditions associated with Eq. 35. One practical set of boundary conditions consists of forcing the edges of each DM to map to each other:

$$F_i\left(\pm\frac{1}{2}, Y\right) = \pm\frac{1}{2} \qquad (50)$$

$$F_i\left(X, \pm\frac{1}{2}\right) = X \qquad (51)$$

$$G_i\left(\pm\frac{1}{2}, Y\right) = Y \qquad (52)$$

-continued

$$G_i\left(X, \pm\frac{1}{2}\right) = \pm\frac{1}{2} \qquad (53)$$

with i=1,2. These correspond to a set of Neumann boundary conditions in $H_1(X,Y)$ and $H_2(X,Y)$. These boundary conditions can be enforced by augmenting the dimensionality of the linear systems on Eq. 43 and Eq. 46, however doing so increases the residual least squares errors and thus hampers the contrast of the final solution. Moreover FIG. **4** and FIG. **5** show that, because of the one to one remapping near the DM edges in the control term of the reverse problem, the boundary conditions are almost met in practice. For the remainder of this paper we thus do not include boundary conditions when calculating the DM shapes, when solving for $H_1(X,Y)$ in Eq. 35 since, in the worse case, only the edge rows and columns of the DMs actuator will have to be sacrificed in order for the edges to truly map to each other.

4.5 Remapped Aperture

For a given pupil geometry we have calculated (H_1,H_2). We then convert the DM surfaces to real units, (h_1,h_2), by multiplication with D^2/Z. We evaluate the remapping functions using Eqs. 17 and 19 and obtain the field at the entrance of the coronagraph in the ray optic approximation

$$E_{DM2}(x_2, y_2) = \qquad (54)$$

$$\left\{ \sqrt{\det[J]}\, E_{DM1}(f_1, g_1) e^{i\frac{2\pi}{\lambda}(S(f_1,g_1)+h_1(f_1,g_1)-h_2)} \right\}\Big|_{(x_2,y_2)}$$

where the exponential factor corresponds to the Optical Path Length through the two DMs. Even if the surface of the DMs has been calculated using only a finite set of Fourier modes, we check that the optical path length is conserved.

FIG. **6** shows that since the curvature of the DMs is limited by the number of modes N, our solution does not fully map out the discontinuities induced by the secondary supports and the segments. However, they are significantly thinner and one can expect that their impact on contrast will be attenuated by orders of magnitude. In order to quantify the final coronagraphic contrasts of our solution we then propagate it through an APLC coronagraph designed using the method in §. 2. In the case of a hexagon based primary (such as JWST), we use a coronographic apodizer with a slightly oversized secondary obscuration and undersize outer edge in order to circularize the pupil. Note that this choice is mainly driven by the type of coronagraph we chose in §. 2 to illustrate our technique. Since the DM control strategy presented in this section is independent of the coronagraph, it can be generalized to any of the starlight suppression systems which have been discussed in the literature. For succinctness we present our results using coronagraph solely based on using pupil apodization (either in an APLC or in a PIAAC configuration). Results for a JWST geometry are shown on FIG. **5.3** and FIG. **7** and discussed in §. 6. Eq. 54 assumes that the propagation between the two DMs occurs according to the laws of ray optics. In the next section we derive the actual diffractive field at DM2, e.g Eq. 23, and show that in the pupil remapping regime of ACAD, edge ringing due to the free space propagation is actually smaller than in the Fresnel regime.

5 Chromatic Properties

5.1 Analytical Expression of the Diffracted Field

ACAD is based on ray optics. It is an inherently broadband technique, and provided that the coronagraph is optimized for broadband performance ACAD will provide high contrast over large spectral windows. However, when taking into account the edge diffraction effects that are captured by the quadratic integral in Eq. 23, the true propagated field at DM2 becomes wavelength dependent. More specifically, when λ is not zero then the oscillatory integral superposes on the ray optics field a series of high spatial frequency oscillations. In theory, it would be best to use this as the full transfer function to include chromatic effects in the computation of the DMs shapes. However, as discussed in §. 4, solving the non-linear Monge-Ampere Equation is already a delicate exercise, and we thus have limited the scope of this paper to ray optics solutions. Nonetheless, once the DMs' shapes have been determined using ray optics, one should check whether or not the oscillations due to edge diffraction will hamper the contrast. This approach is reminiscent of the design of PIAA systems where the mirror shapes are calculated first using geometric optics and are then propagated through the diffractive integral in order to check a posteriori whether or not the chromatic diffractive artifacts are below the design contrast [Pluzhnik et~al. (2005)]. In this section we detail the derivation of Eq. 23 that is the diffractive integral for the two DMs remapping system and use this formulation to discuss the diffractive properties of ACAD.

We start with the expression of the second order diffractive field at DM2 as derived in [Pueyo et~al. (2011)], Eq. 20.

$$E_{DM2}(x_2, y_2) =$$

$$\frac{1}{i\lambda Z}\left\{ \int E_{DM1}(x, y) e^{\frac{i\pi}{\lambda Z}\left[\frac{\partial f_2}{\partial x}(x-x_1)^2+2\frac{\partial g_2}{\partial x}(x-x_1)(y-y_1)+\frac{\partial g_2}{\partial y}(y-y_1)^2\right]} \right.$$

$$\left. dxdy \right\}\Big|_{(x_1,y_1)}$$

We write $E_{DM1}(x,y)$ as its inverse Fourier transform

$$E_{DM1}(x,y)=\int \hat{E}_{DM1}(\xi,\eta) e^{i2\pi(x\xi+y\eta)} d\xi d\eta \qquad (55)$$

and insert this expression in Eq. 20. Completing the squares in the quadratic exponential factor then yields:

$$E_{DM2}(x_2, y_2) = \frac{1}{i\lambda Z}\left\{ \int \hat{E}_{DM1}(\xi, \eta) I_1(f_1, g_1) e^{i2\pi[f_1\xi+g_1\eta]} \right. \qquad (56)$$

$$\left. e^{-i\pi\lambda Z\left(\frac{\partial f_2}{\partial y}\big|_{(f_1,g_1)}\xi^2+\frac{\partial g_2}{\partial x}\big|_{(f_1,g_1)}\eta^2\right)} d\xi d\eta \right\}\Big|_{(x_2,y_2)}$$

with

$$I_1(y_1, x_1) = \qquad (57)$$

$$\left\{ \int e^{\frac{i\pi}{\lambda}\left[\frac{\partial f_2}{\partial x}\left(x-x_1-\frac{\xi\lambda Z}{\frac{\partial f_2}{\partial x}}\right)^2+2\frac{\partial g_2}{\partial x}(x-x_1)(y-y_1)+\frac{\partial g_2}{\partial y}\left(y-y_1-\frac{\eta\lambda Z}{\frac{\partial g_2}{\partial x}}\right)^2\right]} dx \right.$$

$$\left. dy \right\}\Big|_{(x_1,y_1)} \quad .$$

The integral over space, $I_1(y_1,x_1)$, is the integral of a complex gaussian and can be evaluated analytically. This yields:

$$E_{DM2}(x_2, y_2) = \left\{ \frac{1}{\sqrt{\left| \frac{\partial f_2 \partial g_2}{\partial x \partial y} - \left(\frac{\partial g_2}{\partial x} \right)^2 \right|}} \right. \tag{58}$$

$$\left. \int \hat{E}_{DM1}(\xi, \eta) e^{i2\pi[x_1 \xi + y_1 \eta]} e^{-i\pi\lambda Z \left(\frac{\partial f_2}{\partial y} \xi^2 + \frac{\partial g_2}{\partial x} \eta^2 \right)} d\xi d\eta \right\} \Bigg|_{(x_1, y_1)}.$$

We thus have expressed $E_{DM2}(x_2, y_2)$ as a function of $(x_1, y_1) = (f_1(x_2, y_2), g_1(x_2, y_2))$. This expression can be further simplified: using Eqs. 27 to 29 one can derive

$$\frac{\partial f_2}{\partial x} \Bigg|_{(x_1, y_1)} = \frac{1}{\det[J(x_2, y_2)]} \frac{\partial g_1}{\partial y} \Bigg|_{(x_2, y_2)}$$

and

$$\frac{\partial g_2}{\partial y} \Bigg|_{(x_1, y_1)} = \frac{1}{\det[J(x_2, y_2)]} \frac{\partial f_1}{\partial x} \Bigg|_{(x_2, y_2)}.$$

Which finishes to prove Eq. 23:

$$E_{DM2}(x_2, y_2) = \tag{59}$$

$$\left\{ \sqrt{|\det[J]|} \int_{\mathcal{FP}} \hat{E}_{DM1}(\xi, \eta) e^{i2\pi(\xi f_1 + \eta g_1)} e^{-i\frac{\pi\lambda Z}{\det|J|} \left(\frac{\partial g_1}{\partial y} \xi^2 + \frac{\partial f_1}{\partial x} \eta^2 \right)} \right.$$

$$\left. d\xi d\eta \right\} \Bigg|_{(x_2, y_2)}$$

This expression is very similar to a modified Fresnel propagation and can be rewritten as such:

$$E_{DM2}(x_2, y_2) = \tag{60}$$

$$\left\{ \int_{\mathcal{A}} E_{DM1}(x, y) e^{-i\frac{\pi\det[J]}{\lambda Z} \left(\left(\frac{\partial g_1}{\partial y} \right)^{-1} (x - f_1)^2 + \left(\frac{\partial f_1}{\partial x} \right)^{-2} (y - g_1)^2 \right)} dx \right.$$

$$\left. dy \right\} \Bigg|_{(x_2, y_2)}$$

$$E_{DM2}(x_2, y_2) = \left\{ \int_{\mathcal{A}} E_{DM1}(x, y) e^{-i\frac{\pi\det[J]}{\lambda Z} \left(\left(\frac{\partial g_1}{\partial y} \right)^{-1} (x - f_1)^2 + \left(\frac{\partial f_1}{\partial x} \right)^{-1} (y - g_1)^2 \right)} \right.$$

$$\left. dx dy \right\} \Bigg|_{(x_2, y_2)}$$

Because of this similarity we call this integral the Stretched-Remapped Fresnel approximation (SR-Fresnel). Indeed in this approximation the propagation distance is stretched by

$$\left(\frac{\frac{\partial g_1}{\partial y}}{\det[J]}, \frac{\frac{\partial f_1}{\partial x}}{\det[J]} \right)$$

and the integral is centered around the remapped pupil (f_1, g_1).

5.2 Discussion

FIG. **10**, Left: Comparison of edge diffraction between PIAA and Fresnel propagation. Because the discontinuities in

the pupil occur at the location where $\Gamma_x < 1$, a PIAA amplifies the chromatic ringing when compared to a more classical propagation. Right: Comparison of edge diffraction between ACAD and Fresnel propagation. Because the discontinuities in the pupil occur at the location where $\Gamma_x > 1$, a ACAD damps the chromatic ringing when compared to a more classical propagation. These simulations were carried out for a one dimensional aperture. In this case the Monge-Ampere Equation can be solved using finite elements and the calculation of the diffractive effects reduces to the evaluation of various Fresnel special functions at varying wavelength. The full two-dimensional problem is not separable and requires the development of novel numerical tools.

The integral form provides physical insight about the behavior of the chromatic edge oscillations. If we write

$$\Gamma_x = \frac{\det[J]}{\frac{\partial g_1}{\partial y}} \Bigg|_{(x_2, y_2)} \tag{61}$$

$$\Gamma_y = \frac{\det[J]}{\frac{\partial f_1}{\partial x}} \Bigg|_{(x_2, y_2)} \tag{62}$$

we can identify a several diffractive regimes:

1. when $\Gamma_x = \Gamma_y = 1$ the $E_{DM2}(x, y_2)$ reduces to a simple Fresnel propagation. Edge ringing can them be mitigated using classical techniques such as pre-apodization, or re-imaging into a conjugate plane using oversized relay optics.

2. when $\Gamma_x, \Gamma_y < 1$ then it is as if the effective propagation length through the remapping unit was increased. This magnifies the edge chromatic ringing.

3. when $\Gamma_x, \Gamma_y > 1$ then it is as if the effective propagation length through the remapping unit was decreased. This damps the edge chromatic ringing.

4. when $\Gamma_x > 1$ and $\Gamma_y < 1$, e.g. at a saddle point in the DM surface, then it is as if the effective propagation length through the remapping unit was decreased in one direction and increased in the other. The edge chromatic ringing can either be damped or magnified depending on the relative magnitude of Γ_x and Γ_y.

In the case of a PIAA coronagraphs, the mirror shapes are such that $\Gamma_x, \Gamma_y > 1$ at the center of the pupil and $\Gamma_x, \Gamma_y \ll 1$ at the edges of the pupil, where the discontinuities occur. As a consequence the edge oscillations are largely magnified when compared to Fresnel oscillations (see right panel of FIG. **10**), and apodizing screens are necessary in order to reduce the local curvature of the mirror's shape (as also discussed in [Pluzhnik et~al. (2005), Pueyo et~al, (2011)]. In the case of ACAD, where the x-axis is chosen to be perpendicular to the discontinuity, the surface curvature is such that $\Gamma_x > 1$, $\Gamma_y \sim 1$ at the discontinuities inside the pupil and $\Gamma_x > 1$, $\Gamma_y \sim 1$ elsewhere. This yields damped chromatic oscillations at the remapped discontinuities and Fresnel oscillations at the edges of the pupil (see right panel of FIG. **10**). Note that FIG. **10** was generated using a one dimensional toy model that assumes Eq. 23 is separable, e.g $\Gamma_y = 1$, as described in [Pueyo et~al. (2011)]. In practice at the saddle points of the optical surfaces, near the junction of two spiders for instance, $\gamma_x > 1$, $\Theta_y < \sim 1$ and thus our separable model does not guarantee than in the true 2D case chromatic edge oscillations might not be locally amplified. However even near the saddle points ACAD provides a strongly converging remapping in the direction perpendicular to the discontinuity and very little diverging remapping in the other direction. As a consequence $\Gamma_x \gg 1$

and Γ_y is smaller than but close to one. We thus predict that even at these locations chromatic ringing will not be amplified. Even though ACAD is based on pupil remapping, its diffraction properties are qualitatively very different from PIAA coronagraphs since edge ringing is not amplified beyond the Fresnel regime at the pupil edges, and is attenuated near the discontinuities. We conclude that in most cases ACAD operates in a regime where edge chromatic oscillations are not larger than classical Fresnel oscillations, and sometimes actually smaller. As a consequence the chromaticity of this ringing can be mitigated using standard techniques developed in the Fresnel regime, and we do not expect this phenomenon to be a major obstacle to ACAD broadband operations.

5.3 Diffraction Artifacts in ACAD are no Worse than Fresnel Ringing

Results obtained when applying our approach to a geometry similar to JWST. We used two 3 cm DMs of 64 actuators separated by 1 m. Their maximal surface deformation is 1.1 μm, well within the stroke limit of current DM technologies. The residual light in the corrected PSF follows the secondary support structures and can potentially be further cancelled by controlling the DMs using an image plane based cost function, see FIG. 23

We have established that the diffractive chromatic oscillations introduced by the fact that DM1 and DM2 are not located in conjugate planes is no worse than classical Fresnel ringing from the aperture edges and can be mitigated using well-know techniques which have been developed for this regime. While a quantitive tradeoff study of how to design a high contrast instrument which minimizes such oscillations is beyond the scope of this paper, we briefly remind their qualitative essence to the reader:

The edges of the discontinuities in the telescope aperture can be smoothed via pupil apodization before DM1. This solution is not particularly appealing as it requires the introduction of a transmissive, and thus dispersive, component in the optical train.

The distance between the two DMs can be reduced. Indeed the DMs deformations presented herein, for 3 cm DMs separated by 1 m, are all ≤ 1 μm while current technologies allow for deformations of several microns. As the edge ringing scales as Z/D^2 chromatic oscillations will be reduced by decreasing Z. Since the DM surfaces scale as D^2/Z reducing Z will increase the DM deformations but have little impact on the feasibility of our solution as current DM technologies can reach 4 μm strokes.

The coronagrahic apodizer can be placed in a plane that is conjugate to the DM1. This can be achieved by re-imaging DM2 through a system of oversized optics (the over-sizing factor increases steeply when the pupil diameter decreases). By definition there are no Fresnel edge oscillations in such a plane. Alternatively a coronagraph without a pupil apodization (amplitude or phase mask in the image plane) can be used, and in this configuration it is only sufficient for the optics to be oversized.

Note that these three solutions are not mutually exclusive and that only a full diffractive analysis, which uses robust numerical propagators that have been developed based on Eq. 23, can quantitatively address the trade-offs discussed above. The development of such propagators is our next priority. In [Pueyo et~al. (2011)] we laid out the theoretical foundations of such a numerical tool in the case of circularly symmetric pupil remapping and this solution has been since then practically implemented, as reported by [Krist et~al, (2010)]. Generalizing this method to a tractable propagator in the case

of arbitrary remapping is a yet unsolved computational problem. In the meantime we emphasize that while the spectral bandwidth of coronagraphs whose incoming amplitude has been corrected using ACAD will certainly be limited by edge diffraction effects, but these effects are no worse than Fresnel ringing and can thus be mitigated using optical designs which are now routinely used in high contrast instruments (see [Vàinaud et~al. (2010)] for such discussions). For the remainder of this paper we thus assume the diffractive artifacts have been adequately mitigated and we compute our results assuming a geometric propagation between DM1 and DM2.

When using two sequential DMs as a pure amplitude actuator (e.g., assuming a flat wavefront after the second DM) the relationship between the surface deformations and the outgoing electrical field is given by the Huygens integral. We derived, under the second order approximation for the Huygens integrand, a simplified expression of this diffractive transfer function:

$$E_{DMs} = \left\{ \frac{1}{\sqrt{\left|\frac{\partial f_2}{\partial x}\frac{\partial g_2}{\partial y} - \left(\frac{\partial g_2}{\partial x}\right)^2\right|}} \int \hat{E}_{DM1}(\xi, \eta) e^{i2\pi[x_1\xi + y_1\eta]} e^{-i\pi\lambda Z\left[\frac{\partial f_2}{\partial y}\xi^2 + \frac{\partial g_2}{\partial x}\eta^2\right]} d\xi d\eta \right\}\Bigg|_{(x_2, y_2)}$$

The computational cost associated with the diffractive transfer function in the above equation and also Eq. (59) makes it almost impossible to devise a global inversion method that captures both the remapping of large amplitude errors and the diffractive properties of the dual DMs unit.

Procedure to Include Diffraction

As a consequence in order to find DM shapes that efficiently compensate for the secondary support structures, we provide the procedure outlined below:

1. First invert the problem in the ray optics approximation in order to map out the pupil imprint of the spiders as much as possible, as discussed in this specification.

2. Second compute in the SR-approximation the diffractive response associated with the derived DM shapes using Eq. (59). Assess the broadband properties of the dual DM unit in the presence of diffractive effects.

3. Using a small perturbation superposed to the deformations calculated in step 1, compute, around the equilibrium point set by step 1, the sensitivity matrix for both DMs seen through the chosen coronagraph. This matrix is calculated using the diffractive models in step 2, e.g. in the SR-approximations. We conduct an iterative closed loop.

Results for the Astronomical Telescope Application

As an illustration we have applied the entire methodology described above to a geometry analogous to the AFTA telescopes. We have in particular successfully implemented a numerical integrator capable of capturing the diffractive effects in Eq. (59) that are the sources of the bandwidth limit in ACAD. Our results are shown on FIG. 26 where we calculated, assuming that the DMs have been controlled according to step 1, the field in a plane conjugate with the telescope pupil. When introducing a Focal Plane Mask, this plane would be the Lyot plane of the coronagraph and its wavefront topology drives the contrast floor and bandwidth when using linear DM control loops. From a ray optics perspective ACAD "fills up as much as possible" the area obscured by the secondary support structure FIG. 3, while in the diffractive

regime we can see that ACAD replaces the deep and sharp amplitude errors from supports with shallow and smooth ripples. The chromatic nature of these oscillations sets the ultimate bandwidth of ACAD. We see that ACAD only weakly impacts the bandwidth of the starlight suppression system, as shown in FIG. 27 where we have combined these diffractive models with a Radial Apodization Vector Vortex Coronagraph (RA-VVC, Mawet et al., in prep., and obtained contrasts as deep at 3×10 at $2\lambda/D$ over the full range of wavelengths from 500 nm to 700 nm, a bandwidth of over 30%. The combination of FIG. 23 (APLC or PIAAC) and FIG. 27 illustrates the second advantage of ACAD: it is fundamentally "coronagraph agnostic". We have conducted diffractive simulations using the RA-VVC since it is one of the most promising technologies for obscured apertures 70% throughput in its high transmissivity configuration and theoretical IWA as close as 1.5 λ/D. Smaller IWA solutions should they be available later on.

6 Results

6.1 Application to Future Observatories

6.1.1 JWST

We have illustrated each step of the calculation of the DM shapes in §. 4 using a geometry similar of JWST. This configuration is somewhat a conservative illustration of an on-axis segmented telescope as it features thick secondary supports and a "small" number of segments whose gaps diffract light in regions of the image plane close to the optical axis (the first diffraction order of a six hexagons structure is located at ~$3\lambda/D$). In order to assess the performances of ACAD on such an observatory architecture we chose to use a coronagraph designed around a slightly oversized secondary obscuration of diameter 0.25 D, with a focal plane mask of diameter $3\lambda/D$, an IWA of $5\lambda/D$ and an OWA of $30\lambda/D$. The field at the entrance of the coronagraph after remapping by the DMs is shown on the top right panel of FIG. 11. The DM surfaces, calculated assuming 64 actuators across the pupil (N=64 in the Fourier expansion) and DMs of diameter 3 cm separated by Z=1 m, are shown on the middle panel of FIG. 11. They are well within the stroke limit of current DM technologies. The surfaces were calculated by solving the reverse problem over an even grid of 10 cutoff low-pass spatial frequencies ranging between 30 and 70 cycles per apertures for the tapering kernel ω. The value yielding the best contrast was chosen. Note that the optimal cutoff frequency depends on the spatial scale of the discontinuities, and that higher contrasts could be obtained by choosing a set of two convolution kernels for the reverse problem and finding the optimal solution using a finer grid. However, the results in the bottom row of FIG. 11 are extremely promising. FIG. 12 shows a contrast improvement of a factor of 100 when compared to the raw coronagraphic PSF, which is quite remarkable for an algorithm which is not based on an image-plane metric. These results illustrate that even with a very unfriendly aperture similar to JWST one can obtain contrasts as high as envisioned for upcoming Ex-AO instruments, which have been designed for much friendlier apertures. While we certainly do not advocate to use such a technique on JWST, this demonstrates that ACAD is a powerful tool for coronagraphy with on-axis segmented apertures.

6.1.2 Extremely Large Telescopes

PSFs resulting from ACAD when varying the number and thickness of secondary support structures while maintaining their covered surface constant (FIG. 15). The surface area covered in this example is 5096 greater than in the TMT example shown on FIG. 13. As the spiders get thinner their impact on raw contrast becomes smaller and the starlight suppression after DM correction becomes bigger. For a rela-

tively small number of spiders (<12) the contrast improvement on each single structure is the dominant phenomenon, regardless of the number of spiders. ELTs designed with a moderate to large number of thin secondary support structure (6 to 12) present aperture discontinuities which are easy to correct with ACAD.

We now discuss the case of Extremely Large Telescopes and provide an illustration using the example of the Thirty Meter Telescope. We considered the aperture geometry shown on the top left panel of FIG. 13. It consists of a pupil 37 segments across in the longest direction and a secondary of diameter ~0.12D which is held by three main thick struts and six thin cables. As seen on the bottom left panel of FIG. 13 the impact of segment gaps is minor as they diffract light beyond the OWA of the coronagraph. When using a coronagraph with a larger OWA the segment gaps will have to be taken into account, and will have to be mitigated using DMs with a larger number of actuators. In order to obtain first order estimates of the performances of ACAD on the aperture geometry shown on the top left panel of FIG. 13, we chose to use a coronagraph designed around a slightly oversized secondary obscuration of diameter 0.15 D, with a focal plane mask of $6\lambda/D$ diameter, an IWA of $4\lambda/D$ and an OWA of $30\lambda/D$. The field at the entrance of the coronagraph after remapping by the DMs is shown on the top right panel of FIG. 13. The DM surfaces, calculated assuming 64 actuators across the pupil (N=64 in the Fourier expansion) and DMs of diameter 3 cm separated by Z=1 m, are shown on the middle panel of FIG. 13. They are well within the stroke limit of current DM technologies. The surfaces were calculated by solving the reverse problem over an even grid of 10 cutoff low-pass spatial frequencies ranging between 30 and 70 cycles per apertures for the tapering kernel ω. The value yielding the best contrast was chosen. The final PSF is shown on the bottom right panel of FIG. 13 and features a high contrast dark hole with residual diffracted light at the location of the spiders' diffraction structures. The impact on coronagraphic contrast of secondary supports was thoroughly studied by [Martinez et~al. (2008)]. They concluded that under a 90% Strehl ratio, the contrast in most types of coronagraphs is driven by the secondary support structures to levels ranging from 10^{-4} to 10^{-5}. This, in turn, leads to a final contrast after post-processing (called Differential Imaging) of ~10^{-7}-10^{-8}. FIG. 14 shows that using ACAD on an ELT pupil yields contrasts before any post-processing which are comparable to the ones obtained by [Martinez et~al. (2008)] after Differential Imaging. This demonstrates that should two sequential DMs be integrated into a future planet finding instrument, setting their surface deformation according to the methodology presenting above would allow this instrument to perform its scientific program at a very high contrast. Moreover the surface of the DMs could be adjusted to mitigate for the effect of missing segments at the surface of the primary (when for instance the telescope is operating while some segments are being serviced).

6.2 Hypothetical Cases

6.2.1 Constant Area Covered by the Secondary Support Structures

In the case of ELTs with large number of small segments (when compared to the aperture size), gaps diffract light far from the optical axis (see FIG. 13 for an example). The secondary support structures are then the major source of unfriendly coronagraphic diffracted light. Under the assumption that thick structures are necessary to support the heavy secondary over the very large ELT pupils, one can use the aperture area covered by the spiders as a proxy of the secondary lift constraint. We have thus explored a series of geom-

etries for which the number of spiders increases as they get thinner while the overall area covered by the secondary support structures remains constant. In the examples shown from FIG. **15** to FIG. **18**, the area covered by the secondary support structures is 1.5 times greater than in the TMT geometry discussed above. In all cases we used a coronagraph with a central obscuration of 0.15 D, with a focal plane mask of 6λ/D diameter, and IWA of 4λ/D and an OWA of 30λ/D. The surfaces were calculated by solving the reverse problem over an even grid of 10 cutoff low-pass spatial frequencies ranging between 30 and 70 cycles per apertures for the tapering kernel. The value yielding the best contrast was chosen. This exercise leads to several conclusions pertaining to the performances of ACAD with various potential ELT geometries.

Clocking of the Spiders with Respect to the DM

The top two panels of FIG. **15** illustrate the importance of the clocking of the spiders with respect to the DMs actuator grid (or the Fourier grid in our case). When the secondary support structures are clocked by 45° with respect to the DM actuators they are much more attenuated by ACAD, thus yielding higher contrast. This is an artifact of the Fourier basis set chosen and would be mitigated by using DMs whose actuator placement presents circular and azimuthal symmetries [Watanabe et~al. (2008)].

Annulus in the PSF with a Large Number of Spiders

When the number of secondary support struts becomes very large (>20), an interesting phenomena occurs in the raw PSF: the spiders diffract light outside an annulus of radius $N_{Spiders}/\pi\lambda/D$, just as spiderweb masks do in the case of shaped pupil coronagraphs [Vanderbei et~al. (2003)]. The "bump" located beyond that spatial frequency is more difficult to attenuate using the DMs (see FIG. **15** for an illustration). ACAD creates small ripples at the edges of the remapped discontinuities and when too many discontinuities are in the vicinity of each other, then these ripples interfere constructively and hamper the starlight extinction level yielded by ACAD.

A Lot of Thin Spiders is More Favorable Than a Few Thick Spiders

In general decreasing the width of the spiders while increasing their number is beneficial to the contrast obtained after ACAD as illustrated on the radial averages on FIG. **16** and FIG. **18**. When one increases the number of spiders while decreasing their width in a classical coronagraph, the peak intensity of the diffraction pattern of one spider decreases as the squared width of the spider. The radially averaged contrast improvement without ACAD is then somewhat lesser than the square of the spider thinning factor as it is mitigated by the increasing number of spiders. When using ACAD the spiders are seen by the coronagraph as much thinner than they actually are (by a factor τ) and thus the peak intensity of their diffraction pattern is lower by a factor of τ^2, Our numerical experiments show that τ increases when the spider width decreases. As consequence, the overall contrast gain after ACAD when decreasing the width of the spiders while increasing their number is greater than in the case of a classical coronagraph. When designing ELT secondary support structures and planning to correct for them using ACAD, increasing the number of spiders to 8 or even 12 has a beneficial impact on contrast as it enables each discontinuity to become thinner and thus to be corrected to higher contrast using the DMs. The PSFs of apertures with more than 12 spiders present diffraction structures which are poorly suited for correction with square DMs. While the contrast resulting from applying ACAD to such apertures is still a decreasing function of the number of spiders, FIG. **18** shows that the net contrast gain brought by the DM based remapping is smaller

than in the more gentle cases of 12 spiders. The study presented on FIG. **15** to FIG. **18** remains to be fully optimized for each potential design of an ELT planet finding instrument (in particular using a finer grid of cutoff spatial frequencies). It however demonstrates the flexibility of ACAD for various aperture geometries and provides a first order rule of thumb to design telescope apertures which are friendly to direct imaging of exo-planets: "A lot of thin spiders is more favorable than a few thick spiders". In practice the number of spiders will be limited by effects not treated in our analysis such as the mechanical rigidity, requirements on the perfection of their periodic spacing and glancing reflections from the sides of multiple spiders. We thus advocate that, should future ELTs be built with high contrast exo-planetary science as a main scientific driver, then such effect ought to be thoroughly analyzed as a large numbers of thin spiders is more favorable from a contrast standpoint when using ACAD to mitigate for pupil amplitude asymmetries.

6.2.2 Monolithic on-Axis Apertures.

PSFs resulting from ACAD when varying the number and thickness of secondary support structures. As the spiders get thinner their impact on raw contrast becomes lesser and the starlight suppression after DM correction becomes greater. In this case ω was optimized on a very fine grid and the aperture we clocked in a favorable direction with respect to the Fourier basis.

When discussing the case of JWST we stressed the complexity associated with the optimization of ACAD in the presence of aperture discontinuities of varying width. Carrying out such an exercise would be extremely valuable to study the feasibility of the direct imaging of exo-earths with an on-axis segmented future flagship observatory such as ATLAST [Postman et~al. (2010)]. However, such an effort is computationally heavy and thus beyond the scope of the present paper, which focuses on introducing the ACAD methodology and illustrating using key basic examples.

So far, none of the examples in this manuscript demonstrate that ACAD can yield corrections all the way down to the theoretical contrast floor that is set by the coronagraph design. When seeking to image exo-earths from space, future missions will need to reach this limit. In order to explore this regime, we conducted a detailed study of a hypothetical on-axis monolithic telescope with four secondary support struts. To establish the true contrast limits we varied the thickness of the spiders for each geometry. The surfaces were calculated by solving the reverse problem over an even grid of 70 cutoff low-pass spatial frequencies ranging between 30 and 70 cycles per apertures for the tapering kernel. The value yielding the best contrast was chosen. In all cases we used a coronagraph with a central obscuration of 0.15 D, with a focal plane mask of 6λ/D diameter, and IWA of 4λ/D, and an OWA of 30λ/D. Note that when using coronagraphs relying on pupil apodization these results can be readily generalized to larger circular secondary obscurations, at a loss in IWA (as shown on FIG. **2**). Moreover we clocked the telescope aperture by 45° with respect to the grid of Fourier modes. We found that, indeed, the theoretical contrast floor set by the coronagraph design is met for thin spiders (0.02 D) and it is very close to being met for spiders only half the thickness of the ones currently equipping the Hubble Space Telecope (0.05 D), see FIG. **19** and FIG. **20**. Even in the case of thick struts (0.1 D) we find contrasts an order of magnitude higher than in the similar configuration on the top panel of FIG. **10**, due to our thorough optimization of the cutoff frequency of the tapering kernel and careful clocking of the aperture with respect to the actuators. On-axis telescopes are thus a viable option to image earth-analogs from space: their secondary

support structures can be corrected down to contrast levels comparable to the target contrast of recent missions concept studies [Guyon et~al. (2008), Trauger et~al. (2010)]. Since the baseline wavefront control architecture for future space coronagraphs relies on two sequential DMs, ACAD does not add any extra complexity to such missions and merely consists of controlling the DMs in order to optimally compensate for the effects of asymmetric aperture discontinuities.

7 Discussion

7.1 Field Dependent Distortion

Because ACAD relies on deforming the DMs' surfaces in an aspherical fashion, off-axis wavefronts seen through the two DMs apparatus will be distorted, just as in a PIAA coronagraph [Martinache et~al. (2006)]. However the asphericity of the surfaces in the case of ACAD operating on reasonably thin discontinuities, is much smaller than in a PIAA remapping unit. FIG. **21** shows the impact on off-axis PSFs of such a distortion in the worse-case scenario of a geometry similar to JWST. We demonstrate that most of the flux remains in the central disk of radius λ/D for all sources in the field of view of the coronagraphs considered here (all the way to 30 cycles per capture). We conclude that, because of the small deformations of the DMs, PSF distortion will not be a major hindrance in exo-planet imaging instruments whose DMs are controlled in order to mitigate for discontinuities in the aperture.

7.2 Impact of Wavefront Discontinuities in Segmented Telescopes.

7.2.1 General Equations in the Presence of Incident Phase Errors and Discontinuities

So far we have treated primary mirrors' segmentation as a pure amplitude effect. In reality the contrast floor in segmented telescopes will be driven by both phase and amplitude discontinuities; here we explore the impact of phase errors

and discontinuities occurring before two DMs whose surfaces have been set using ACAD. There are two main phenomena to be considered. The first is the conversion of the incident wavefront phase before

$$DM1: \frac{2\pi}{\lambda}\Delta h_1$$

into amplitude at the second mirror. The second is the projection of this wavefront phase into a remapped phase errors at

$$DM2: \frac{2\pi}{\lambda}\Delta h_1(f_1(x_1, y_2), g_1(x_1, y_2)).$$

Since the remapping unit is designed using deformable mirrors, both DM1 and DM2 a complete correction could be attained in principle. However, the deformable mirrors are continuous while Δh_1 presented discontinuities. Thus, complete corrections for segmented mirrors might not be achieved in practice. Below we discuss the following two main points. (1) Even if the phase wavefront error Δh_1 has discontinuities, the phase errors within in segment still drive the phase to amplitude conversion and thus the propagated

amplitude at DM2. In that case treatments of these phenomenons that have already been discussed in the literature for monolithic apertures are still valid for small enough phase errors and smooth enough remapping functions. For ACAD remapping this smoothness constraint is naturally enforced by the limited number of actuators across the DM surface. In this case phase to amplitude conversioncan in principle be corrected using DM1. (2) Remapped phase discontinuities can be corrected for a finite number of spatial frequencies using a continuous phase sheet deformable mirror. We illustrate this partial correction over a 20% bandwidth using numerical simulations of a post-ACAD half dark hole created by superposing a small perturbation, computed using a linear wavefront control algorithm, to the ACAD DM2 surface.

If the incoming wavefront is written as Δh_1 and the solution of the Monge-Ampere Equation for DM1 as h_1^0 then one can conduct the analysis in Eq. 9 to 19 using $\hat{h}_1 = h_1^0 + \Delta h_1$. Under the assumption that surface of DM2 is set as $\hat{h}_2$ in order to conserve Optical Path Length then one can re-write the remapping as $(\tilde{f}_1, \tilde{g}_1)$ defined by:

$$\frac{\partial \hat{h}_1}{\partial x}\bigg|_{(\tilde{f}_1(x_2,y_2),\tilde{g}_1(x_2,y_2))} = \frac{\tilde{f}_1(x_2, y_2) - x_2}{Z} \tag{63}$$

$$\frac{\partial \hat{h}_1}{\partial y}\bigg|_{(\tilde{f}_1(x_2,y_2),\tilde{g}_1(x_2,y_2))} = \frac{\tilde{g}_1(x_2, y_2) - y_2}{Z}$$

Moreover if edge ringing has been properly mitigated then the ray optics solution is valid and the field at DM2 can be written as:

$$E_{DM2}(x_2, y_2) = \left\{ \left(\frac{E_{DM1}}{\left(1 + \frac{\partial^2 \tilde{h}_1}{\partial x^2}\right)\left(1 + \frac{\partial^2 \tilde{h}_1}{\partial y^2}\right) - \left(\frac{\partial^2 \tilde{h}_1}{\partial x \partial x}\right)^2}\right)\bigg|_{(\tilde{f}_1,\tilde{g}_1)} e^{i\frac{2\pi}{\lambda}\left(S(\tilde{f}_1, \tilde{g}_1) + \tilde{h}_1(\tilde{f}_1, \tilde{g}_1) - \tilde{h}_2\right)} \right\}\bigg|_{(x_2,y_2)} \tag{64}$$

7.2.2 Impact on the Amplitude after ACAD

Broadband wavefront correction (20% bandwidth around 700 nm) with a single DM in segmented telescope with discontinuous surface errors. Top Left: wavefront before the coronagraph. Top Right: broadband aberrated PSF with DM at rest. Bottom Left: DM surface resulting from the wavefront control algorithm. Bottom Right: broadband corrected PSF. Note that the wavefront control algorithm seeks to compensate for the diffractive artifacts associated with the secondary support structures: it attenuates them on the right side of the PSF while it strengthens them on the left side of the PSF. As a result the DM surface becomes too large at the pupil spider's location and the quasi-linear wavefront control algorithm eventually diverges.

We first consider the amplitude profile in Eq. 64. it is composed of two factors: the remapped telescope aperture, $E_{DM1}(\tilde{f}_1, \tilde{g}_1)$, and the determinant of $Id + \mathcal{H}[\tilde{h}_1]$.

The first condition necessary for the incoming wavefront not to perturb the ACAD solution is: Δh_1 is such that the remapping is not modified at the pupil locations where the telescope aperture is not zero $E_{DM1} \neq 0$. This results in the following conditions:

$$\frac{\partial \Delta h_1}{\partial x} << \frac{\partial \Delta h_1^0}{\partial x} \text{ for } (x, y) \text{ such that } E_{DM1}(x, y) \neq 0$$

$$\frac{\partial \Delta h_1}{\partial y} << \frac{\partial \Delta h_1^0}{\partial y} \text{ for } (x, y) \text{ such that } E_{DM1}(x, y) \neq 0$$

At the locations where $E_{DM1}=0$ there is no light illuminating the discontinuous wavefront and thus the large local slopes at these location have no impact on the remapping functions (f_1, g_1). These conditions are not true in segmented telescopes that are not properly phased, for which the tip-tilt error over each segment can reach several waves. However under the assumption that the primary has been properly phased (for instance the residual rms wavefront after phasing is expected to be ~$\frac{1}{10}$ th of a wave, similar to values expected for JWST NIRCAM) then these conditions are true within the boundaries of each segment. Moreover, while the local wavefront slopes at the segment's discontinuities do not respect this condition the incident amplitude at these points is E_{DM1} (X, y)=0 and they thus do not perturb the ACAD remapping solution.

The second necessary condition resides in the fact that the determinant of $Id + \mathcal{H}$ ($\tilde{h}_1$) is not equal to $\det[Id + \mathcal{H}$ (h_1^0)] at the pupil locations where the telescope aperture is not zero ought not have a severe impact on contrast. One can use the linearization in [Loeper Rapetti (2005)] to show that:

$$\frac{1}{\det\left[Id + \mathcal{H}(\tilde{h}_1)\right]} = \tag{65}$$

$$\frac{1}{\det\left[Id + \mathcal{H}(\tilde{h}_1^0)\right]\left(1 + \dfrac{(1 + h_{1xx}^0)\Delta h_{1yy} + (1 + h_{1yy}^0)\Delta h_{1xx} - 2*h_{1xy}^0 \Delta h_{1xy}}{\det[Id + \mathcal{H}(h_1^0)]}\right)}$$

$$\frac{1}{\det\left[Id + \mathcal{H}(\tilde{h}_1)\right]} = \frac{1}{\det[Id + \mathcal{H}(h_1^0)](1 + \Delta A(\Delta h_1))} \tag{66}$$

The perturbation term $\Delta A(\Delta h_1)$ corresponds to the full non-linear expression of the phase to amplitude conversion of wavefront errors that occurs in pupil remapping units. In [Pueyo et~al. (2011)] we derived a similar expression in the linear case, when $\Delta h_1 << \lambda$ and showed that in the pupil regions where the beam is converging this phase to amplitude conversion was enhanced when compared to the case of a Fresnel propagation. In a recent study [Krist et~al. (2011)] presented simulations predicting that this effect was quite severe in PIAA coronagraphs and can limit the broadband contrast after wavefront control unless DMs were placed before the remapping unit. In principle ACAD will not suffer from this limitation as the first aspherical surface of the remapping unit is actually a Deformable Mirror that can actually compensate for Δh_1, before any phase to amplitude wavefront modulation occurs. Devising a wavefront controller that relies on DM1 requires moreover a computationally efficient model to propagate arbitrary wavefronts through ACAD. Such a tool was developed in [Krist et~al. (2010)] assuming azimuthally symmetric geometries. Since devising such a tool in ACAD's case, in the asymmetric case, represents a substantial effort well beyond the problem of prescribing ACAD DM shapes, we chose not to include such simulations in the present manuscript. Since we are using Deformable Mirrors with a limited number of actuators, ACAD remapping is in general less severe than in the case of

PIAA. We thus expect the results regarding the wavefront correction before the remapping unit reported in [Krist et~al. (2011)] to hold. This is provided that the DM actuators can adequately capture the high spatial frequency content of Δh_1 to create a dark hole in the coronagraphic PSF. We tackle this particular aspect next when discussing the case of phase errors, in the absence of wavefront phase to amplitude conversion. Once again note that while the local wavefront curvatures are very large at the segment's discontinuities, the incident amplitude at these points is $E_{DM1}(x,y)=0$ and thus they do not have an impact on the ACAD phase to amplitude modulation. In practice if the DM is not exactly located at a location conjugate to the telescope pupil the actual wavefront discontinuities will be slightly illuminated and might perturb the remapping functions and the phase to amplitude conversion. While this might tighten requirements regarding the positioning of DM1 in the direction of the optical axis we do not expect this effect to be a major obstacle to successful ACAD implementations.

7.2.3 Impact on the Phase after ACAD

In practice, when Δh_1 presents discontinuities, the surface of DM2 cannot be set to the deformation $\tilde{h}_2$ that conserves Optical Path Length, since we work under the assumption that the DM has a continuous phase-sheet. While this has no impact on the discussion above regarding the amplitude of E_{DM2}, since DM1 is solely responsible for this part, it ought to be taken into account when discussing the phase at DM2. Under the assumption that Δh_1 does not perturb the nominal ACAD remapping function then one can show that the phase at DM2 is:

$$\arg[E_{DM2}(x_2, y_2)] == \frac{2\pi}{\lambda}(\Delta h_1(f_1^0(x_2, y_2), g_1^0(x_2, y_2)) + \Delta h_2(x_2, y_2)) \tag{67}$$

where $\Delta h_2(x_2, y_2)$ is a small continuous surface deformation superposed to the ACAD shape of DM2 and $\Delta h_1(f_1^0(x_2, y_2), g_1^0(x_2, y_2))$ is the telescope OPD seen through the DM based remapping unit. This second term presents phase discontinuities whose spatial scale has been contracted by ACAD. When these discontinuities are very small then their high spatial frequency content does not disrupt the ability of DM2 to correct for low to mid-spatial frequency wavefront errors. However as the discontinuities become larger their high spatial frequency content can fold into the region of the PSF that the DMs seek to cancel. These "frequency folding" speckles are highly chromatic [Give'on et~al. (2006)] and can have a severe impact on the spectral bandwidth of a coronagraph whose wavefront is corrected using a continuous DM.

In order to assess the impact of this phenomenon, we conducted a series of simulations based on single DM wavefront control algorithm that seeks to create a dark hole in one half of the image plane at in as in [Borda & Traub (2006)]. We use the example of a geometry similar to JWST and work under the assumption that the discontinuous wavefront incident to the coronagraph has the same spatial frequency content as a JWST NIRCAM Optical Path Difference that has been adjusted to 70 nm rms in order to mimic a visible Strehl similar to the near-infrared Strehl of JWST. The non-linear wavefront and sensing and control problem associated with phasing a primary mirror to such level of precision is undoubtedly a colossal endeavor and is well beyond the scope of this paper. In this section we work under the assumption that the primary mirror either has been phased to such a level, that the wavefront discontinuities are no larger than 200 nm

peak to valley or that the wavefront has been otherwise corrected down to this specification using a segmented Deformable Mirror that is conjugate with the primary mirror. Moreover we assume (1) that the residual post-phasing wavefront map has been characterized and can be used in order to build the linear model underlying the wavefront controller (2) the focal plane wavefront estimator (carried using DM diversity as in [Borda. & Traub (2006)] for instance) is capable to yield an exact estimate of the complex electrical field at the science camera. Underlying this last assumption is the overly optimistic premise that wavefront will remain unchanged over the course of each high-contrast exposure. While this is not a realistic assumption one could envision the introduction of specific wavefront sensing schemes, with architectures similar to the one currently considered for low order wavefront sensors on monolithic apertures [Guyon et~al. (2009), Wallace et~al. (2011)], or using a separate metrology system. The results presented here are thus limited to configurations for which segment phasing will be dynamically compensated using specific sensing and control beyond the scope of this paper. As this section merely seeks to address the controllability of wavefront errors in segmented telescopes we chose to conduct our simulations with a perfect estimator. Finally we use the stroke minimization wavefront control algorithm presented in [Pueyo et~al. (2009)] to ensure convergence for as many iteration as possible. We first tested the case of a segmented telescope in the absence of ACAD, using a azimuthally symmetric coronagraph and a single DM. We sough to create a Dark Hole between 5 and 28 λ_0/D under a 20% bandwidth with λ_0=700 nm. FIG. **22** shows the results of such a simulation. The DM can indeed correct for the discontinuities over a broadband in one half of the image plane. However the wavefront control algorithm seeks to compensate for the diffractive artifacts associated with the secondary support structures: it attenuates them on the right side of the PSF while it strengthens them on the left side of the PSF. As a result the DM surface becomes too large at the pupil spider's location and the quasi-linear wavefront control algorithm eventually diverges for contrasts ~10^6.

Broadband wavefront correction (20% bandwidth around 700 nm) in a segmented telescope whose pupil has been re-arranged using ACAD. The surface of the first DM is set according to the ACAD equations. The surface of the second DM is the sum of the ACAD solution and a small perturbation calculated using a quasi-linear wavefront control algorithm. Top Left: wavefront before the coronagraph. Note that the ACAD remapping has compressed the wavefront errors near the struts and the segment gaps. Top Right: broadband aberrated PSF with DMs set to the ACAD solution. Bottom Left: perturbation of DM2's surface resulting from the wavefront control algorithm. Bottom Right: broadband corrected PSF. The wavefront control algorithm now yields a DM surface that does not feature prominent deformations at the location of the spiders. Most of the DM stroke is located at the edge of the segments, at location of the wavefront discontinuities. There, the DM surface eventually becomes too large and the quasi-linear wavefront control algorithm diverges. However this occurs higher contrasts than in the absence of ACAD.

We then proceeded to simulate the same configuration in the presence of two DMs whose surface at rest was calculated using ACAD. Since there does not exist a model yet to propagate arbitrary wavefronts through ACAD (the models in [Krist et~al. (2011)] only operate under the assumption of an azimuthally symmetric remapping) we can only use the second DM for wavefront control. We work under the assumption that the incident wavefront does not perturb the nominal ACAD remapping (which is true in the case of the surface

map we chose for our example) and that the arguments in [Krist et~al. (2010)] hold so that phase to amplitude conversion in ACAD can be compensated by actuating DM1. Frequency folding will then be the phenomenon responsible for the true contrast limit. In this section we are interested in exploring how this impacts the controllability of wavefront discontinuities using continuous phase-sheet DMs. We used a azimuthally symmetric coronagraph and superposed our wavefront control solution to DM2. We sought to create a Dark Hole between 5 and 23 λ_0/D under a 20% bandwidth with λ_0=700 nm. FIG. **22** shows the results of such a simulation. When the incident wavefront is small enough it is indeed possible to superpose a "classical linear wavefront control" solution to the non-linear ACAD DM shapes in order to carve PSF dark holes. The wavefront control algorithm now yields a DM surface that does not feature prominent deformations at the location of the spiders. Most of the DM stroke is located at the edge of the segments, at location of the wavefront discontinuities and seek to correct the frequency folding terms associated with such discontinuities. At these locations the DM surface eventually becomes too large and the linear wavefront control algorithm diverges. However this divergence occurs at contrast levels much higher than when the ACAD solution is not applied to the DMs. These simulations show that indeed discontinuous phases can be corrected using the second DM of a ACAD whose surfaces have preliminary been set to mitigate the effects of spiders and segment gaps.

7.3 Ultimate Contrast Limits

Assuming that edge ringing has been properly mitigated so that the ray optics approximation underlying the calculation of the DMs shapes is valid, one can wonder about the ultimate contrast limitations of the results presented in this manuscript. Increasing the number of actuators would have dramatic effects on contrast if the actuator count would be such that N>D/d where d is the scale of the aperture discontinuities. Unfortunately current DM technologies are currently far from such a requirement and the solutions presented here are in the regime where N<<D/d. In this regime N only has a marginal influence on contrast when compared to the impact of the cutoff frequency of the tapering kernel. In the regime described here varying the actuator count only changes the size of the corrected region.

The residual PSF artifacts in FIGS. **11** to **20** follow the direction of the initial diffraction pattern associated with secondary support structures and segments. When addressing the problem of aperture discontinuities by solving the Monge-Ampere Equation, ACAD calculates the DM shapes based on a pupil plane metric and thus mostly focuses on attenuating these structures with little regard to the final contrast. It is actually quite remarkable that such a pupil-only approach yields levels of starlight extinction of two to three orders of magnitude. A more appropriate metric would be the final intensity distribution in the post-coronagraphic image plane. However, as discussed in §. 3 classical wavefront control algorithms based on a linearization of the DMs deformations around local equilibrium shapes (such as the ones presented in [Bora & Traub (2006), Give'on et~al. (2007)] in the one DM case or [Pueyo et~al. (2009)] for one or two DMs) cannot be used to compensate the full aperture discontinuities. This is illustrated in FIG. **22** where the DM surface in the vicinity of spiders becomes too large after a certain number of iterations, which leads the iterative algorithm to diverge. When attempting to circumvent this problem by recomputing the linearization at each iteration, we managed to somewhat stabilize the problem for a few iterations and reached marginal contrast improvements, but the overall algorithm remained unstable unless a prohibitively small step size was used. This

is the problem which motivated our effort to calculate the DM shapes as the full non-linear solution of the Monge-Ampere Equation. While doing so yields significant contrast improvements in both the case of JWST like geometries, TMT and on axis-monolithic apertures similar, this approach does not give a proper weight to the spatial frequencies of interest for high contrast imaging. We mitigated this effect by giving a strong weight to the spatial frequencies of interest (in the Dark Hole) when solving the Monge-Ampere Equation.

The next natural step is thus to use non-linear solutions presented herein to correct for the bulk of the aperture discontinuities and to serve as a starting point for classical linearized waveform control algorithms, as illustrated on FIG. 24. FIG. 25 indeed illustrates that when superposing an image plane based wavefront controller to the Monge-Ampere ACAD solution, the contrast can be improved beyond the floor shown on FIG. 12. However, one DM solutions are of limited interest as they only operate efficiently over a finite bandwidth and over half of the image plane. ACAD yields a true broadband solution, and consequently it would be preferable to use the two DMs in the quasi-linear regime to quantify the true contrast limits of ACAD. In such a scheme the DM surfaces are first evaluated as the solution of the Monge-Ampere Equation and then adjusted using the image plane based wavefront control algorithm presented in [Pueyo et~al. (2009)]. However such an exercise requires efficient and robust numerical algorithms to evaluate Eq. 23. Such tool only exist so far in the case of azimuthally symmetric remapping units [Krist et~al. (2010)]. Developing such numerical tools is thus of primary interest to both quantifying the chromaticity and the true contrast limits achievable with on-axis and/or segmented telescopes.

8 Conclusion

We have introduced a technique that takes advantage of the presence of Deformable Mirrors in modern high-contrast coronagraph to compensate for amplitude discontinuities in on-axis and/or segmented telescopes. Our calculations predict that this high throughput class of solutions operates under broadband illumination even in the presence of reasonably small wavefront errors and discontinuities. Our approach relies on controlling two sequential Deformable Mirrors in a non-linear regime yet unexplored in the field of high-contrast imaging. Indeed the mirrors' shapes are calculated as the solution of the two-dimensional pupil remapping problem, which can be expressed as a non-linear partial differential equation called Monge-Ampere Equation. We called this technique Active Compensation of Aperture Discontinuities. While we illustrated the efficiency of ACAD using Apodized Pupil Lyot and Phase Induced Amplitude Coronagraph, it is applicable to all types of coronagraphs and thus enables one to translate the past decade of investigation in coronagraphy with unobscured monolithic apertures to a much wider class of telescope architectures. Because ACAD consists of a simple remapping of the telescope pupil, it is a true broadband solution. Provided that the coronagraph chosen operates under a broadband illumination, ACAD allows high contrast observations over a large spectral bandwidth as pupil remapping is an achromatic phenomenon. We showed that wavelength edge diffraction artifacts, which are the source of spectral bandwidth limits in PIAA coronagraphs (also based on pupil remapping), are no larger than classical Fresnel ringing. We thus argued that they will only marginally impact the spectral bandwidth of a coronagraph whose input beam has been corrected with ACAD. The mirror deformations we find can be achieved, both in curvature and in stroke, with technologies currently used in Ex-AO ground based instruments and in various testbeds aimed at demonstrating high-contrast

for space based applications. Implementing ACAD on a given on-axis and/or segmented thus does not require substantial technology development of critical components.

For geometries analogous to JWST we have demonstrated that ACAD can achieve at least contrast $\sim 10^{-7}$, provided that dynamic high precision segment phasing can be achieved. For TMT and ELT, ACAD can achieve at least contrasts $\sim 10^{-8}$. For on-axis monolithic observatories the design contrast of the coronagraph can be reached with ACAD when the secondary support structures are 5 times thinner than on HST. When they are just as thick as HST contrasts as high as 10^8 can be reached. These numbers are, however, conservative: an optimal solution can be obtained by fine tuning the control term in the Monge-Ampere Equation to the characteristic scale of each discontinuity. As our goal was to introduce this technique to the astronomical community and emphasize its broad appeal to a wide class of architectures (JWST,AT-LAST,HST,TMT,E-ELT) we left this observatory specific exercise for future applications.

The true contrast limitation of ACAD resides in the fact that the Deformable Mirrors are controlled using a pre-coronagraph pupil based metric. However, as illustrated in FIG. 16, the solution provided by ACAD can be used as the starting point for classical linearized waveform control algorithms based in image plane diagnostics. In such a control strategy, the surfaces are first evaluated as the solution of the Monge-Ampere Equation and then adjusted using the quasi-linear method presented in [Pueyo et~al. (2009)]. This control strategy requires efficient and robust numerical algorithms to evaluate the full diffractive propagation in the remapped Fresnel regime. All the contrasts reported here are achieved without aberrations, and we showed that in practice, quasi-linear DM controls based on images at the science camera will have to be superposed to the ACAD solutions. Finally, as ACAD is broadly applicable to all types of coronagraphs, the remapped pupil can be used as the entry point to relax the design of coronagraphs that do operate on segmented apertures such as discussed in [Carlotti et~al. (2011), Guyon et~al. (2010)], also illustrated in FIG. 16. ACAD is thus a promising tool for future high contrast imaging instruments on a wide range of observatories as it will allow astronomers to devise high throughput broadband solutions for a variety of coronagraphs. It only relies on hardware (Deformable Mirrors) that have been extensively tested over the past ten years. Finally since ACAD can operate with all type of coronagraphs and it renders the last decade of research on high-contrast imaging technologies with off-axis unobscured apertures applicable to much broader range of telescope architectures.

Acknowledgment of Support and Disclaimer

REFERENCES

Barman, T. S., Macintosh, B., Konopacky, Q. M., & Marois, C. 2011a, ApJ, 733, 65-. 2011b, ApJ, 735, L39

Belikov, R., Pluzhnik, E., Witteborn, F. C., Greene, T. P., Lynch, D. H., Zell, P. T., & Guyon, O. 2011, in Society of Photo-Optical Instrumentation Engineers (SPIE) Conference Series, Vol. 8151, Society of Photo-Optical Instrumentation Engineers (SPIE) Conference Series

Benamou, J., Froese, B., & Oberman, A. 2010, ESAIM: Mathematical Modelling and Numerical Analysis, 44, 737

Bord'e, P. J. & Traub, W. A. 2006, ApJ, 638, 488

Brown, R. A. & Burrows, C. J. 1990, Icarus, 87, 484 Carlotti, A., Vanderbei, R., & Kasdin, N. J. 2011, Optics Express, 19, 26796

Dacorogna, B. & Moser, J. 1990, Ann. Inst Henri Poincare, 7 Dodson-Robinson, S. E., Veras, D., Ford, E. B., & Beichman,. A. 2009, ApJ, 707, 79

Dohlen, K., Beuzit, J.-L., Feldt, M., Mouillet, D., Puget, P., Antichi, J., Baruffolo, A., Baudoz, P., Berton, A., Boccaletti, A., Carbillet, M., Charton, J., Claudi, R., Downing, M., Fabron, C., Feautrier, P., Fedrigo, E., Fusco, T., Gach, J.-L., Gratton, R., Hubin, N., Kasper, M., Langlois, M., Longmore, A., Moutou, C., Petit, C., Pragt, J., Rabou, P., Rousset, G., Saisse, M., Schmid, H.-M., Stadler, E., Stamm, D., Turatto, M., Waters, R., & Wildi, F. 2006, in Presented at the Society of Photo-Optical Instrumentation Engineers (SPIE) Conference, Vol. 6269, Ground-based and Airborne Instrumentation for Astronomy. Edited by McLean, Ian S.; Iye, Masanori. Proceedings of the SPIE, Volume 6269, pp. 62690Q (2006).

Fortney, J. J., Marley, M. S., Saumon, D., & Lodders, K. 2008, ApJ, 683, 1104

Froese, B. & Oberman, A. 2012, Arxiv preprint arXiv: 1204.5798 Give'on, A., Belikov, R., Shaklan, S., & Kasdin, J. 2007, Opt. Express, 15, 12338

Amir Give'on, N. Jeremy Kasdin, Robert J. Vanderbei and Yoav Avitzour, 2006, J. Opt. Soc. Am. A, 5, pp 1063-1073

Glimm, T. & Oliker, V. 2002, J. Math. Sci., 117

Graham, J. R., Macintosh, B., Doyon, R., Gavel, D., Larkin, J., Levine, M., Oppenheimer, B., Palmer, D., Saddlemyer, L., Sivaramakrishnan, A., Veran, J.-P., & Wallace, K. 2007, ArXiv e-prints, 704

Groff, T. D., Carlotti, A., & Kasdin, N. J. 2011, in Society of Photo-Optical Instrumentation Engineers (SPIE) Conference Series, Vol. 8151, Society of Photo-Optical Instrumentation Engineers (SPIE) Conference Series

Guyon, O. 2003, A&A, 404, 379-. 2005, ApJ, 629, 592

Guyon, O., Angel, J. R. P., Backman, D., Belikov, R., Gavel, D., Giveon, A., Greene, T., Kasdin, J., Kasting, J., Levine, M., Marley, M., Meyer, M., Schneider, G., Serabyn, G., Shaklan, S., Shao, M., Tamura, M., Tenerelli, D., Traub, W., Trauger, J., Vanderbei, R., Woodruff, R. A., Woolf, N. J., & Wynn, J. 2008, in Society of Photo-Optical Instrumentation Engineers (SPIE) Conference Series, Vol. 7010, Society of Photo-Optical Instrumentation Engineers (SPIE) Conference Series

Guyon, O., Martinache, F., Belikov, R., & Soummer, R. 2010a, ApJS, 190, 220

Guyon, O., Pluzhnik, E., Martinache, F., Totems, J., Tanaka, S., Matsuo, T., Blain, C., & Belikov, R. 2010b, PASP, 122, 71

Guyon, O., Pluzhnik, E. A., Galicher, R., Martinache, F., Ridgway, S. T., & Woodruff, R. A. 2005, ApJ, 622, 744

Guyon, O., Matsuo, T. and Angel, R., 2009, ApJ, 693, 75-84 Hinkley, S., Oppenheimer, B. R., Zimmerman, N., Brenner, D., Parry, I. R., Crepp, J. R., Vasisht, G., Ligon, E., King, D., Soummer, R., Sivaramakrishnan, A., Beichman, C., Shao, M., Roberts, L. C., Bouchez, A., Dekany, R., Pueyo, L., Roberts, J. E., Lockhart, T., Zhai, C., Shelton, C., & Burruss, R. 2011, PASP, 123, 74

Johnson, J. A., Aller, K. M., Howard, A. W., & Crepp, J. R. 2010, PASP, 122, 905

Kalas, P., Graham, J. R., Chiang, E., Fitzgerald, M. P., Clampin, M., Kite, E. S., Stapelfeldt, K., Marois, C., & Krist, J. 2008, Science, 322, 1345

Kasdin, N. J., Vanderbei, R. J., Littman, M. G., & Spergel, D. N. 2005, Appl. Opt., 44, 1117

Kratter, K. M., Murray-Clay, R. A., & Youdin, A. N. 2010, ApJ, 710, 1375

Krist, J. E., Belikov, R., Pueyo, L., Mawet, D. P., Moody, D., Trauger, J. T., & Shaklan, S. B. 2011, in Society of Photo-Optical Instrumentation Engineers (SPIE) Conference Series, Vol. 8151, Society of Photo-Optical Instrumentation Engineers (SPIE) Conference Series

Krist, J. E., Pueyo, L., & Shaklan, S. B. 2010 in (SPIE), 77314N Kuchner, M. J. & Traub, W. A. 2002, ApJ, 570, 900

Lagrange, A.-M., Bonnefoy, M., Chauvin, G., Apai, D., Ehrenreich, D., Boccaletti, A., Gratadour, D., Rouan, D., Mouillet, D., Lacour, S., & Kasper, M. 2010, Science, 329, 57

Loeper, G. & Rapetti, F. 2005, Comptes Rendus Mathematique, 340, 319

Lozi, J., Martinache, F., & Guyon, O. 2009, PASP, 121, 1232 Macintosh, B., Troy, M., Doyon, R., Graham, J., Baker, K., Bauman, B., Marois, C., Palmer, D., Phillion, D., Poyneer, L., Crossfield, I., Dumont, P., Levine, B. M., Shao, M., Serabyn, G., Shelton, C., Vasisht, G., Wallace, J. K., Lavigne, J.-F., Valee, P., Rowlands, N., Tam, K., & Hackett, D. 2006, in Society of Photo-Optical Instrumentation Engineers (SPIE) Conference Series, Vol. 6272, Society of Photo-Optical Instrumentation Engineers (SPIE) Conference Series

Madhusudhan, N., Burrows, A., & Currie, T. 2011, ApJ, 737, 34 Marley, M. S., Saumon, D., & Goldblatt, C. 2010, ApJ, 723, L117 Marois, C., Macintosh, B., Barman, T., Zuckerman, B., Song, I., Patience, J., Lafreni'ere, D., & Doyon, R. 2008, Science, 322, 1348

Martinache, F., Guyon, O., Pluzhnik, E. A., Galicher, R., & Ridgway, S. T. 2006, ApJ, 639, 1129

Martinez, P., Boccaletti, A., Kasper, M., Cavarroc, C., Yaitskova, N., Fusco, T., & V'erinaud, C. 2008, A&A, 492, 289

Martinez, P., Dorrer, C., Kasper, M., Boccaletti, A., & Dohlen, K. 2010, A&A, 520, A110

Mawet, D., Pueyo, L., Moody, D., Krist, J., & Serabyn, E. 2010 in (SPIE), 773914

Mawet, D., Serabyn, E., Wallace, J. K., & Pueyo, L. 2011, Optics Letters, 36, 1506

Monge, G. 1781, Histoire de l'Acad'emie Royale des Sciences de Paris, 666

Pluzhnik, E. A., Guyon, O., Ridgway, S. T., Martinache, F., Woodruff, R. A., Blain, C., & Galicher, R. 2005, ArXiv Astrophysics e-prints

Postman, M., Traub, W. A., Krist, J., Stapelfeldt, K., Brown, R., Oegerle, W., Lo, A., Clampin, M., Soummer, R., Wiseman, J., & Mountain, M. 2010, in Astronomical Society of the Pacific Conference Series, Vol. 430, Pathways Towards Habitable Planets, ed. V. Coud'e Du Foresto, D. M. Gelino, & I. Ribas, 361

Poyneer, L. A. & V'eran, J.-P. 2005, Journal of the Optical Society of America A, 22, 1515

Pueyo, L. 2008, PhD thesis, Princeton University Pueyo, L. & Kasdin, N. J. 2007, ApJ, 666, 609

Pueyo, L., Kasdin, N. J., Carlotti, A., & Vanderbei, R. 2011, ApJS, 195, 25

Pueyo, L., Kasdin, N. J., & Shaklan, S. 2011, J. Opt. Soc. Am. A, 28, 189

Pueyo, L., Kay, J., Kasdin, N. J., Groff, T., McElwain, M., Give'on, A., & Belikov, R. 2009, Appl. Opt., 48, 6296

Pueyo, L., Wallace, K., Troy, M., Burruss, R., Macintosh, B., & Soummer, R. 2010 in (SPIE), 77362A

Rafikov, R. R. 2005, ApJ, 621, L69

Rouan, D., Riaud, P., Boccaletti, A., Cl'enet, Y., & Labeyrie, A. 2000, PASP, 112, 1479

Sauvage, J.-F., Fusco, T., Rousset, G., & Petit, C. 2007, Journal of the Optical Society of America A, 24, 2334

Shaklan, S. B. & Green, J. J. 2006, Appl, Opt., 45, 5143

Shaklan, S. B., Green, J. J., & Palacios, D. M. 2006, in Presented at the Society of Photo-Optical Instrumentation Engineers (SPIE) Conference, Vol. 6265, Space Telescopes and Instrumentation I: Optical, Infrared, and Millimeter. Edited by Mather, John C.; MacEwen, Howard A.; de Graauw, Mattheus W. M. Proceedings of the SPIE, Volume 6265, pp. 626511 (2006).

Soummer, R., Aime, C., & Falloon, P. E. 2003, A&A, 397, 1161 Soummer, R., Pueyo, L., Ferrari, A., Aime, C., Sivaramakrishnan, A., & Yaitskova, N. 2009, ApJ, 695, 695

Soummer, R., Sivaramakrishnan, A., Pueyo, L., Macintosh, B., & Oppenheimer, B. R. 2011, ApJ, 729, 144

Spiegel, D. S. & Burrows, A. 2012, ApJ, 745, 174

Thomas, S. J., Soummer, R., Dillon, D., Macintosh, B., Gavel, D., & Sivaramakrishnan, A. 2011, AJ, 142, 119

Traub, W. A. & Vanderbei, R. J. 2003, ApJ, 599, 695 Trauger, J., Stapelfeldt, K., Traub, W., Krist, J., Moody, D., Mawet, D., Serabyn, E., Henry, C., Brugarolas, P., Alexander, J., Gappinger, R., Dawson, O., Mireles, V., Park, P., Pueyo, L., Shaklan, S., Guyon, O., Kasdin, J., Vanderbei, R., Spergel, D., Belikov, R., Marcy, G., Brown, R. A., Schneider, J., Woodgate, B., Egerman, R., Matthews, G., Elias, J., Conturie, Y., Vallone, P., Voyer, P., Polidan, R., Lillie, C., Spittler, C., Lee, D., Hejal, R., Bronowicki, A., Saldivar, N., Ealey, M., & Price, T. 2010, in Society of Photo-Optical Instrumentation Engineers (SPIE) Conference Series, Vol. 7731, Society of Photo-Optical Instrumentation Engineers (SPIE) Conference Series

Trauger, J. T. & Traub, W. A. 2007, Nature, 446, 771 Vanderbei, R. J., Cady, E., & Kasdin, N. J. 2007, ApJ, 665, 794 Vanderbei, R. J., Spergel, D. N., & Kasdin, N. J. 2003a, ApJ, 599, 686-, 2003b, ApJ, 590, 593

Vanderbei, R. J. & Traub, W. A. 2005, ApJ, 626, 1079 V'erinaud, C., Kasper, M., Beuzit, J., Gratton, R. G., Mesa, D., Aller-Carpentier, E., Fedrigo, E., Abe, L., Baudoz, P., Boccaletti, A., Bonavita, M., Dohlen, K., Hubin, N., Kerber, F., Korkiakoski, V., Antichi, J., Martinez, P., Rabou, P., Roelfsema, R., Schmid, H. M., Thatte, N., Salter, G., Tecza, M., Venema, L., Hanenburg, H., Jager, R., Yaitskova, N., Preis, O., Orecchia, M., & Stadler, E. 2010, in Society of Photo-Optical Instrumentation Engineers (SPIE) Conference Series, Vol. 7736, Society of Photo-Optical Instrumentation Engineers (SPIE) Conference Series

Wallace, J. K., Burruss, R., Pueyo, L., Soummer, R., Shelton, C., Bartos, R., Fregoso, F., Nemati, B., Best, P., & Angione, J. 2009, in Proceedings of the SPIE conference 7440, ed. S. B. Shaklan, Vol. 7440 (SPIE)

Wallace, J. K., Rao, S., Jensen-Clem, R. M. and Serabyn, G., 2011, Proc SPIE 8126

Watanabe, M., Oya, S., Hayano, Y., Takami, H., Hattori, M., Minowa, Y., Saito, Y., Ito, M., Murakami, N., Iye, M., Guyon, O., Colley, S., Eldred, M., Golota, T., & Dinkins, M. 2008, in Society of Photo-Optical Instrumentation Engineers (SPIE) Conference Series, Vol. 7015, Society of Photo-Optical Instrumentation Engineers (SPIE) Conference Series

Zheligovsky, V., Podvigina, O., & Frisch, U. 2010, Journal of Computational Physics, 229, 5043

The embodiments illustrated and discussed in this specification are intended only to teach those skilled in the art how to make and use the invention. In describing embodiments of

the invention, specific terminology is employed for the sake of clarity. However, the invention is not intended to be limited to the specific terminology so selected. The above-described embodiments of the invention may be modified or varied, without departing from the invention, as appreciated by those skilled in the art in light of the above teachings. It is therefore to be understood that, within the scope of the claims and their equivalents, the invention may be practiced otherwise than as specifically described.

We claim:

1. An active optical beam shaping system, comprising:

a first deformable mirror arranged to at least partially intercept an entrance beam of light and to provide a first reflected beam of light;

a second deformable mirror arranged to at least partially intercept said first reflected beam of light from said first deformable mirror and to provide a second reflected beam of light; and

a signal processing and control system configured to communicate with said first and second deformable mirrors,

wherein said signal processing and control system is configured to provide control signals to said first deformable mirror so as to configure a reflecting surface of said first deformable mirror to substantially conform to a calculated surface shape,

wherein said signal processing and control system is further configured to provide control signals to said second deformable mirror to configure a reflecting surface of said second deformable mirror to substantially conform to a calculated surface shape,

wherein said first deformable mirror, said second deformable mirror and said signal processing and control system together provide a large amplitude light modulation range to provide an actively shaped optical beam,

wherein said large amplitude modulation range is characterized by

$$\left| \frac{\partial h}{\partial \vec{r}} \right| \geq O(\theta_s)$$

wherein

$$\left| \frac{\partial h}{\partial \vec{r}} \right|$$

is a focal gradient of at least one of said first deformable mirror and said second deformable mirror at a point of a respective reflecting surface thereof,

wherein h is a surface deflection of a corresponding one of said first deformable mirror and said second deformable mirror at said point, and

wherein θ_s is a solid angle subtended by a disk of radius δ and the distance z between said first deformable mirror and said second deformable mirror.

2. An active optical beam shaping system according to claim 1, wherein said large amplitude modulation range is greater than 1.2% of a fully illuminated portion of said entrance beam of light.

3. An active optical beam shaping system according to claim 2, wherein said large amplitude modulation range is substantially an entire range to permit selectable amplitude modulation of portions of said entrance beam of light any-

where from substantially fully attenuated to substantially fully illuminated relative to fully illuminated portions of said entrance beam of light.

4. An active optical beam shaping system according to claim **1**, further comprising a beam analyzer arranged to receive at least a portion of said exit beam of light reflected from said second deformable mirror,

    wherein said beam analyzer is configured to communicate with said signal processing and control system to provide feedback control of at least one of said first and second deformable mirrors.

5. An active optical beam shaping system according to claim **1**, wherein said signal processing and control system is further configured to calculate said surface shape of at least one of said first and second deformable mirrors based on reverse ray tracing calculations.

6. An active optical beam shaping system according to claim **1**, wherein said signal processing and control system is further configured to calculate said surface shape of at least one of said first and second deformable mirrors based on a solution to Monge-Ampere equations corresponding to said active optical beam shaping system.

7. An optical transmitter, comprising:

an optical source; and

an optical modulator arranged in an optical path of said optical source,

wherein said optical modulator comprises:

    a first deformable mirror arranged to at least partially intercept an entrance beam of light from said optical source and to provide a first reflected beam of light;

    a second deformable mirror arranged to at least partially intercept said first reflected beam of light from said first deformable mirror and to provide a second reflected beam of light; and

    a signal processing and control system configured to communicate with said first and second deformable mirrors,

wherein said signal processing and control system is configured to provide control signals to said first deformable mirror and said second deformable mirror to provide at least a portion of said second reflected beam of light as an output beam having at least one of a selectable amplitude profile or selectable phase profile,

wherein said first deformable mirror, said second deformable mirror and said signal processing and control system together provide a large amplitude light modulation range to provide an actively shaped optical beam,

wherein said large amplitude modulation range is characterized by

$$\left| \frac{\partial h}{\partial \vec{r}} \right| \geq O(\theta_s)$$

wherein

$$\left| \frac{\partial h}{\partial \vec{r}} \right|$$

is a focal gradient of at least one of said first deformable mirror and said second deformable mirror at a point of a respective reflecting surface thereof,

    wherein h is a surface deflection of a corresponding one of said first deformable mirror and said second deformable mirror at said point, and

    wherein θ_s is a solid angle subtended by a disk of radius δ and the distance z between said first deformable mirror and said second deformable mirror.

8. An optical transmitter according to claim **7**, wherein said signal processing and control system is configured to provide control signals to said first deformable mirror and said second deformable mirror such that said output beam has both a selectable amplitude profile and selectable phase profile.

9. An optical transmitter according to claim **8**, wherein said signal processing and control system is configured to provide control signals to said first deformable mirror and said second deformable mirror such that said output beam of light comprises soliton pulses.

10. An optical receiver, comprising:

an optical detector; and

an optical filter arranged in an optical path of said optical detector,

wherein said optical filter comprises:

a first deformable mirror arranged to at least partially intercept an entrance beam of light being detected to provide a first reflected beam of light;

a second deformable mirror arranged to at least partially intercept said first reflected beam of light from said first deformable mirror and to provide a second reflected beam of light; and

a signal processing and control system configured to communicate with said first and second deformable mirrors,

wherein said signal processing and control system is configured to provide control signals to said first deformable mirror and said second deformable mirror to provide at least a portion of said second reflected beam of light as an output beam directed to said optical detector having at least one of a selectable amplitude profile or selectable phase profile,

wherein said first deformable mirror, said second deformable mirror and said signal processing and control system together provide a large amplitude light modulation range to provide an actively shaped optical beam,

wherein said large amplitude modulation range is characterized by

$$\left| \frac{\partial h}{\partial \vec{r}} \right| \geq O(\theta_s)$$

wherein

$$\left| \frac{\partial h}{\partial \vec{r}} \right|$$

is a focal gradient of at least one of said first deformable mirror and said second deformable mirror at a point of a respective reflecting surface thereof,

    wherein h is a surface deflection of a corresponding one of said first deformable mirror and said second deformable mirror at said point, and

    wherein θ_s is a solid angle subtended by a disk of radius δ and the distance z between said first deformable mirror and said second deformable mirror.

11. An optical communication system, comprising:

an optical transmitter;

an optical transmission path optically coupled to said optical transmitter; and

an optical receiver optically coupled to said optical transmission path,

53

wherein at least one of said optical transmitter, said optical transmission path, or said optical receiver comprises an active optical beam shaper, and

wherein said active optical beam shaper comprises:

a first deformable mirror arranged to at least partially intercept an entrance beam of light to provide a first reflected beam of light;

a second deformable mirror arranged to at least partially intercept said first reflected beam of light from said first deformable mirror and to provide a second reflected beam of light; and

a signal processing and control system configured to communicate with said first and second deformable mirrors,

wherein said signal processing and control system is configured to provide control signals to said first deformable mirror and said second deformable mirror to provide at least a portion of said second reflected beam of light as an output beam having at least one of a selectable amplitude profile or selectable phase profile,

wherein said first deformable mirror, said second deformable mirror and said signal processing and control system together provide a large amplitude light modulation range to provide an actively shaped optical beam,

wherein said large amplitude modulation range is characterized by

$$\left|\frac{\partial h}{\partial \vec{r}}\right| \geq O(\theta_s)$$

wherein

$$\left|\frac{\partial h}{\partial \vec{r}}\right|$$

is a focal gradient of at least one of said first deformable mirror and said second deformable mirror at a point of a respective reflecting surface thereof,

wherein h is a surface deflection of a corresponding one of said first deformable mirror and said second deformable mirror at said point, and

wherein θ_s is a solid angle subtended by a disk of radius δ and the distance z between said first deformable mirror and said second deformable mirror.

12. An optical communication system according to claim 11, wherein said optical transmission path is at least one of an atmospheric or substantially a vacuum transmission path to provide a free-space optical transmission path,

wherein said an optical transmitter is arranged to transmit a free-space optical signal, and

wherein said optical receiver is arranged to receive a free-space optical signal such that said optical communication system is a free-space optical communication system.

13. An optical communication system according to claim 11, wherein said optical transmission path comprises an optical waveguide arranged to receive optical signals from said optical receiver and transmit said optical signals to said optical receiver.

14. An optical communication system according to claim 13, wherein said optical waveguide is an optical fiber such that said optical communication system is a fiber-optic communication system.

54

15. An optical telescope, comprising:

a light collection and magnification system;

an active optical beam shaper arranged in an optical path of light collected and magnified by said light collection and magnification system; and

an optical detection system arranged to receive a beam of light from said active optical beam shaper,

wherein said active optical beam shaper comprises:

a first deformable mirror arranged to at least partially intercept an entrance beam of light to provide a first reflected beam of light;

a second deformable mirror arranged to at least partially intercept said first reflected beam of light from said first deformable mirror and to provide a second reflected beam of light; and

a signal processing and control system configured to communicate with said first and second deformable mirrors,

wherein said signal processing and control system is configured to provide control signals to said first deformable mirror and said second deformable mirror to provide at least a portion of said second reflected beam of light as an output beam having at least one of a selectable amplitude profile or selectable phase profile,

wherein said first deformable mirror, said second deformable mirror and said signal processing and control system together provide a large amplitude light modulation range to provide an actively shaped optical beam,

wherein said large amplitude modulation range is characterized by

$$\left|\frac{\partial h}{\partial \vec{r}}\right| \geq O(\theta_s)$$

wherein

$$\left|\frac{\partial h}{\partial \vec{r}}\right|$$

is a focal gradient of at least one of said first deformable mirror and said second deformable mirror at a point of a respective reflecting surface thereof,

wherein h is a surface deflection of a corresponding one of said first deformable mirror and said second deformable mirror at said point, and

wherein θ_s is a solid angle subtended by a disk of radius δ and the distance z between said first deformable mirror and said second deformable mirror.

16. A solar furnace, comprising:

a light collection system;

an active optical beam shaper arranged in an optical path of light collected by said light collection system; and

an optical focusing system arranged to receive a beam of light from said active optical beam shaper to be focused on an object to be heated,

wherein said active optical beam shaper comprises:

a first deformable mirror arranged to at least partially intercept an entrance beam of light to provide a first reflected beam of light;

a second deformable mirror arranged to at least partially intercept said first reflected beam of light from said first deformable mirror and to provide a second reflected beam of light; and

a signal processing and control system configured to communicate with said first and second deformable mirrors,

wherein said signal processing and control system is configured to provide control signals to said first deformable mirror and said second deformable mirror to provide at least a portion of said second reflected beam of light as an output beam having at least one of a selectable amplitude profile or selectable phase profile,

wherein said first deformable mirror, said second deformable mirror and said signal processing and control system together provide a large amplitude light modulation range to provide an actively shaped optical beam,

wherein said large amplitude modulation range is characterized by

$$\left|\frac{\partial h}{\partial \vec{r}}\right| \geq O(\theta_s)$$

wherein

$$\left|\frac{\partial h}{\partial \vec{r}}\right|$$

is a focal gradient of at least one of said first deformable mirror and said second deformable mirror at a point of a respective reflecting surface thereof,

wherein h is a surface deflection of a corresponding one of said first deformable mirror and said second deformable mirror at said point, and

wherein θ_s is a solid angle subtended by a disk of radius δ and the distance z between said first deformable mirror and said second deformable mirror.

17. An optical pulse-shaping system, comprising:

an optical pulse source;

a first diffraction grating disposed in an optical path of said optical pulse source;

an active optical beam shaper disposed in an optical path of light diffracted from said first diffraction grating; and

a second diffraction grating disposed in an optical path of light output from said active optical beam shaper,

wherein said active optical beam shaper comprises:

a first deformable mirror arranged to at least partially intercept an entrance beam of light to provide a first reflected beam of light;

a second deformable mirror arranged to at least partially intercept said first reflected beam of light from said first deformable mirror and to provide a second reflected beam of light; and

a signal processing and control system configured to communicate with said first and second deformable mirrors,

wherein said signal processing and control system is configured to provide control signals to said first deformable mirror and said second deformable mirror to provide at least a portion of said second reflected beam of light as an output beam having at least one of a selectable amplitude profile or selectable phase profile.

* * * * *